UNIVERSITY OF CALIFORNIA
RIVERSIDE

High Performance Abrasion-Resistant Materials: Lessons from Nature

A Dissertation submitted in partial satisfaction
of the requirements for the degree of

Doctor of Philosophy

in

Chemical and Environmental Engineering

by

Qianqian Wang

September 2012

Dissertation Committee:
Dr. David Kisailus, Chairperson
Dr. Guanshui Xu
Dr. Pablo D. Zavattieri

The Dissertation of Qianqian Wang is approved:

_____

_____

_____

Committee Chairperson

University of California, Riverside

Acknowledgements

I want to thank my advisor, Dr. David Kisailus, for his incredible support and help on this project during the past four years. Passionate, knowledgeable and insightful in materials science, he gave me guidance and inspiration for this project. Kind, nice and patient, Dr. Kisailus made my research life as a Ph. D. student easier. He helped me a lot in conducting experiments, analyzing data and writing paper. Dr. Kisailus also helped me a lot in the skills of presentation and academic communications. With his support, I got the chance to present my work at several world class conferences. I am also grateful for his help in the guidance for my career development. It will never be overestimated about how much Dr. Kisailus helped me during the past four years for Ph.D. study.

I want to thank Dr. James Weaver, who was a post-doctoral researcher in our lab and worked on this project before September 2009. The initial study of this project was done by him. He made incredible contributions to the work in chapter 2. I am also grateful for his training on sample preparation and data analysis when I first started this project.

I want to thank Dr. Elaine DiMasi, who is a staff scientist at the National Synchrotron Light Source Department in Brookhaven National Lab. She helped me with synchrotron XRD experiments and data analysis. Elaine is smart, knowledgeable, organized and helpful. The skills I learned from her, including data organizing and analysis and paper writing, helped me not only in the synchrotron XRD section, but also in all other parts of my Ph.D. study. She once included the following sentence in our

email communications: “Nobody knows how hard scientists work to cover everything - except other scientists.” This was very encouraging.

I want to thank Dr. Pablo Zavattieri, who is an assistant professor in the School of Civil Engineering at Purdue University and collaborated with us on this project. I spent two months in his lab during the summer of 2010 and learned FEM from him. He is smart, nice and helpful. He taught me a lot with his expertise in FEM and mechanics. I am also grateful for his time to fly out here for my Ph.D. qualification exam and defense. Our collaboration on this project will continue.

I want to thank Dr. Michiko Nemoto and Dr. Dongsheng Li, who were post-doctoral researchers in our lab and helped me with this project. Both of them are smart, hard working and helpful. I want to thank Brian Weden and Leslie Wood, who were undergraduates and helped me with this project. They not only helped me with experiments, but also brought in ideas for this project. I want to thank Garrett Milliron and Christopher Salinas, who are graduate students in our lab and helped me on data analysis with their expertise in coding and programming. I also want to thank all the other graduate students in our group: Wenting Hou, Jianxin Zhu, Nichola Kinsinger and John Johnson. All of my group members are fun and helpful. They made my life in the lab happy and memorable. I enjoyed the time we spent together not only in the lab but also in our group trips to the beach and Yosemite National park.

Last, but the most important, I want to thank my father, Zhongfeng Wang, and my mother, Yinli Li. They are the best parents. Neither of them got a college degree, but they

succeeded in supporting a daughter for a Ph.D. degree and a son for a Bachelor degree. With their love and support, I got the confidence and courage to come to USA and go for my dreams. They may not always understand or agree with my choices, but they are always there for support once I make a decision. They are kindhearted, strong, and optimistic. It was those personalities I inherited from them that made this Ph.D. study possible. I am proud of them and appreciate being their daughter.

ABSTRACT OF THE DISSERTATION

High Performance Abrasion-Resistant Materials:
Lessons from Nature

by

Qianqian Wang

Doctor of Philosophy, Graduate Program in Chemical and Environmental Engineering
University of California, Riverside, September 2012
Dr. David Kisailus, Chairperson

Chitons are marine mollusks found worldwide in the intertidal or subtidal zones of cold water as well as in tropical waters. These organisms have evolved an amazing feeding structure called a radula. The radula is a ribbon-like structure that consists of abrasion resistant teeth anchored to a flexible stylus that the organism uses to abrade rocky substrates to reach endolithic and epilithic algae. In this work, we investigated the radula in *Cryptochiton stelleri*, the largest of the chitons. Using various microscopic and spectroscopic techniques, an ultrastructural analysis and investigation of mechanical properties of fully mineralized radular teeth from *C. stelleri*, as well as the mineralization process of these teeth, has been performed to gain insights into structure-function relationships of the abrasion resistant, impact tolerant, and anti-fatigue composites synthesized by nature. Shape, wear patterns, and feeding positions of the teeth have been analyzed to provide teeth working conditions that can be used in finite element analysis modeling of the tooth, which helps to provide a foundation to produce abrasion-resistant, impact-tolerant and anti-fatigue materials.

An overall analysis of mature radular teeth using Scanning Electron Microscopy (SEM), X-ray Diffraction (XRD), Transmission Electron Microscopy (TEM) and Raman Spectroscopy revealed a magnetite containing hard shell with an iron phosphate containing soft core. α-chitin was also identified in mature teeth with powder XRD. Energy-dispersive X-ray spectroscopy (EDS) analysis uncovered the higher carbon concentration at the core region than at the shell. Hardness and modulus gradients from the leading edge to the trailing edge of the teeth, which contributes to a self-sharpening mechanism, were revealed by nanoindentation. The mechanical measurements revealed the teeth had the highest hardness (12.5 GPa) and modulus (125 GPa) of any biomineral reported to date.

Phase transformation and structural development during the biomineralization process of the radular teeth were analyzed with EDS, synchrotron XRD, Micro- X-ray Fluorescence (μXRF), SEM and TEM. The phase transformation from ferrihydrite to magnetite, which occurred at the tip of the leading edge, along with aggregation of mineral particles and shrinkage of organic fibers were discovered.

Regional micro- and nanostructures as well as the mechanical properties of the mature teeth were characterized via SEM analysis of the fracture surfaces, TEM and nanoindentation. Nanorods structures were found at the trailing edges and the surfaces of the leading edges of teeth. The middle of the leading edge of the tooth is made of close-packed particles and exhibited the highest hardness and modulus. The rods at the trailing edge were orientated along the surface curvature of the trailing edge, while the rods at the

surface of the leading edge were rotated 90°. The diameters of the rods at the trailing edge were larger than those at the leading edge. Tooth performance was simulated with FEM analysis on a radular tooth model obtained from confocal microscopy imaging. Tensile stresses were concentrated at the leading edge, while the compressive stresses were concentrated at the trailing edge. Both of the stress directions are guided along the surface curvature, following the major orientation of the rods. The combination of regional ultrastructural features of these teeth, consisting of the highest hardness and modulus mineral known in Nature, enables the radular teeth to be optimized abraders during the feeding process.

Table of Contents

List of Tables

List of Figures

1 Chapter 1. Introduction and Overview

1.1 General overview

With our ever increasing population and dwindling supply of natural resources, there is a growing need for the development of new light-weight structural materials with high strength and durability that are low-cost and recyclable. Current technologies to process hard and abrasion resistant materials are usually energy cost and not environmental friendly, such as high sintering, surface hardening with carburization, casting and etc.

Throughout billions of years of evolution, Nature has evolved efficient strategies, exemplified in the crystallized tissues of numerous species, to synthesize complex composite materials that often exhibit exceptional mechanical properties. These biological systems demonstrate the ability to control nano- and microstructural features that significantly improve the mechanical performance of otherwise brittle materials. For thousands of years, Man has made observations of natural systems to improve on technology. For example, the Chinese invented saw with inspiration from the serrate leaves and teeth of locusts; the Italian Renaissance polymath Leonardo da Vinci got ideas about several designs of flying machines from his studies of the flight of birds. In 1917, D'Arcy W. Thompson made such observations and first published his works on investigations of structures of biological systems [1]. He claimed that, other than the natural selection, the physical laws and mechanics should also be emphasized as the fundamental determinant of the form and structure of living organisms. He pointed out

examples that relate biological systems to mechanical phenomena, such as the internal supporting structures in the hollow bones of birds vs. the truss design in buildings, the compression-tension bearing of bones-ligaments structures in human bodies vs. the thick -thin lines combinations of cantilever bridges.

Over the past 100 years, there has been an explosion of research involving the study of structural biological materials [2]. However, the materials approaches were shunned by biologists because of the different views from engineers and biologists [3]. As a young and vibrant discipline, materials science and engineering utilizes the knowledge gleaned from physics, chemistry and biology to make engineering developments. Although traditional areas of materials science and engineering include metals, polymers, and ceramics, biological materials typically include a combination of these classes of materials and have thus gained the attention of materials scientists' for multiple decades.

These biological structures exhibit unique design features that afford exceptional performance. One such characteristic is the ability to resist abrasion. Abrasion resistance is the ability for a material to withstand mechanical actions, such as rubbing, scraping or erosion that tend to remove the surface or part of that material. Abrasion resistance is important for maintaining both the shape and function of materials. Materials with this property have wide application in multiple areas: wear resistant bearings, steel plates, welding rods, ceramics, rubber, tubing, welding consumables, foundry goods, etc. Some

examples of applications of abrasion resistant materials in daily life and industry are listed in Figure 1.

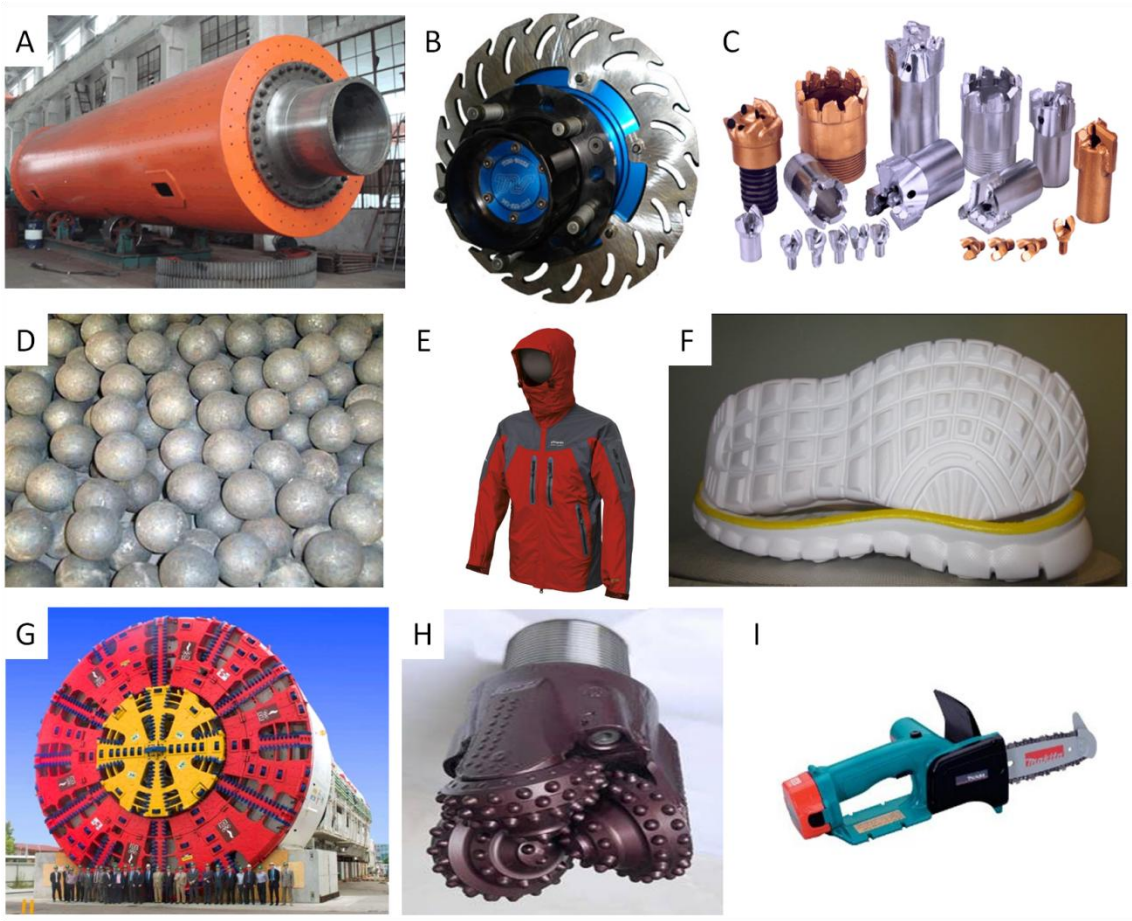

Figure 1.1Examples of applications of abrasion resistant materials. (A) steel roller ball mill cylinder, (B) Blade Brake Rotors, (C) shaping and machining tools, (D) wear resistant bearings, (E) jackets, (F) rubber sole of shoes, (G) tunnel boring, (H) oil drilling and (I) electric saw.

Abrasion wear occurs when a hard and rough surface comes in contact with and slides against a soft surface, removing layers of the softer material. The harder material will maintain shape and function, while the softer one will be depleted. Decreasing abrasion wear is possible by using different approaches including smoothing the contact

surfaces or adding lubricant to decrease friction. If these working conditions cannot be implemented or optimized to avoid abrasion wear, another approach is to utilize materials that are abrasion-resistant and hard.

As mentioned previously, abrasion resistance is found in some biological systems such as skin, nails, and beaks. One outstanding example is found in the heavily crystallized radular teeth of the chitons, a group of elongated mollusks that graze on hard substrates for algae. The radula, a toothed ribbon-like structure, which is used for this feeding are well known for their ability to efficiently erode the rocky surfaces on which they feed [2]. Understanding the ultrastructural features of these teeth that yield remarkable damage tolerance and abrasion resistance, and to design new biomimetic abrasion-resistant materials were the inspiration for this dissertation. The goal of this project was to understand the physical and chemical composition of the radular teeth, uncover the process by which they were formed, interpret the structure-function relationships, and utilize finite element analysis and biomimicry to verify our observations.

1.2 Principles and process of biomineralization

1.2.1 Biominerals

Minerals have been used by organisms for at least 3500 million years [2]. About 540 million years ago, there was a period that some organisms succeeded in constructing their skeletons with minerals [2].Today more than sixty different minerals are widespread in all five kingdoms of organisms [2]. These include both amorphous and inorganic

crystals. The predominant biological minerals are composed of either silica or calcium carbonate, but can also consist of calcium phosphate, iron oxides, etc. Amorphous minerals, like calcium carbonate and phosphate, are usually used as temporary storage depots for ions essential for cellular metabolism [4]. Other uses of amorphous minerals are fulfilling skeleton functions, such as the stylets composed of amorphous calcium phosphate are used as harpoon to capture preys in nemerteans (ribbon worms) [5], or working as a repository for embedding toxic metals, of which the most common host mineral is amorphous calcium pyrophosphate [6]. On the other hand, crystalline minerals are used by organisms in many different areas. One of the common functions is gravity perception for mobile organisms. For example, the movement of minerals depositing around the cell cavities are tracked by the sensory cells [2]. The navigation function of single crystals of iron oxides is also well-known [7].

1.2.2 Principles of biomineralization process

Based on the definition from Lowenstam in 1981, there are two distinguishable types of mineralization processes: “biologically induced” and “matrix mediated”. For biologically induced mineralization, minerals are developed by interactions between biologically produced metabolite end products with cations in the external environment. This process occurs widely among prokaryotes intracellularly and extracellularly. It also occurs in eukaryotes, including some algal representatives of the protoctista, many plant phyla, and some animal phyla. However, the minerals also form intercellularly in algae and intracellularly in plants and animals [2].

"Organic matrix mediated" mineralization is a process that nucleation and subsequent development of minerals takes place in contact with a performed organic matrix. Compared with the "biologically induced" process, it affords greater control in the size, morphology and orientation of the mineral crystals. The mineral products of this process are mostly located at extracellular sites among the eukaryotes. The minerals precipitated from an organic matrix mediated process usually form hard parts for organisms, such as, exo- and endoskeletons, as well as solely isolated grains or skeletal pinpoint mineralization of crystal aggregates.

1.2.3 Iron minerals in biology systems

Iron plays a key role in metabolic processes, including the transport of oxygen in hemoglobin of vertebrate blood to a central role in the cytochrome system [7]. Bacteria has developed elegant mechanisms to incorporate extracellular iron and produce numerous siderophores, which are small iron-specific chelating compounds, that make up the slow transport of dissolved iron in the predominantly oxidizing hydrosphere. On the other hand, iron minerals are widely distributed in biological systems as well, including transport and storage, waste disposal, hardening of teeth, and navigation. Among all the minerals that have been discovered and for which the crystal structures have been identified, there are 10 iron-containing minerals, including oxides, sulfates, sulfides and phosphates (Table 1.1.) Ferrihydrite is considered as the fourth widely used mineral in biological systems since it is a component of the micelle of the well-known iron storage protein, ferritin (found in numerous organisms). Besides ferrihydrite, there is as abundant source of magnetite in biological organisms [7].

Minerals	Occurrence	Mineralization Process (es)	Mineral location (typical examples)	references
Oxides				
magnetite (Fe_3O_4)	Bacteria	Matrix mediated	Intracellular magnetosomes	Blakemore (1975)
	Protozoa (?)	Unknown	Unknown	Lins de Barros *et al.*(1981)
	Molluscs	Matrix mediated	Extracellular in chiton teeth	Lowenstam (1962a)
	Arthropods	Unknown	Honeybee abdomen	Gould *et al.* (1978)
	Chordates	Matrix mediated (?)	Tuna dermethmoid bone, pigeon head	Walker et al. (Chapter 20), Walcott *et al.* (1979)
Ferrihydrite ($5Fe_2O_3 \cdot 9H_2O$)	Bacteria	Matrix mediated	Bacterioferritin micelle	Stiefel and Watt (1979), Yariv *et al.* (1981)
	Fungi	Matrix mediated	Ferritin micelle	David and Easterbrook (1971), Peat and Banbury (1968)
	Plantae	Matrix mediated	Phytoferritin micelle	Hyde *et al.* (1963)
	Animalia	matrix mediated	Ferritin micelle	Ford *et al.* (1984)
Lepidocrocite (δ-FeOOH)	Porifera	Induced	Sponge granules	Towe and Rutzler (1968)
	Mollusca	Matrix mediated	Chiton teeth	Lowenstam (1967)
Goethite (α-FeOOH)	Mollusca	Matrix mediated	Limpet teeth	Lowenstam (1962b)
Amorphous Ferric oxides	Bacteria	Unknown	Variable or unknown	Ehrlich (1981)
	Protozoa	Unknown	Foraminiferal test cement	Towe (1967)

	Annelida	Matrix mediated (?)	Polychaete tube cement	Lowenstam (1972)
	Mollusca	Unknown	Gastropod gizzard plates	Lowenstam (1968)
Amorphous Ilmenite	Bacteria (?)	Induced	On surface of holothurian skin	Lowenstam (unpublished)
Sulfides				
Pyrite (FeS_2)	Bacteria	Induced	Forms extracellularly	e.g., Hallberg (1978)
Hydrotroilite ($FeS \cdot nH_2O$)	Bacteria	Induced	Forms extracellularly	e.g., Hallberg (1978)
Sulfates				
Jarosite [M-$Fe(SO_4)_2(OH)_6$]	Bacteria	Induced	Forms extracellularly, only known from lab exp.	Lazaroff *et al.* (1982)
Phosphates				
Amorphous Hydroferric	Annelida	Matrix mediated	Sternaspis div. sp. sternal shield	Lowenstam (1972)
Amorphous phosphate	Mollusca	Matrix mediated	Chiton teeth	Lowenstam (1972)
	Enchinode-rmata	Matrix mediated	Holothurian dermal granules	Lowenstam and Rossman (1975)

Table 1.1 Iron-containing minerals, phyletic occurrences, mineralization types and locations of biochemically precipitated iron [7].

1.2.4 Structural biomaterials

Among all the outstanding functions of these minerals serving in biological systems, the superior mechanical properties developed through diversification and

specialization have grabbed the attention of materials scientists. Nano- and Micro- scale hierarchical structures of some biominerals have been revealed and related to their functions; layers of calcium carbonate with organic binder in the mollusks shells contribute to their high strength as well as toughness and impact resistance; cylindrical rods of hydroxyapaptite with proteins afford rat tooth enamel its hardness and damage tolerance; silica in various shapes makes diatoms hard and malleable [8].

1.3 Abrasion resistant materials

1.3.1 Basics of abrasion resistance materials

The progressive loss of materials from the contacting surface of a body due to relative motion at the surface is called wear. Principal factors that influence wear include hardness, load, speed, surface roughness and temperature [9]. Various modes of wear have been defined, including adhesion, fatigue, erosion, corrosion and abrasion. When two surfaces are loaded against each other, not all of the surfaces are in contact due to the asperities on the surfaces. Adhesion wear occurs when the whole contact load is applied on small area of the asperities contacts. Some diffusion or crystal growth may even occur for ductile materials during adhesion wear. Fatigue wear on the surface results from the repeated cycles of stress from repeat sliding, rolling or impacting motions. Erosion is defined as damage caused by the impingement of sharp particles on an object. Erosion usually results in severe roughness on the surface. Corrosive wear is defined as a wear process that chemical or electrochemical reaction with the environmental predominates.

This process is strongly influenced by environment, materials and the presence or absence of a film such as a lubricant, or other contaminants.

Abrasive wear occurs when a harder asperity plough or cut through a softer one. Abrasive wear is defined as wear resulting from the penetration and ploughing-out of material from a surface by another body. There are two types of abrasive wear, two-body abrasive wear and three-body abrasive wear. Two-body abrasion, or cutting wear, is referred as abrasive wear when the abrading contact is a surface asperity on the mating part (Figure 1.2.A). Three-body abrasion occurs when the abrading contact is a free grit from external or a particle that has been produced within the system and which is loaded between the two surfaces (Figure 1.2.B). Three-body abrasion is more common in industry because of the environmental conditions.

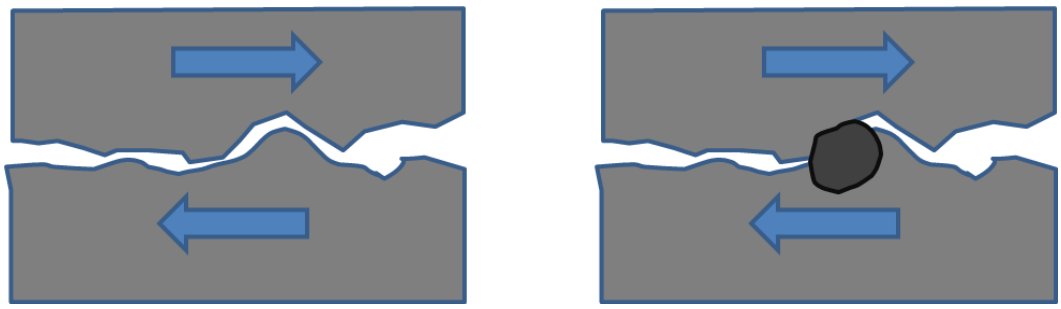

Two-body Abrasion Three-body Abrasion

Figure 1.2 Schematic of two-body abrasion and three-body abrasion.

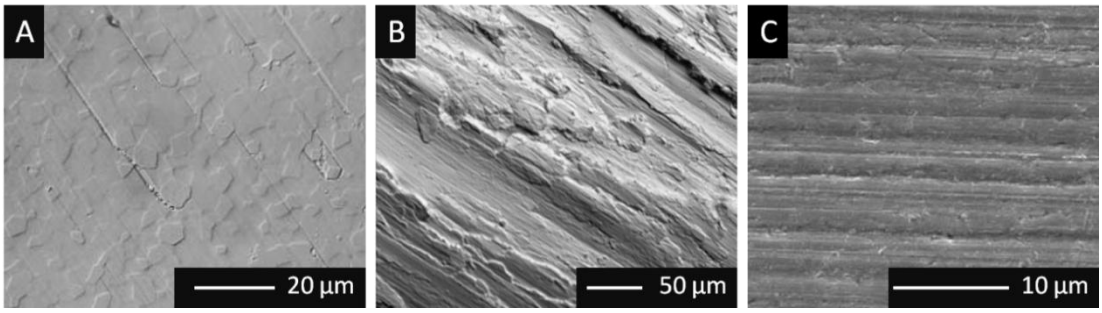

Figure 1.3 Examples of wear surfaces from three-body abrasion (A) [10], gouging wear (B) [11], and low-stress abrasion (C) [12].

The load is transmitted by the abrasive particles from one surface to the other in three-body abrasion. The load stresses at the contact point are very high due to the fact that the actual load supporting area is small and thus, the mean pressure of the whole surface is low. To achieve abrasion resistance, materials need to posses high hardness and structural integrity (Figure 1.3A). When the abrasive particles are large and heavy and the force is large enough to gouge out material, it is defined as gouging wear or abrasion (Figure 1.3B). With significant lateral stresses imposed on the surface and intermittent impact forces from the operation, materials to resist this gouging abrasion need to be not only hard but also tough. Low-stress abrasion usually occurs on solid-handling equipments like conveyors, chutes, vibrating screens, etc. (Figure 1.3.C). The crucial property for materials in this situation is only hardness because of the absence of impact for this case [9].

1.3.2 Assessment of abrasion resistance

Property maps of a wide range of materials have been constructed by Zok and Miserez in 2007. The solutions have been obtained based on the discussions on yielding

and cracking at blunt contacts, as well as a prescribed plastic penetration and cracking at sharp contacts, initiated by critical loads (Figure 1.4). These situations are also discussed with normal load P applied only, which means no friction, or with both normal load *P* and tangential load *Q*. The two loads are related by $Q=\mu P$ where μ is the friction coefficient. Maps of material property groups have been generated based on these discussions (Figure 1.5 and 1.6). For resistance to yielding at blunt contacts with no friction, ceramics have better performance than other engineering materials for rigid abrasives (Figure 1.5A), while stiffer materials are better for elastic abrasives (Figure 1.5C). For resistance to cracking at blunt contact with friction, ceramics are the worst, while metals and polymers are the best (Figure 1.5B). For resistance to cracking at sharp contacts without friction, soft metallic alloys are superior to other engineering materials (Figure 1.5D).

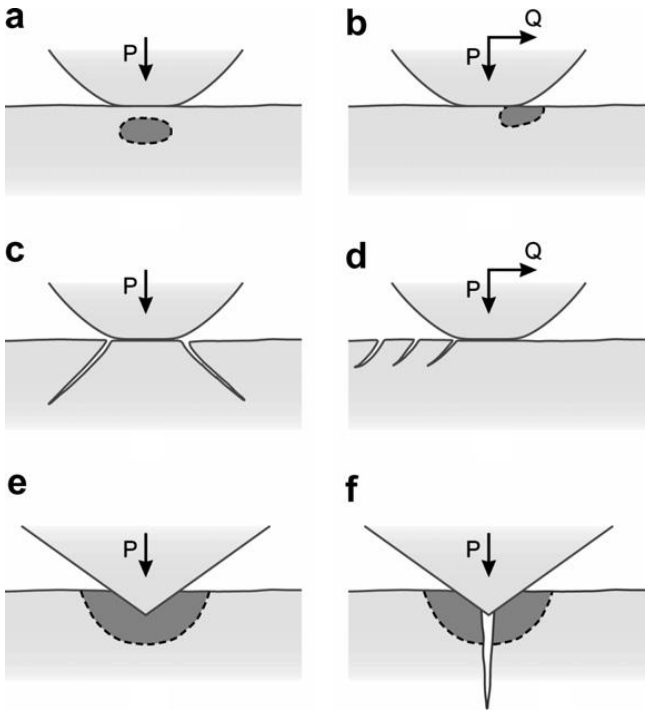

Figure 1.4 Damage mechanisms at contacts with blunt and sharp abrasives. Shaded areas represent yielding. For blunt contacts, two failure modes are considered: (i) onset of yielding (a, b); and (ii) formation of cracks prior to yield (c, d). When the contacts are sharp, yielding is unavoidable, even at low loads. Two additional criteria are used for assessment: (i) attainment of a critical plastic penetration depth (e), and (ii) formation of cracks within the plastic zone (f). Each criterion yields a dominant material property group that serves as a performance metric. Shaded areas represent yielding. P and Q represent normal and tangential loads separately [13].

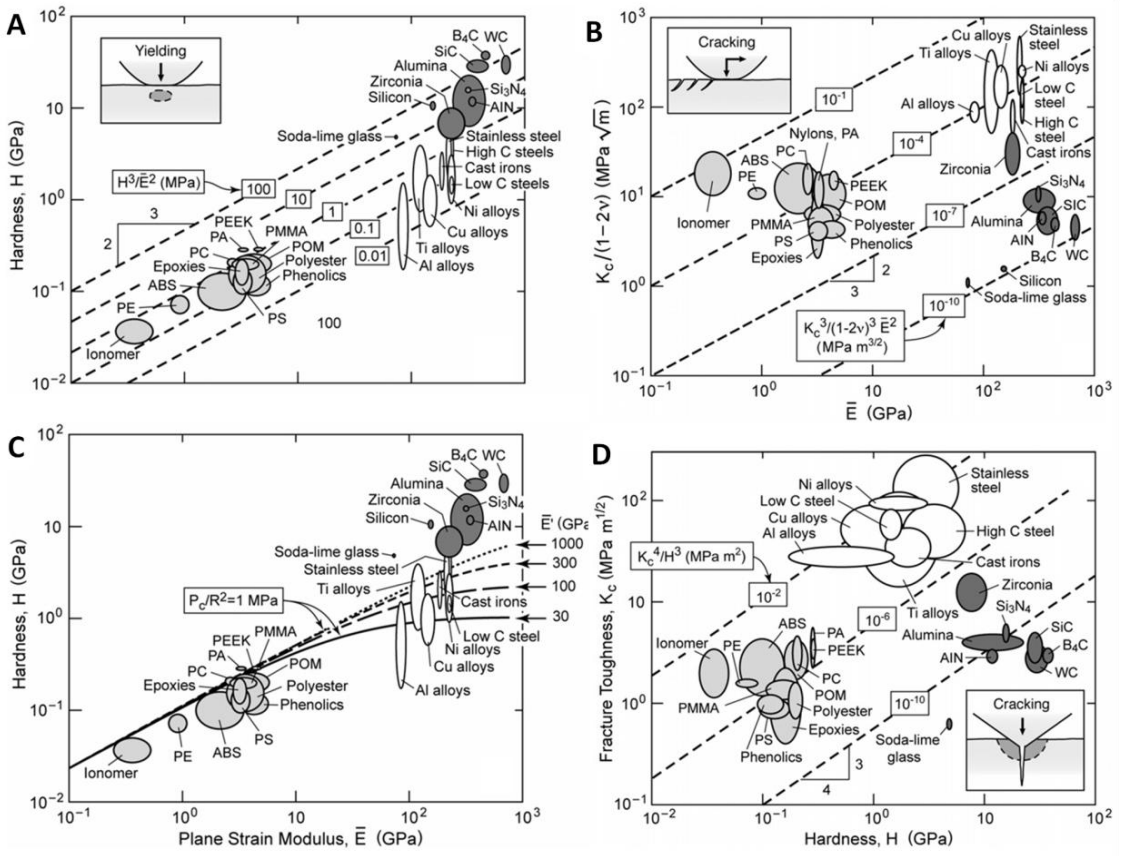

Figure 1.5 Property maps for resistance to yielding at blunt contacts with no friction, for rigid and (A) elastic abrasives (C). Property maps for resistance to cracking at blunt contacts with friction (B) and at sharp contacts without friction (D) [13].

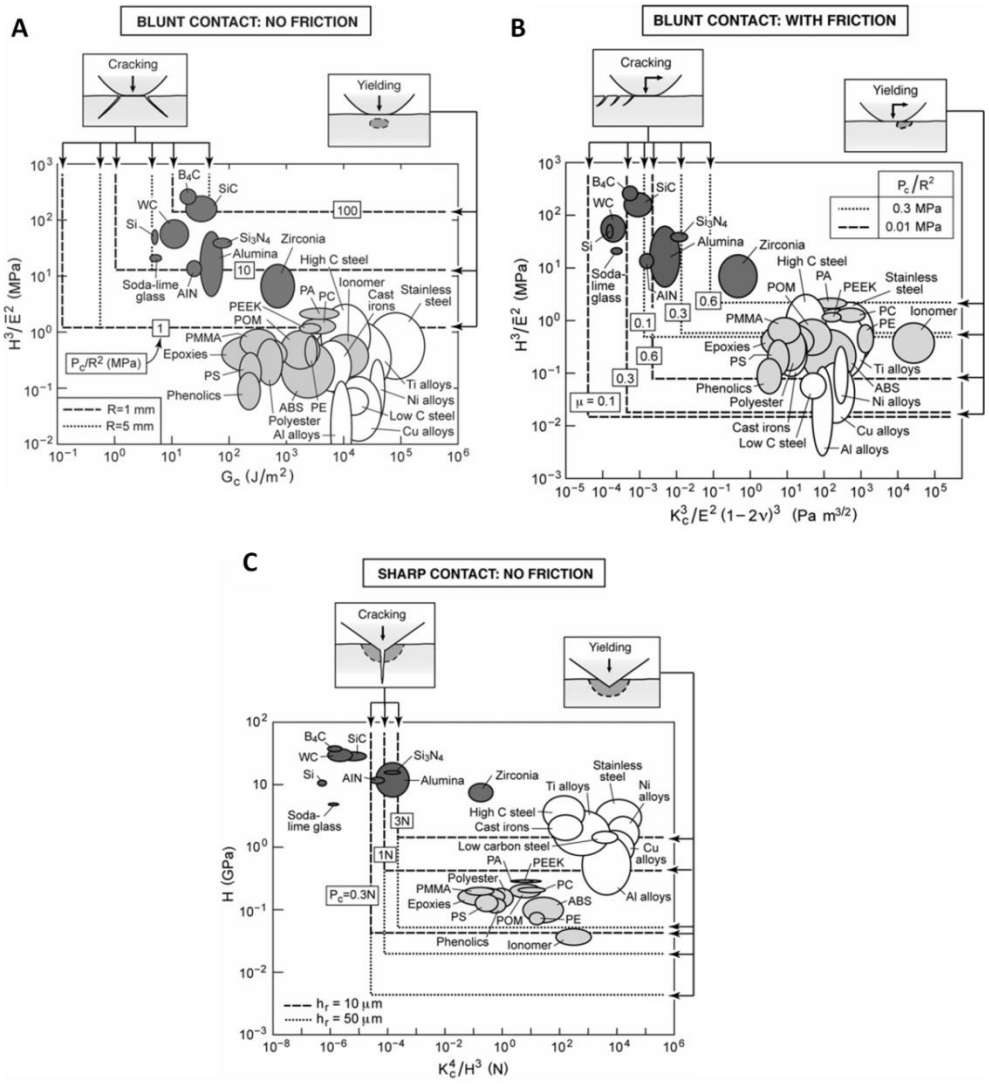

Figure 1.6 Property maps for resistance to cracking and yielding at blunt contacts without (A) and with friction (B), as well as plastic penetration and cracking at sharp contacts (C) [13].

1.4 Finite element analysis

1.4.1 Basics of FEA

As the basis of a multibillion dollar per year industry, finite element analysis (FEA) has become very common in recent years. FEA is the practical application of finite

element method (FEM), which is defined as a numerical technique that solves the differential equations by discretising the equations in their space dimensions. The discretization of the equation in the space dimensions is carried out locally over small regions of simple but arbitrary shapes called the finite elements. The approach transforms the differential equations to their equivalent matrix (linear algebraic) equations in terms of the values of variables at the nodes of the elements. The resulting linear algebraic equations are normally solved using computers (Figure 1.7).

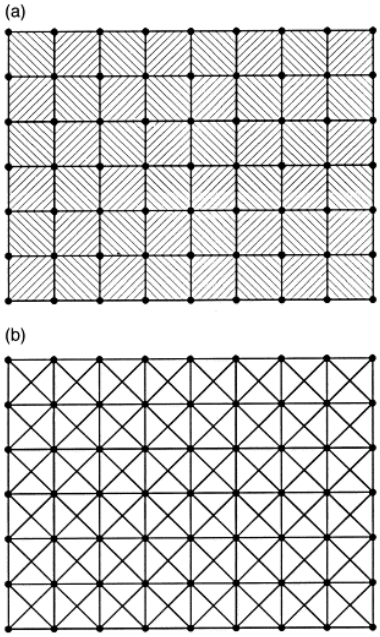

Figure 1.7 A finite element model and partial clique graph. (a) A finite element model. (b) Partial clique graph of FEM [14].

FEA uses a computer to construct models of materials or designs that are stressed and analyzed for specific results. FEA starts with constructing a complex system of points called nodes and making a grid called a mesh (Figure 1.8.A). This mesh is then

programmed to contain the material and structural properties, which define how the structure will react to certain loading conditions. The first development of FEA was in 1943, when R. Courant obtained approximate solutions to vibration systems with the Ritz method of numerical analysis and minimization. By the early 1970's, only the aeronautics, automotive, defense, and nuclear industries were able to afford the FEA with expensive mainframe computers. With the rapid decrease of the cost of computers and the phenomenal increase in computing power, incredible developments of FEA have been made and outstanding precision has been achieved. The supercomputers are now able to produce accurate results for all kinds of parameters. FEA nowadays are widely used in designing new products and refining existing products. A proposed design can be performed and verified with FEA prior to manufacturing or construction, in which way the cost is far less than actually build and test each sample [15].

1.4.2 Application examples of FEA

There are four common types of engineering finite element analysis, including structural, fatigue, heat transfer and vibrational. Two types of models are constructed for structural analysis, linear and non-linear. In the linear model, the parameters are simple and no plastic deformation occurs (Figure 1.8.B). In the non-linear model, the stressing of the materials will be over their elasticity and causes the variation of the materials (Figure 1.8.C). Fatigue analysis is performed with cyclic loading on the specimen and to predict the life of a material or structure. It can tell the path of the crack propagation, as well as the damage tolerance of the material (Figure 1.8.D). The conductivity or thermal fluid dynamics of the material or structure can be modeled with heat transfer analysis (Figure

1.8.E). Vibrational analysis is used to test reaction of materials facing random vibrations, shock, and impact (Figure 1.8.F). Resonance and subsequent failure may occur if the natural vibrational frequency of the material is activated.

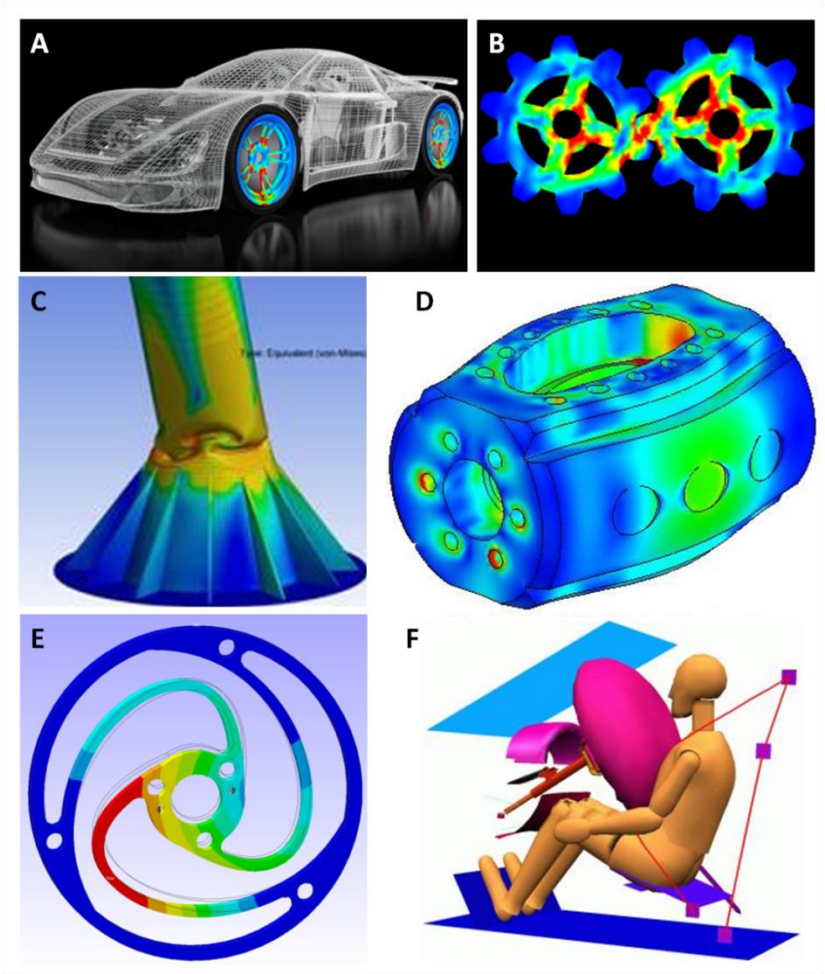

Figure 1.8 Application examples of FEA. A full mesh of the cover of a vehicle (A). Linear structural analysis of the deformation and stress distribution between two gears where the left gear is fixed but the right gear has an applied torque (B). A non-linear buckling modeled with Ansys (C). Fatigue analysis and weight optimization of a drum (D). Heat transfer analysis of a single part wheel suspension system (E). Vibrational analysis of airbag system of a vehicle (F).

1.5 Radula

1.5.1 Overview of radula

Radula, the teeth structure of mollusks, is found to be heavily mineralized and abrasion-resistant. The radula from chitons and limpets has attracted attention from scientists. Chitons, a group of elongated herbivorous mollusks, are protected dorsally by eight overlapping shell plates. The chitons graze for algae on hard substrates using a specialized rasping organ called the radula (Figure 1.7) [2, 16, 17], a conveyor belt-like structure located in the mouth (Figure 1.7A) that contains numerous parallel rows of mineralized teeth. Limpets are marine snails with a simple shell that is more or less conical in shape. They have the similar habitat and radula as chitons. Iron oxides minerals were found in the radula of both groups. During the feeding process, the first several rows of teeth at the anterior of the radula are involved in grazing and become worn. New teeth are continuously synthesized and enter the wear zone at the same rate at which teeth in the anterior-most row are shed from the growing ribbon, at a rate of 0.40, 0.36 and 0.51 rows per day for the chitons *Acanthopleura hirtosa* and *Plaxiphora albida*, and for the limpet *Patelloida alticostata*, respectively [18, 19].

The new teeth of radula are initially formed by synthesizing an organic matrix, which is subsequently mineralized with increasing tooth maturity. The mature teeth (i.e., fully mineralized) are used to rasp for food and finally fall off the radula ribbon because of wear. The superior epithelium surrounding the teeth is responsible for delivering the elements required for mineralization and producing materials that harden the radula.

Dramatic ultrastructure changes of the apical cusp epithelium have been observed concurrently with the onsite of the mineral in the teeth. Their cells die and the epithelium detach from the radula after the radula is hardened. A subradular membrane is secreted by the epithelium and serves as attachment of the epithelium and the radula. The membrane detaches from the radula after they going through a change of the reversal of tanning process [20, 21].

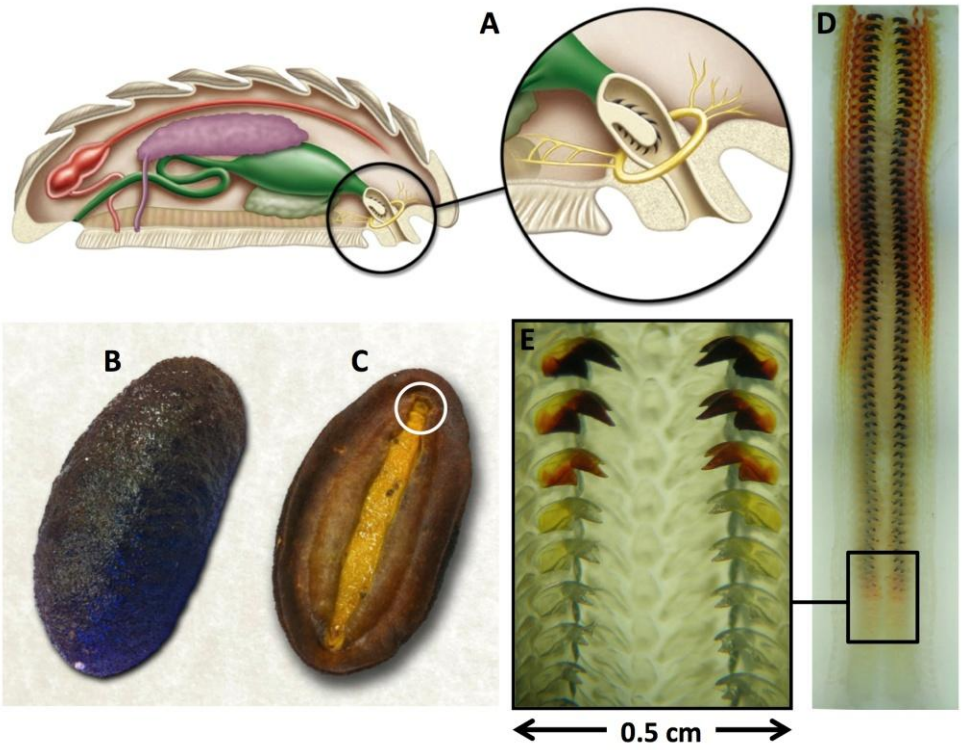

Figure 1.9 Chiton anatomy and gross morphological features of the radular teeth. (A) Diagrammatic lateral view of a representative chiton body plan, (B) dorsal and (C) ventral views of *Cryptochiton stelleri* (in this species, the characteristic overlapping shell plates shown in (A) are internal and thus not visible in the photo). The location of the mouth (which contains the radula) is circled in white. (D) Optical image of an entire radula from *C. stelleri*, containing more than 70 rows of parallel mineralized teeth. (E)

Transitional zone near the posterior end of the radula demonstrating a gradual change in tooth color from transparent to black, representing the earliest stages of mineralization.

Ferritin is the major iron storage protein during the mineralization of the radula in limpets and chitons. Ferritin aggregates, usually contained in sidersome, containing considerable amount of iron was found in the superior epithelium just before the onsite of the mineralization in the tooth cusp. Some of these aggregates pass through the microvilli and deliver iron into the cusp of the tooth for the formation of the iron mineralization [22, 23]. In *Acanthopleura hirtosa* and 18 other chiton species, ferritin was also found in the stylus canal, which appeared to be the other delivery pathway for the elements required for mineralization for the tooth cusp [24].

1.5.2 Previous studies of radula

Mature radular teeth usually consist a hard shell/ soft core structure. For limpets, the mineral in the outer shell is goethite, while the core is siliceous *[19, 22, 25-31]*. For chitons, the mineral contents vary in different species. In *Acanthopleura hirtosa*, the outer shell consists of magnetite while the core is made of calcium apatite; lepidocrocite and goethite are found at the thin layer between the core and shell [23, 24, 32-37]. In *Plaxiphora albida*, a magnetite containing shell and iron (III) phosphate core were claimed by Macey et al. in 1995 [38]. However, seven years later, in 2002 Lee et al. analyzed the mature teeth of *P. albida* with Raman microscopy and found that a narrow band of the hydrated iron (III) oxide limonite was shown to separate the magnetite of the tooth surface from a lepidocrocite and limonite containing central core region, without

separate iron phosphate mineral presented [39]. They argued that the high concentration of phosphorous observed by energy dispersive spectroscopy in the core region of the tooth in *P. albida* may come from the adsorption of phosphorous onto the surface of the iron oxides. XRD analysis through three species, *Acanthopleura echinata*, *Acanthopleura echinatum*, and *Chiton tuberculatus*, revealed a magnetite shell / apatite core separated by a thin lepidocrocite layer structure [40]. A veneer of ferrihydrite on the surface of the mature tooth of *Acanthopleura echinata* was detected with Raman microscopy [31]. In *Liolophura loochooana*, the anterior side is formed with lepidocrocite while the posterior side is consisted of magnetite [41]. Transformation of amorphous calicium phosphate to crystalline dahllite in the radular teeth of *Acanthopleura haddoni* was detected [42]. EDS analysis of radular teeth from *Cryptoplax striata* revealed that the mineralization starts with iron infiltration, followed by phosphorus and then calcium [43].

Magnetic properties of the major lateral radular teeth were investigated by X. Qian et al. They found that the teeth are easily magnetized along the long and wide axes, while the thickness axis is difficult to magnetize [44]. C.W. Li et al. studied growth of radular teeth of the chiton *Liolophura loochooana* using magnetic measurements and found the deposition of iron minerals started from the 7th row of teeth, with a maximum of 29 weight percent of magnetite detected at the 36th row. Subsequent teeth that followed decreased in mineral percentage due to abrading of the magnetite [41].

Paul van der Wal et al. suggested that self-sharpening characteristics of radular teeth could offer improvements to industrial cutting devices based on the shape, internal

structure, wearing pattern, feeding position, and distribution of hardness and elastic properties of these teeth [19]. This work provided a starting point to perform finite element analysis on the radular teeth.

1.5.3 Cryptochiton stelleri

The Gumboot Chiton, *Cryptochiton stelleri*, a common inhabitant of the rocky shores of the temperate Northeastern Pacific, is the world's largest species of chiton, reaching a maximum length of more than 30 cm (Figure 1.7B, C) [2, 16, 17]. The radula of *C. stelleri* contains more than 70 rows of mineralized and curved tricuspid teeth (Figure 1.7D). The fully mineralized radular teeth consist of an iron phosphate / magnetite core-shell structure that displays remarkable mechanical properties including the highest reported hardness and modulus of any known biomineral [45]. The organic matrix of these teeth consists primarily of α-chitin (a polymer of β-1, 4-linked N-acetylglucosamine units) and provides a three-dimensional structural framework onto which the mineral phases are precipitated. The resulting mature teeth exhibit a decreasing hardness and modulus from the leading to trailing tooth edges and due to asymmetrical wear patterns, creates a self-sharpening condition. This design affords the teeth the ability to withstand abrasion, impact, and fatigue during substrate rasping events, similar to conditions experienced by industrial machinery such as tunnel boring, oil drilling, shaping and machining tools [45].

Thus, the biomineralization process is paramount in driving the formation of the complex architecture of the radular teeth, which results in their distinct, region specific

mechanical properties. Since every stage of tooth development is contained within a single radula (Figure 1.7E), it thus provides an ideal model system for investigating the dynamic processes of biomineralization during tooth growth and maturation [23].

The radular teeth of *C. stelleri* were first studied by Towe and Lowenstam in the 1960s, who identified the presence of ferritin, in both crystalline and paracrystalline phases, as a likely shuttling vehicle for iron during tooth mineralization [46]. Lowenstam further showed that an open framework organic matrix was present in non-mineralized teeth and likely acted as a template for mineral deposition [47]. In 1979, Kirschvink and Lowenstam confirmed that during the earliest stages of mineralization in the outer margins of the teeth of *C. stelleri*, ferrihydrite was first precipitated and was later transformed to magnetite [20].

1.6 Objectives

An ultrastructural analysis and investigation of mechanical properties of fully mineralized radular teeth from *C. stelleri*, as well as the mineralization process of these teeth, has been performed to gain insights into structure-function relationships of the abrasion resistant, impact tolerant, and anti-fatigue composites synthesized by nature. Biomimicry work has been performed to verify our observations. Shape, wear patterns, and feeding positions of the teeth has been analyzed to provide teeth working conditions that can be used in finite element analysis modeling of the tooth, which helps to provide a foundation to produce abrasion-resistant, impact-tolerant and anti-fatigue materials.

1.7 References

[1] D. A. Thompson, *On Growth and Form*, The Univerisity Press, Cambridge **1942**.

[2] S. W. Heinz A. Lowenstam, *On biomineralization*, Oxford University Press, **1989**.

[3] M. A. Meyers, P. Y. Chen, A. Y. M. Lin, Y. Seki, *Progress in Materials Science* **2008**, *53*, 1.

[4] L. Addadi, S. Weiner, *Angewandte Chemie-International Edition in English* **1992**, *31*, 153.

[5] S. A. Stricker, S. Weiner, *Experientia* **1985**, *41*, 1557.

[6] B. Howard, P. C. H. Mitchell, A. Ritchie, K. Simkiss, M. Taylor, *Biochemical Journal* **1981**, *194*, 507.

[7] D. S. J. Joseph L. Kirschvink, Bruce J. MacFadden, *Magnetite Biomineralization and magnetoreception in organisms*, Plenum Press, New York **1985**.

[8] C. Santulli, *Proceedings of the International School on Advanced Material Science and Technology* **2004**.

[9] A. L. P. A. R. Lansdown, *Materials to resist wear: A guide to their selection and use*, Pergamon Press, Oxford **1986**.

[10] J. D. O. Barceinas-Sanchez, W. M. Rainforth, *Acta Materialia* **1998**, *46*, 6475.

[11] S. R. Bakshi, D. Wang, T. Price, D. Zhang, A. K. Keshri, Y. Chen, D. G. McCartney, P. H. Shipway, A. Agarwal, *Surface & Coatings Technology* **2009**, *204*, 503.

[12] G. Quercia, I. Grigorescu, H. Contreras, C. Di Rauso, D. Gutierrez-Campos, *International Journal of Refractory Metals & Hard Materials* **2001**, *19*, 359.

[13] F. W. Zok, A. Miserez, *Acta Materialia* **2007**, *55*, 6365.

[14] A. Kaveh, A. Bahreininejad, H. Mostafaei, *Computers & Structures* **1999**, *70*, 667.

[15] B. V. S. Nam-Ho Kim, *Introduction to Finite Element Analysis and Design*, Wiley, **2008**.

[16] J. C. E. Ricketts, *Between Pacific Tides: Fifth Edition*, Stanford University, Stanford **1985**.

[17] D. P. A. R. H. Morris, E. C. Haderlie, *Intertidal Invertebrates of California*, Stanford Press, Stanford **1980**.

[18] J. A. Shaw, D. J. Macey, L. R. Brooker, *Journal of the Marine Biological Association of the United Kingdom* **2008**, *88*, 597.

[19] P. van der Wal, H. J. Giesen, J. J. Videler, *Materials Science & Engineering C-Biomimetic and Supramolecular Systems* **2000**, *7*, 129.

[20] J. L. Kirschvink, H. A. Lowenstam, *Earth and Planetary Science Letters* **1979**, *44*, 193.

[21] S. M. Webb, *Physica Scripta* **2005**, *T115*, 1011.

[22] H. K. Lu, C. M. Huang, C. W. Li, *Experimental Cell Research* **1995**, *219*, 137.

[23] K. S. Kim, D. J. Macey, J. Webb, S. Mann, *Proceedings of the Royal Society of London Series B-Biological Sciences* **1989**, *237*, 335.

[24] J. A. Shaw, D. J. Macey, L. R. Brooker, E. J. Stockdale, M. Saunders, P. L. Clode, *Journal of Morphology* **2009**, *270*, 588.

[25] M. R. Carriker, J. G. Schaadt, V. Peters, *Marine Biology* **1974**, *25*, 63.

[26] M. S. Davies, D. J. Proudlock, A. Mistry, *Ecotoxicology* **2005**, *14*, 465.

[27] C. M. Huang, C. W. Li, M. C. Deng, T. S. Chin, *Ieee Transactions on Magnetics* **1992**, *28*, 2409.

[28] N. W. Runham, *Quarterly Journal of Microscopical Science* **1961**, *102*, 371.

[29] N. W. Runham, P. R. Thornton, D. A. Shaw, R. C. Wayte, *Zeitschrift Fur Zellforschung Und Mikroskopische Anatomie* **1969**, *99*, 608.

[30] D. A. Smith, *Journal of Experimental Biology* **1988**, *136*, 89.

[31] E. D. Sone, S. Weiner, L. Addadi, *Journal of Structural Biology* **2007**, *158*, 428.

[32] L. A. Evans, D. J. Macey, J. Webb, *Marine Biology* **1991**, *109*, 281.

[33] L. A. Evans, D. J. Macey, J. Webb, *Calcified Tissue International* **1992**, *51*, 78.

[34] A. P. Lee, J. Webb, D. J. Macey, W. van Bronswijk, A. R. Savarese, G. C. de Witt, *Journal of Biological Inorganic Chemistry* **1998**, *3*, 614.

[35] J. A. Shaw, D. J. Macey, L. R. Brooker, E. J. Stockdale, M. Saunders, P. L. Clode, *Microscopy and Microanalysis* **2009**, *15*, 154.

[36] M. Saunders, C. Kong, J. A. Shaw, P. L. Clode, *Microscopy and Microanalysis* **2011**, *17*, 220.

[37] M. Saunders, C. Kong, J. A. Shaw, D. J. Macey, P. L. Clode, *Journal of Structural Biology* **2009**, *167*, 277.

[38] D. J. Macey, L. R. Brooker, J. Webb, T. G. StPierre, *Acta Zoologica* **1996**, *77*, 287.

[39] A. P. Lee, L. R. Brooker, D. J. Macey, J. Webb, W. van Bronswijk, *Journal of Biological Inorganic Chemistry* **2003**, *8*, 256.

[40] Lowensta.Ha, *Science* **1967**, *156*, 1373.

[41] C. W. Li, T. S. Chin, J. S. Li, S. H. Huang, *Ieee Transactions on Magnetics* **1989**, *25*, 3818.

[42] H. A. Lowenstam, S. Weiner, *Science* **1985**, *227*, 51.

[43] D. J. Macey, L. R. Brooker, *Journal of Morphology* **1996**, *230*, 33.

[44] X. Qian, J. G. Zhao, C. L. Liu, C. H. Guo, *Bioelectromagnetics* **2002**, *23*, 480.

[45] J. C. Weaver, Q. Q. Wang, A. Miserez, A. Tantuccio, R. Stromberg, K. N. Bozhilov, P. Maxwell, R. Nay, S. T. Heier, E. DiMasi, D. Kisailus, *Materials Today* **2010**, *13*, 42.

[46] K. M. Towe, H. A. Lowenstam, M. H. Nesson, *Science* **1963**, *142*, 63.

[47] K. M. Towe, Lowensta.H.A., *Journal of Ultrastructure Research* **1967**, *17*, 1.

2 Chapter 2. Structure-Function Analysis of an Ultra Hard Magnetic Biomineral in the Radular Teeth of *Cryptochiton stelleri*

2.1 Introduction

Ever since early humans first used antler to shape stone tools via lithic reduction, we have been fascinated by the structural complexity and mechanical robustness of biominerals. The 19th century saw an explosion in the interest to catalog global biodiversity and through the course of these expeditions, many new species were discovered and the details of their skeletal systems were documented in exquisite detail (Figure 2.1). It was these detailed ultrastructural studies [1-3] that helped lay the groundwork for the modern field of biomineralization [4]. In more recent times, the availability of advanced instrumentation such as synchrotron x-ray diffraction and high resolution transmission electron and scanning probe microscopy in conjunction with the latest advances in genomics and proteomics have permitted significant progress into not only the nanoscale characterization of these materials, but also the factors regulating their controlled fabrication.

These biominerals display similar, and frequently superior, mechanical robustness to those exhibited by many engineering materials with similar chemical composition, such as structural ceramics. Biological systems have accomplished this feat through the demonstrated ability to control size, morphology, crystallinity, phase, and orientation of the mineral under benign processing conditions (near-neutral pH, room temperature, etc.).

They utilize organic-inorganic interactions and carefully controlled microenvironments that enable kinetic control during the synthesis of inorganic structures [5].

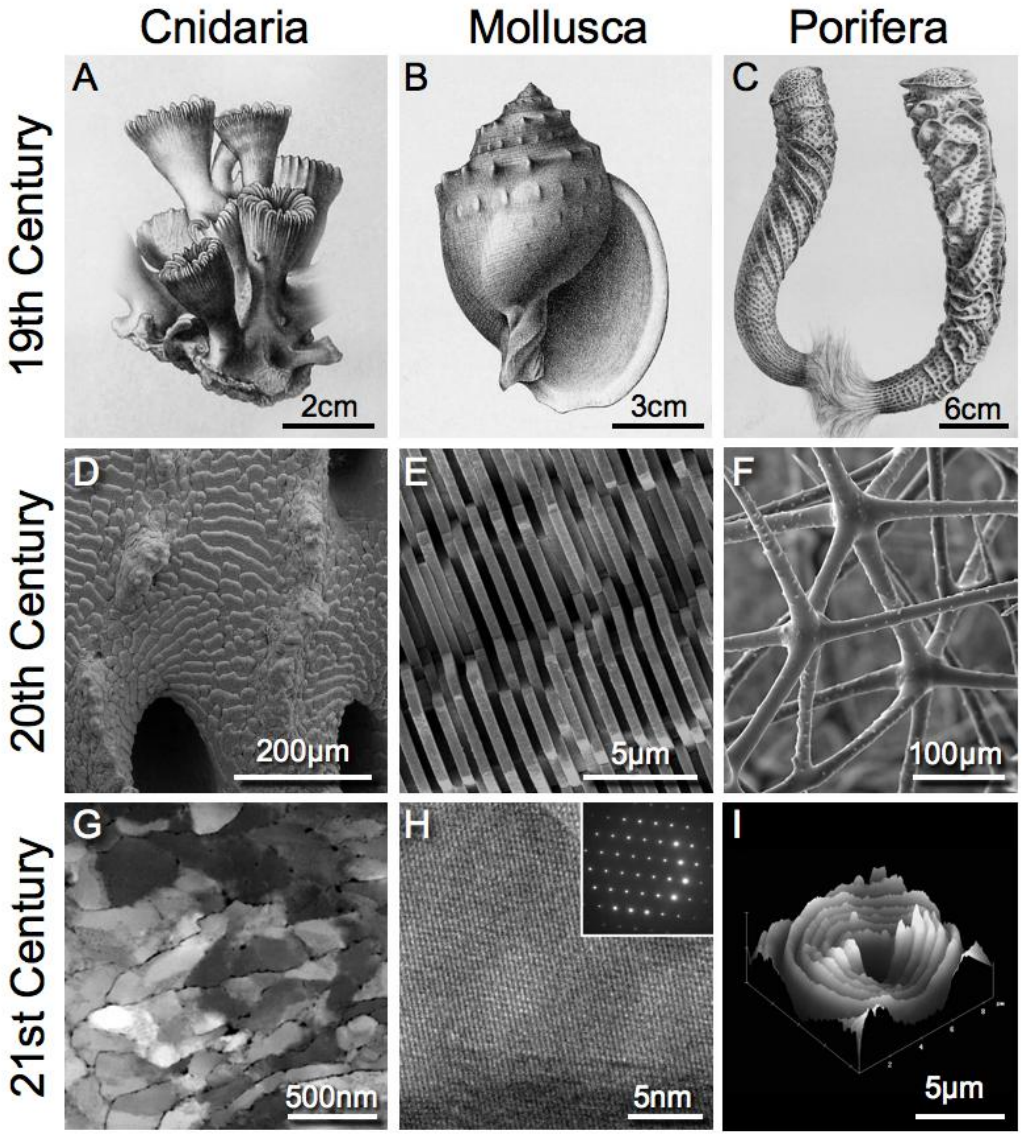

Figure 2.1 Evolution of the field of biomineralization through time.19th Century: Gross morphological skeletal anatomy of *Caryophyllia profunda* (a), *Cassis sp.* (b), and *Euplectella aspergillum* (c) collected during the Challenger expedition between 1873 and 1876. 20th Century: Electron microscopy studies of the aragonitic spherulites from *Aphrocallistes vastus* (d), mineralized tablets of nacre from *Haliotis rufescens* (e), and fused hexactine siliceous spicules from *Aphrocallistes vastus* (f). 21st Century: TEM

image of a focused-ion beam milled sclerite from *Corallium rubrum* (g), High resolution TEM and associated electron diffraction pattern of a single nacre tablet from *Haliotis rufescens* (h), and atomic force micrograph of the concentric lamellae of consolidated silica nanoparticles of a spicule from *Tethya aurantia* (i). (a-c) adapted from [1-3] and (g) adapted from [6].

In these biomineralized systems, minerals and organic macromolecules exist in close proximity and at nanoscale dimensions. Interactions at these interfaces are vital to the functions of structural materials found in nature such as shells, teeth, and bone[4]. Although the organic constituents of these biological composite materials are present in relatively small quantities[4], they significantly alter the mechanical behavior of the bulk structures. In organic-inorganic composites, the existence of the organic phase leads to significant energy dissipation at the interfaces during loading, resulting in a combination of properties that may well improve the abrasion and wear resistance of the structure in comparison to monolithic materials with equivalent chemical composition. Once such example is the hypermineralized teeth of chitons, which are shown to be harder and stiffer than any other known biomineral as discussed in detail below.

The chitons (Mollusca, Polyplacophora; Figure 2.2.A) are an ancient group of mollusks with a fossil record dating back nearly half a billion years. Despite their long and successful history and their ecological importance in rocky coastal habitats[1] they are a comparatively small group with about 650 modern species. Chitons are flattened and usually elongated mollusks that are protected dorsally by a shell consisting of eight overlapping plates. The foot is broad and powerful, well adapted for clinging tightly to the hard surfaces on which the animal grazes for algae. Like most other groups of

mollusks, the chitons have a radula (Figures 2.2.B and C), a rasping, toothed conveyor belt-like structure, which is used for feeding. The composition and morphology of the radular teeth vary from group to group and depend to a large extent on the dietary specifics and the mechanical properties of the substrates on which they feed [4, 7, 8].

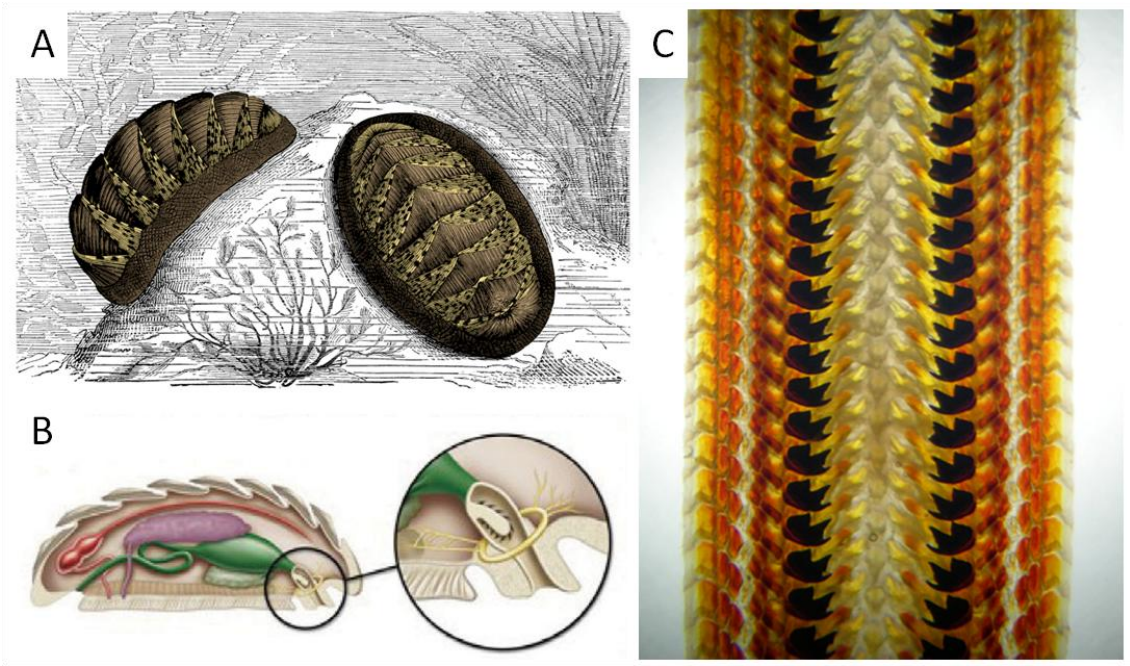

Figure 2.2 Morphological features of the chiton radula. External (A) and internal (B) anatomy of a representative chiton showing the location of the radula, a rasping, toothed conveyor belt-like structure used for feeding. Optical image showing the details of the anterior region of the radula from *C. stelleri* (C). (A) adapted from [9].

Cryptochiton stelleri is native to the temperate Northern Pacific and is the world's largest species of chiton, reaching a maximum length of up to 33cm [4, 7, 8], thus making it an ideal research system for investigating radular tooth architecture and mechanics. Despite its large size, the meat of this mollusk has no commercial value and is generally not considered palatable. This is exemplified in an account by Ricketts and Calvin [7]

who wrote, “After one experiment the writers decided to reserve the animals for times of famine; one tough, paper-thin steak was all that could be obtained from a large *Cryptochiton*, and it radiated such a penetrating fishy odor that it was discarded before it reached the frying pan.”

New radular teeth are continually secreted and shaped inside a specialized secretory organ, the radular sack, where they are fused with the underlying radular cuticle that maintains tooth alignment with respect to one another. Slow migration of the cuticle strip brings the newly formed teeth forward until they are in a functional position, at the anterior-most region of the radula [4]. Because every stage of tooth development is contained on a single radula, it represents an ideal model system for investigating the dynamic processes of biomineralization [4, 10-13].

Building on the pioneering work of Lowenstam and colleagues in the 1960s [5], our present study reports a detailed investigation of the unique properties of the radular teeth of *C. stelleri.* Lowenstam’s initial investigations into the architecture of the radular teeth from *C. stelleri* revealed that the tricuspid mineralized cap is a multi-component system consisting predominantly of an amorphous phosphate core covered with a hard veneer of magnetite. Although mineralogical analyses by Raman and EDS have been performed previously at various locations on radular tooth cross-sections [13], detailed elemental and mechanical maps during the tooth maturation process have not been reported.

In this work, we present a more detailed understanding of the mineralized radular teeth via nano-mechanical and elemental mapping in order to provide insight into the

important structural gradients that contribute to the unique impact and abrasion-resistant properties of this material.

2.2 Materials and Methods

2.2.1 Research Specimens

Live specimens of *Cryptochiton stelleri* were collected from Vancouver, British Columbia between October 2008 and March 2009 and maintained live in a recirculating seawater system until ready for use. The radulae were dissected from these specimens and rinsed in fresh seawater to remove any loose organic debris and immediately dehydrated through a graded series of ethanol treatments. Following complete dehydration to 100% ethanol, the anterior-most region of each radula (containing the fully mature teeth) was removed and embedded in Spurrs resin. The resin blocks obtained were polished to P1200 with progressively finer grades of silicon carbide paper and then with diamond lapping films of particles sizes down to 0.25 μm to obtain a smooth finish.

The resulting samples were examined either by nanoindentation, Raman spectroscopy, back-scattered and secondary scanning electron microscopy, or focused ion beam milled for transmission electron microscopy as described below:

2.2.2 Nanoindentation

Full-map indentation tests were performed on cross-sections through the tip and mid-region of the mature radular teeth from *C. stelleri* in ambient air using a Triboindenter nanomechanical testing system (Hysitron, Minneapolis, MN, USA) with either a berkovich or a cube corner tip at a peak force of 5mN. The load function

consisted of a 5-second loading to 5 mN, followed by a 5-second hold at that force, and then a 5-second unloading. The resulting indents in a grid-array measured ca. 12.5 μm apart and the hardness and reduced modulus were calculated from the unloading curve of each, using the Oliver-Pharr method [14]. Similar indentation measurements were also performed on the same tooth samples that had been hydrated with deionized water using rows of intents that crossed from the outer magnetite shell region into the iron phosphate core region. The measurements were performed to investigate the possible influence that sample dehydration might have on the measured mechanical properties. These results revealed that due to the highly mineralized nature of the teeth, there was on average only a ca. 15% reduction in both modulus and hardness within both mineral phases of the teeth in the hydrated vs. the dry state. For this reason, and to standardize measurements from sample to sample, all subsequent measurements were performed with dry samples.

The resulting modulus and hardness data were plotted using XYZ Plot (Hysitron) and the corresponding gradient maps were created by applying a Gaussian blur function to the resulting indentation maps, which were superimposed on the corresponding back-scattered electron micrographs. For comparative purposes, a profile of indents was also performed on polished sections of conch shells (*Strombus gigas*) using the procedures described above. Indents were also performed with a spherical tip (nominal radius 1 μm) on both the polished radula sections and a geological magnetite control at prescribed peak loads of 1 mN (0.1 mN/sec. loading rate) with a 5 second hold. Calibration of the tip radius was done by performing a series of indents on fused quartz (reduced modulus

69 GPa) in the elastic domain and fitting the loading curves with the Hertzian's solution. Best fit gave an actual radius of curvature of 400 nm.

2.2.3 Scanning Electron Microscopy and Energy Dispersive Spectroscopy

Polished tooth samples were gold coated and examined with a FEI XL-40 or a Tescan VEGA TS-5130MM scanning electron microscope equipped with an IXRF systems energy dispersive spectrometer. In addition to the polished sections, whole fractured teeth were also analyzed by SEM to identify their failure modes. Additional teeth were soaked overnight in a 5.25% sodium hypochlorite (NaOCl) solution to remove the organic phase. The resulting samples were then soaked overnight in DI water, mechanically fractured, rinsed briefly with ethanol and air dried for examination by SEM. Additional NaOCl-treated teeth were prepared, embedded and polished for nanomechanical testing as described above.

2.2.4 Transmission Electron Microscopy

Polished tooth cross-sections were prepared for TEM using a focused ion beam milling machine (Leo Gemini, 1540XB) to obtain thin sections measuring ca 100nm thick. The resulting foils were examined using a FEI-PHILIPS CM300 transmission electron microscope at 300 kV accelerating voltage.

2.2.5 Raman Spectroscopy

Polished tooth samples prepared as described above were investigated using Raman spectroscopy (λ_0= 780 nm) under low laser power conditions (6 mW) to minimize sample heating. Raman linescans were performed with mineral standards to help identify

the various inorganic phases present in the different regions of the teeth using a ThermoFisher DXR dispersive Raman microscope.

2.2.6 X-ray Transmission and Diffraction

For x-ray diffraction, the mineralized caps from the mature teeth of *C. stelleri* were individually mechanically separated from the supporting chitinous stalk, ground into a fine powder, and examined using a Philips X'PERT Powder Diffractometer with Cu Ka radiation.

Synchrotron x-ray transmission imaging was performed at beamline X13B at the National Synchrotron Light Source, Brookhaven National Laboratory, using 19 keV x-rays ($\lambda = 0.65$ Å) and a beam spot focused to ≈ 10 μm $\times 10$ μm. Specimens consisting of several radular teeth still attached to their basal membrane were mounted in the beam and scanned in 25 μm steps both parallel and perpendicular to the basal plane. Transmitted intensity was recorded using a photodiode detector fixed beyond the sample and normalized by incident intensity measured with an ion chamber.

2.3 Results and Discussion

Examination with backscatter SEM shows the infiltration of heavier elements into the teeth from the anterior region of the radula (Figure 2.3.A). The mature radular teeth are each composed of a mineralized tricuspid cap with a stalk-like flexible attachment to the base of the radula (Figures 2.3.B - D). Synchrotron x-ray transmission studies reveal the nature of the electron density distribution of materials in the mature tooth (Figures 2.3.B and C). These observations are also supported by backscattered electron

microscopy studies[13] where the tooth caps are significantly brighter compared to the background material of the stalk and basal supporting membrane (Figures 2.3.A and D).

Cross-sectional examinations by scanning electron microscopy (Figure 2.3.$D_{1, 2}$) and energy dispersive spectroscopy (EDS) of the radular teeth of *C. stelleri* reveal that they are composed of two distinct mineral phases [4, 15] (Figures 2.4.A - C). The core region of the teeth is enriched in iron phosphate and the exterior of the teeth in iron oxide (Figure 2.4). EDS analysis also reveals a significantly higher C content in the tooth core as well as small amounts of Ca, K, Na, Mg, and Si (Figure 2.4D). X-ray and electron diffraction (Figures 2.5.A and 2.7A) of the tooth exterior region reveal that it is composed of ferromagnetic iron oxide (magnetite) [4, 5, 16], while EDS, Raman spectroscopy [12, 13] and dark-field transmission electron microscopy of the tooth core material suggest the presence of weakly crystalline hydrated iron phosphate (Figures 2.6A and 2.7.B) [4, 5]. The iron phosphate rich core region of the radular teeth exhibits two intense Raman bands at 1050 and 1010 cm^{-1} along with weak bands at 1110 cm^{-1} and in the range of 400-700 cm^{-1} (Figure 2.6.A). It is generally accepted that the stretching and bending vibrations of phosphate groups occur at 1000-1200 and 400-700 cm^{-1}, respectively. The Raman peaks of crystalline materials are typically sharp and well separated in the regions of 900-1200 cm^{-1} and 100-400 cm^{-1} [17, 18]. In contrast, the Raman peaks of amorphous / nanocrystalline materials are wider, weaker and typically not well resolved for the vibrations from the phosphate roots or iron-oxygen, which is consistent with our analyses of the core region of the radular teeth (Figure 2.6.A). The raman spectra also suggest a large α-chitin component in the core material (Figure 2.6.A)

and TEM studies reveal the presence of abundant chitin fibers throughout this region (Figure 2.7.D) [19, 20].

Transmission electron microscopy analysis of focused ion beam-milled samples from both the core region (Figure 2.7.D-F) and the outer magnetite shell region (Figure 2.7.A-C) confirm both the rod-like orientation of the magnetite crystallites and the weakly crystalline, organic rich nature of the core material. Selected area electron diffraction and dark-field imaging of the outer magnetite shell also reveal that although the magnetite crystallites (each of which measure ca. 30 nm in diameter) are organized into aligned rod-like columns, there is no preferred orientation of the constituent crystallites (Figure 2.7B). In contrast, the diffuse electron diffraction pattern of the tooth core material clearly demonstrates the weakly crystalline form of the iron phosphate phase (Figure 2.7E).

In addition, EDS point scans across focused ion beam milled samples of the tooth core material reveal the presence of isolated domains of silica. These siliceous domains appear more electron transparent in TEM studies compared to the comparatively electron dense surrounding hydrated iron phosphate (Figure 2.8.) [4, 5].

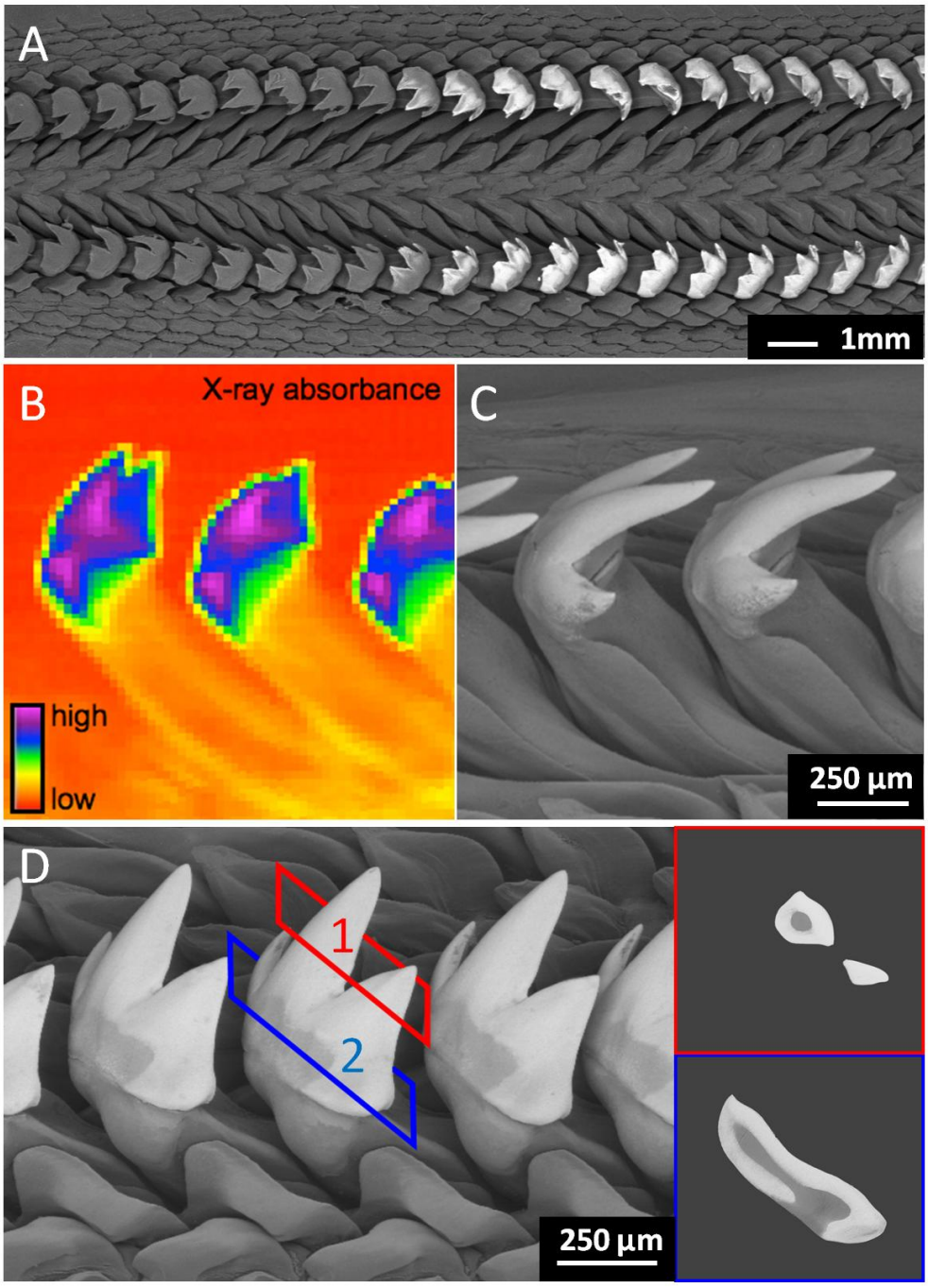

Figure 2.3 Backscattered SEM imaging of the posterior region of the radula from *C. stelleri* shows mineral infiltration (A). X-ray transmission studies of several teeth at the anterior region reveal the nature of the electron density distribution of the tricuspid tooth caps. Cross-sectional studies through the mature teeth from C. stelleri ($D_{1,2}$) reveal a concentric biphasic structure.

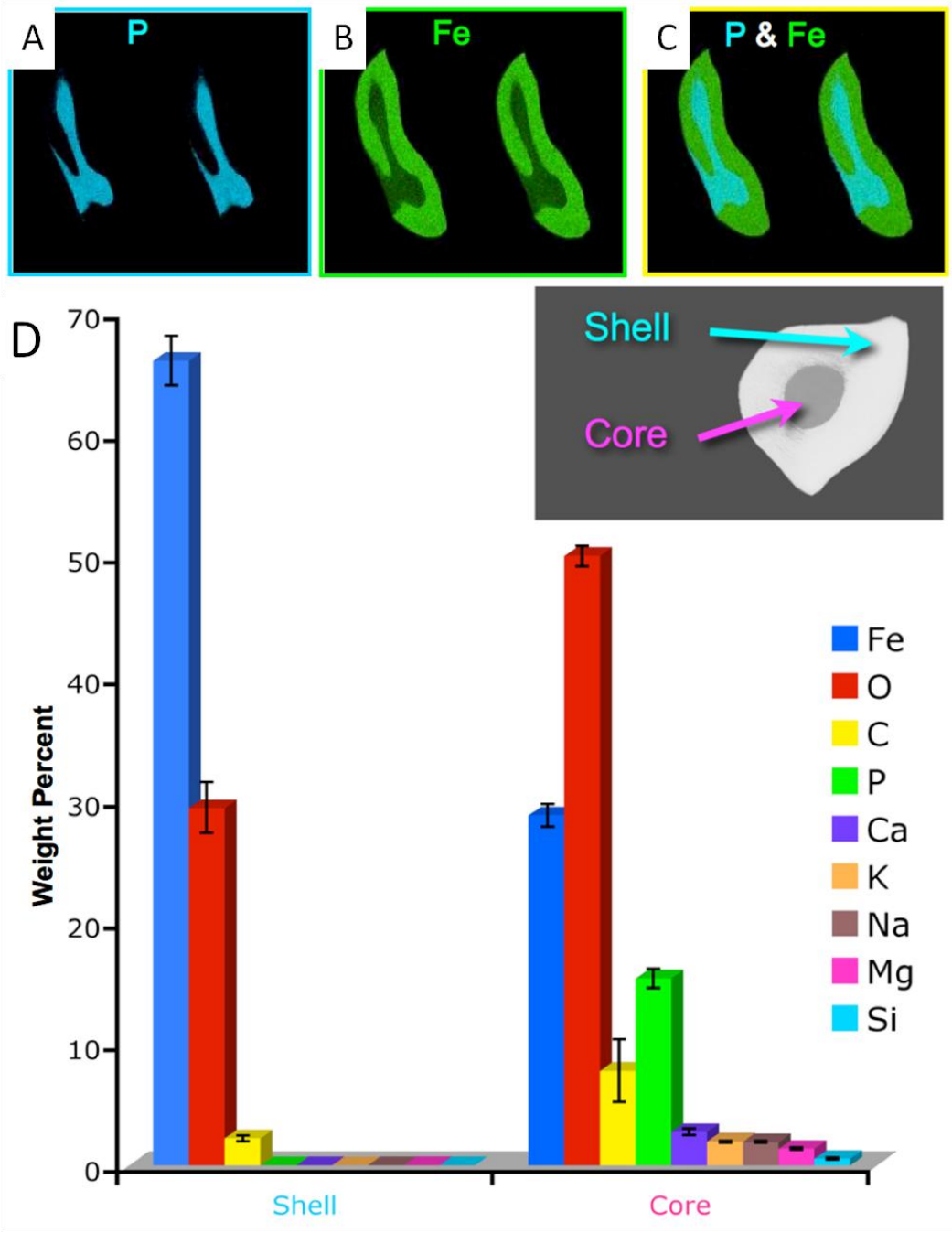

Figure 2.4 Elemental analysis of the radular teeth from *C. stelleri*. EDS mapping of the cross-section of the mature radular teeth (A) reveal an iron phosphate core surrounded by a thick veneer of iron oxide. A significantly higher C content in the tooth core as well as small amounts of Ca, K, Na, Mg, and Si is revealed (B).

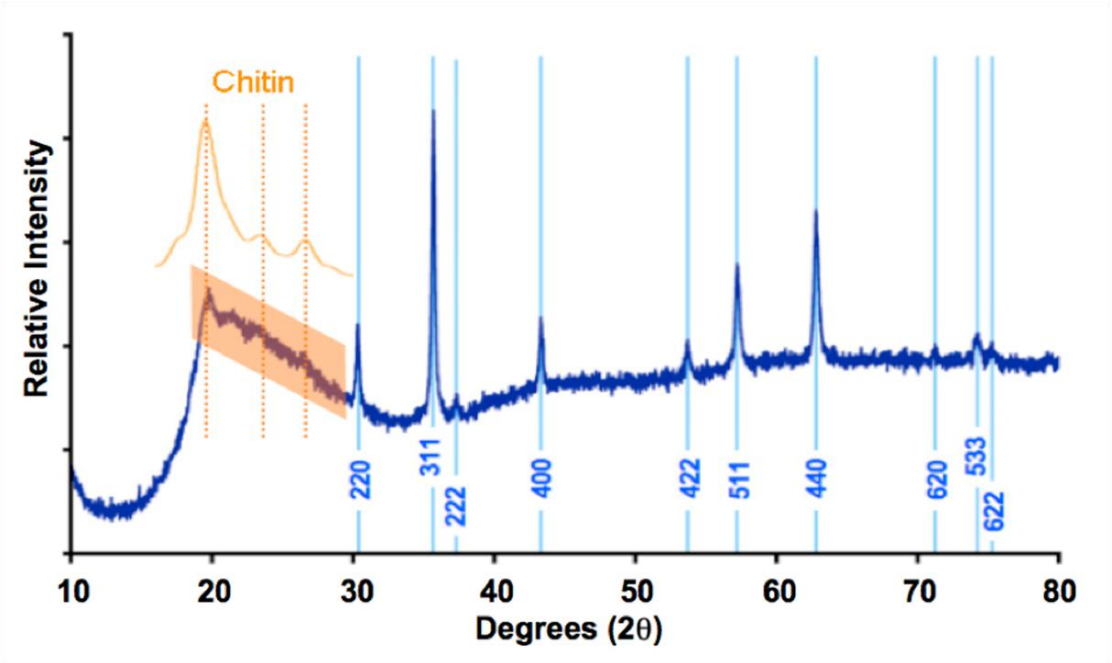

Figure 2.5 XRD analysis of the radular teeth from *C. stelleri*. Powder XRD suggests the presence of α-chitin and magnetite as the dominant crystalline phases. A chitin reference pattern[21] is shown in orange and miller indices of magnetite are labeled in blue.

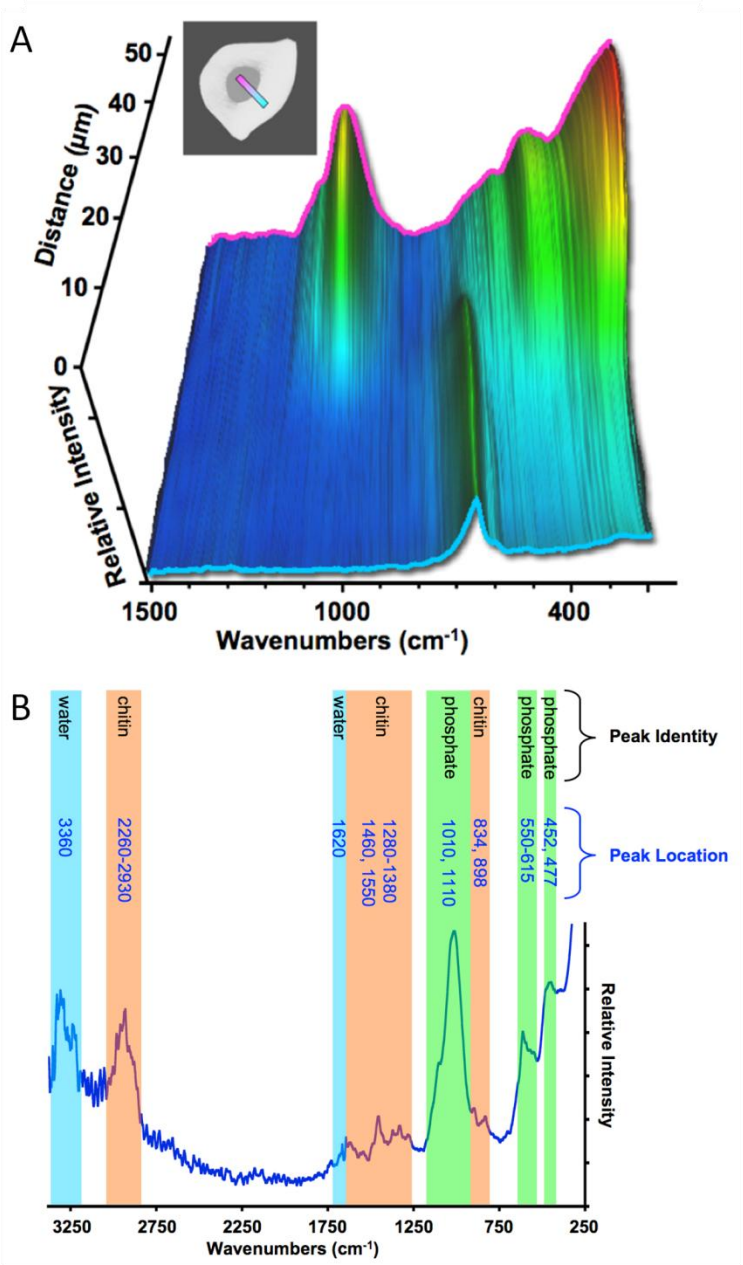

Figure 2.6 Raman Spectroscopy identifies the two likely mineral phases in the shell and core regions as magnetite and hydrated iron phosphate, respectively. A Raman linescan (A) through the region highlighted in the backscattered SEM image illustrates the transition zone between the two mineral phases. The dominant peak in the blue spectrum at 670 cm^{-1} corresponds to the ν Fe-O vibration of magnetite while the dominant peak in the pink spectrum at 1010 cm^{-1} corresponds to the ν P-O vibration of iron phosphate. A higher resolution raman spectrum of the radular tooth core material with the labeled peaks corresponding to α-chitin, phosphate and water is shown in 2D plot (B).

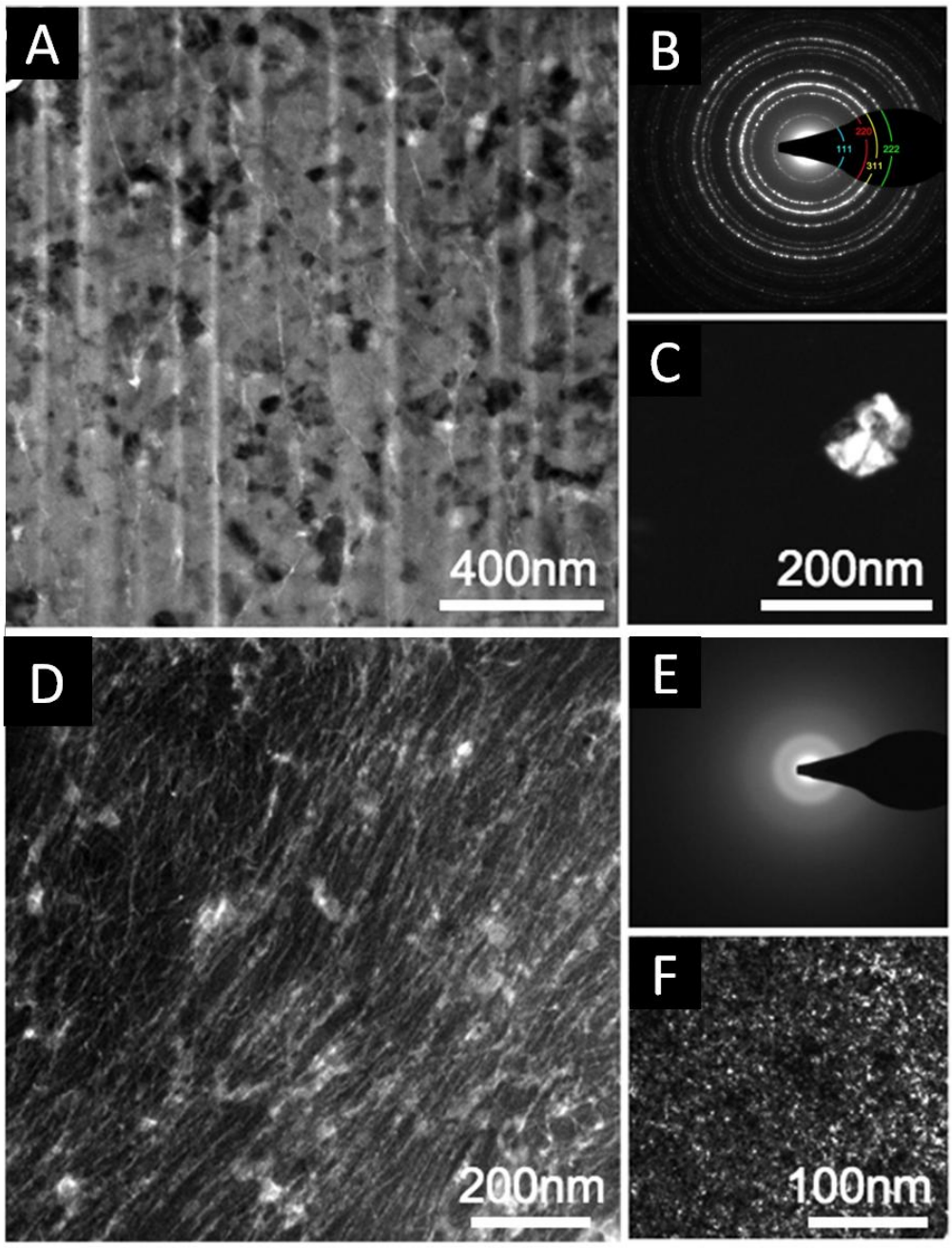

Figure 2.7 TEM analysis of the structure and phase in the shell and core regions of radular teeth of *C. stelleri*. TEM bright-field (A), selected area electron diffraction (B), and dark-field (C) studies of focused ion beam milled tooth sections through the magnetite shell region show the highly parallel nature of the magnetite crystallite bundles (A). TEM bright-field (D), selected area electron diffraction (E), and dark-field (F) studies of the core region of the same sample reveal organic-rich fibrous core material, and the weakly crystalline nature of the associated mineral phase (D).

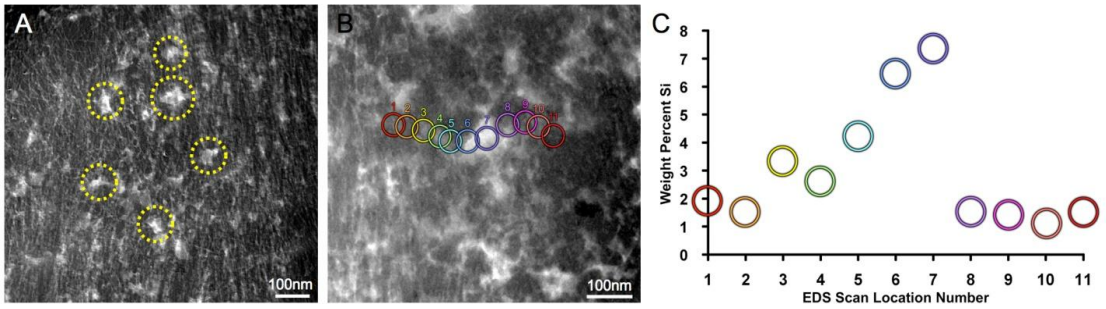

Figure 2.8 In focused ion beam milled samples isolated from the radular tooth cores, randomly dispersed domains of electron transparent material are routinely observed (A). To investigate the nature of these domains (some of which are indicated by dotted yellow circles in A), EDS point scans were performed to look for variability in elemental composition (B). The results from one of these measurements are shown in (C). EDS elemental point spectra reveal that these electron transparent regions contain elevated quantities of silicon compared to levels observed in the background material. These results indicate that while the radular teeth of C. stelleri do in fact contain silica as has been reported previously [4, 5], the siliceous material is phase segregated from the bulk core material of weakly crystalline hydrated iron phosphate.

Nanomechanical analyses of polished cross-sections through both the tooth tip and mid-region reveal that the two mineral phases (the magnetite veneer and the core of weakly crystalline hydrated iron phosphate – see Figure 2.3.D) exhibit distinct mechanical properties (Figure 2.9.A). The magnetite veneer has a modulus ranging from 90 to 125 GPa and a corresponding hardness ranging from 9 to 12 GPa. To the best of our knowledge, these values represent the highest modulus yet reported for a biomineral [21]. The hardness is notably about 3 times higher than that of enamel and nacre, which exhibit indentation hardness and modulus of 3 - 4 GPa and 65 – 75 Gpa [21], respectively, making this material exceptionally well suited for the continuous scraping activity of the radular teeth. In contrast, the weakly crystalline core region has a modulus of ca. 25 GPa and a hardness of ca. 2 GPa. Mechanical mapping of cross-sections through these two

regions of the teeth reveals a distinct gradient in mechanical properties with the modulus of the leading edge of the tooth ca. 15% higher than that on the trailing edge. This design strategy results in an uneven wear pattern along the scrapping edge of the tooth and establishes a self-sharpening condition (Figure 2.9.B), an observation consistent with radula structural studies on other species [22].

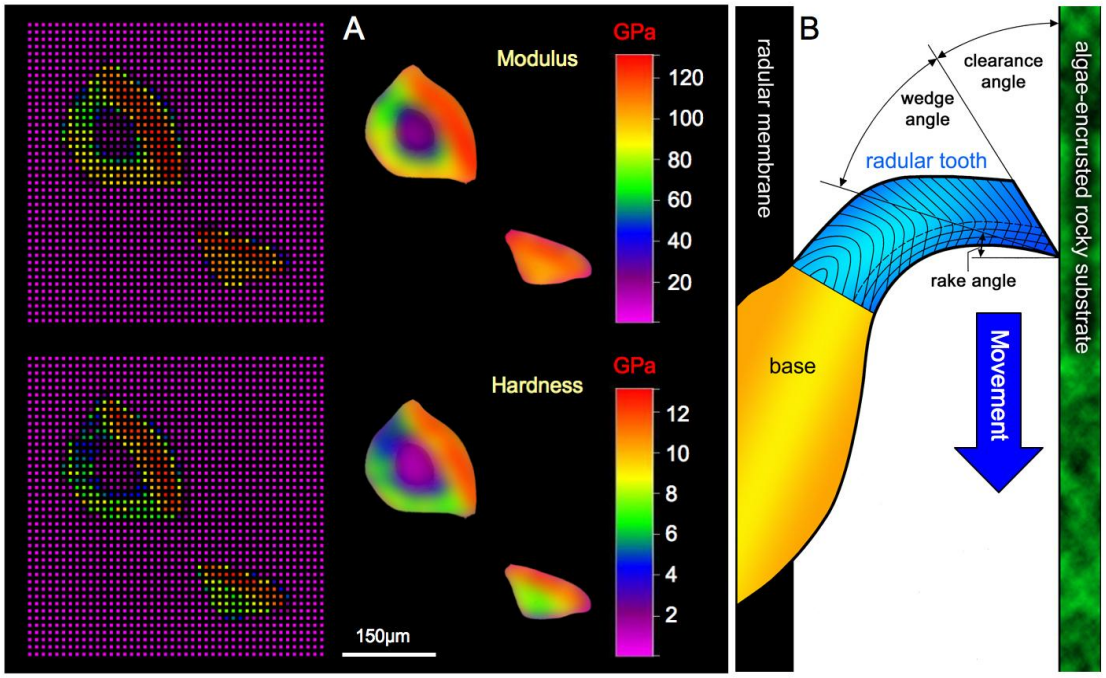

Figure 2.9 Nanomechanical testing of radular tooth cross-sections from *C. stelleri*. (A) Indentation (left) and the corresponding gradient (right) maps of modulus (upper) and hardness (lower) through a tooth tip and mid-region reveal that the leading edge of the tooth has a higher modulus and hardness than the trailing edge, thus establishing the self-sharpening condition illustrated in (B). The direction of tooth movement against the substrate is indicated by the blue arrow. (B) adapted from [22].

Indentation fracture studies of the magnetite veneer reveal that cracks propagating through this material usually travel parallel to the surface of the tooth rather than

perpendicular to the surface (Figure 2.10.B). In contrast, cracks propagating through the tooth core are largely isotropic and lack any defined directionality (Figure 2.10.A). In addition, as a propagating crack passes across the boundary between the core material and the outer magnetite shell, significant crack deflection occurs at this interface (Figure 2.10.A) because of the stress redistribution occurring either from small-scale yielding of the thin organic layers, or from debonding at the organic/mineral interface, with the latter mechanism being more efficient in protecting the uncracked material across the interface [23] (Figure 2.10.A). This strategy of crack deflection is very effective at maintaining the tooth structural integrity and preventing catastrophic failure of the material. Examination of fractured tooth cross-sections reveals how the organization of the magnetite crystallites facilitates this mechanical response (Figure 2.10.C).

Scanning electron microscopy of these fractured surfaces reveals that the magnetite is organized into ca. 250 nm wide bundles of crystallites that are oriented parallel to the long axis of the teeth, each of which is surrounded by a thin organic layer [5].

While the hardness and modulus of the teeth are directly related to the intrinsic mechanical properties of the constituent mineral phase, indentation fracture measurements of sodium hypochlorite-treated teeth reveal that following destruction of the tooth organic matrix, the fracture toughness drops precipitously, while the modulus and hardness remain largely unaffected (<15% reduction). This illustrates the important point that structural integrity can be attained only in the presence of the organic matrix that facilitates the anisotropic organization of the magnetite crystallites, binds them into a

composite structure, and plays a critical role in crack blunting and deflection at interfaces [24]. The highly mineralized nature of the external magnetite region of the radular teeth is exemplified by its low organic content (ca. 2%) compared to the core iron phosphate region (ca. 8%).

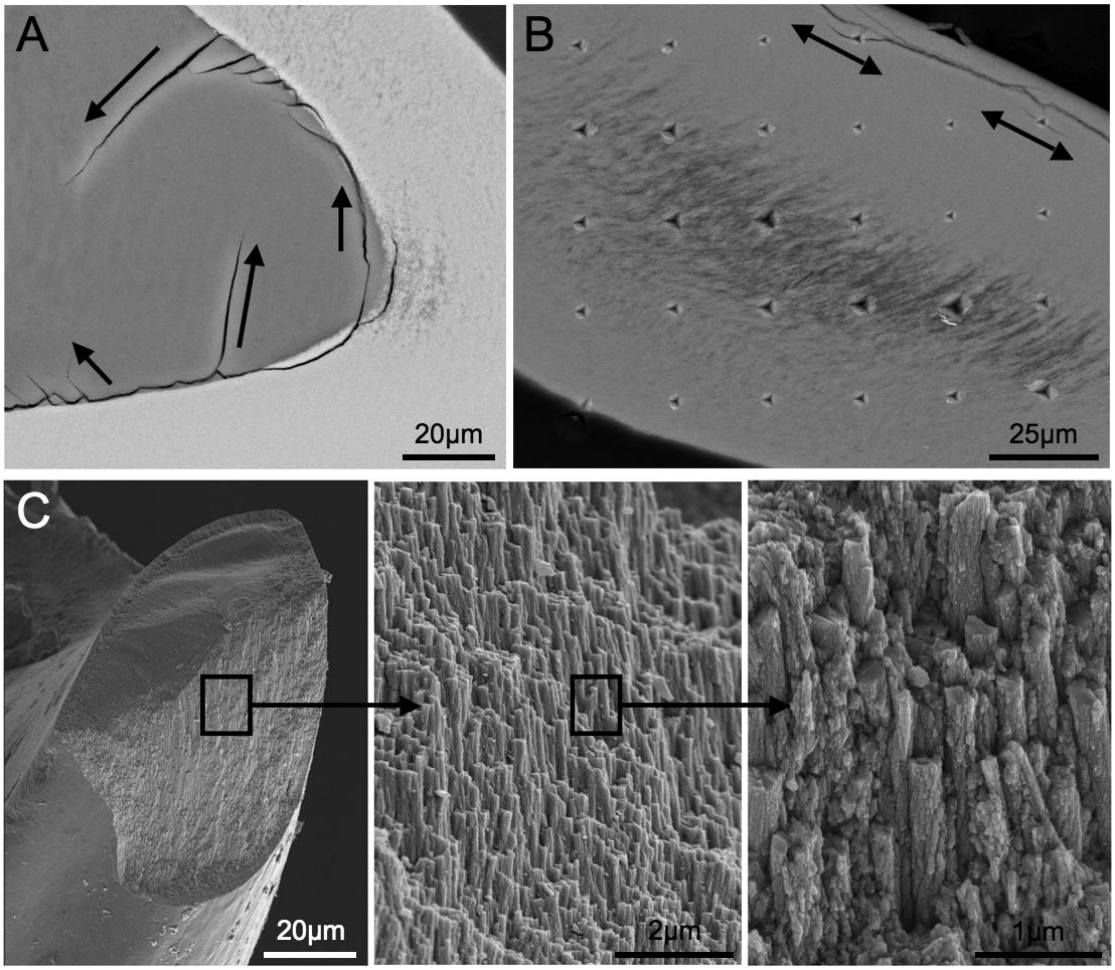

Figure 2.10 SEM analysis of failure modes in the radular teeth of C. stelleri. While crack propagation through the tooth core is isotropic (A), those propagating through the outer magnetite shell travel parallel to the long axis of the teeth (B). SEM analysis of a fractured tooth (C) reveals its closely packed rod-like ultrastructure.

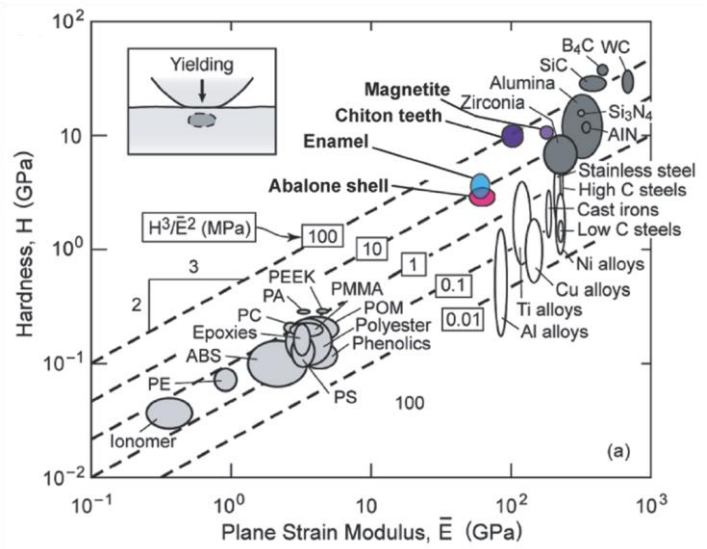

Figure 2.11 Property map resistance of yield damage (stiff abrasive) for various materials (adapted from [24]) predicts that the radular teeth perform better than known biominerals against a spherical contact and approaches that of the hardest engineering ceramics.

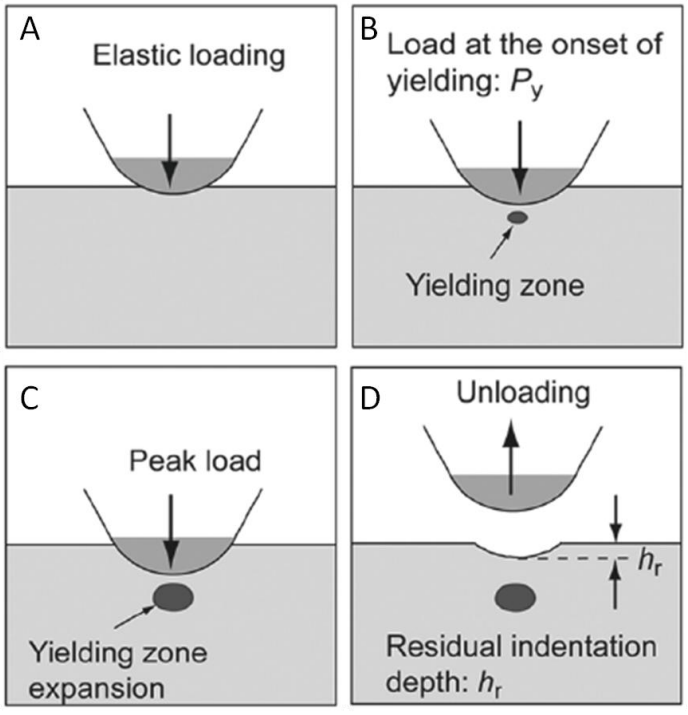

Figure 2.12 Schematic description of yield initiation beneath the contact during a normal loading/unloading cycle.

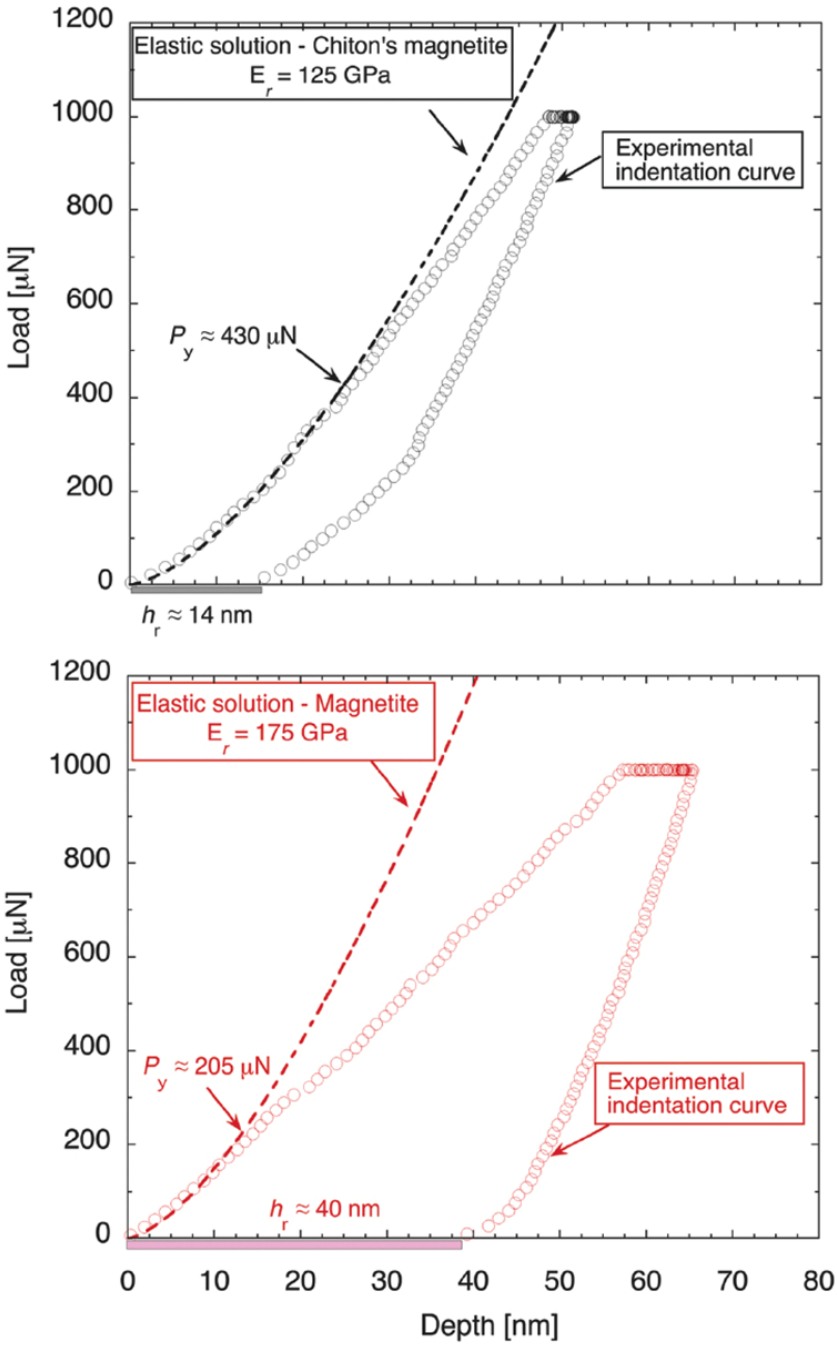

Figure 2.13 Representative indentation curves with a spherical tip on the radular teeth and a geological magnetite control: deviation from the elastic Hertzian solution corresponds to incipient yielding and confirms that the radular teeth have a higher critical load (in agreement with Py α H3/E2), while its residual impression, hr, is smaller at that peak load.

To gain additional insight into the abrasion resistance of the radular teeth from *C. stelleri*, we plotted the *E/H* combination on an Ashby-type plot that compares the abrasion tolerance of a wide range of materials (Figure 2.11). Here the guidelines correspond to abrasion damage by localized plastic deformation against a blunt and rigid contact (Figure 2.12), for which the critical normal load for yielding P_y (according to Hertzian contact mechanics) is proportional to the materials property group [25], $P_y \propto H^3/E^2$. Hence by plotting *E* vs. *H* values on a log-log plot, materials lying on lines with a slope of 2/3 are predicted to perform equivalently against yield damage at the contact.

Based on these criteria, we predict that the radular teeth of *C. stelleri* perform better against wear damage than the hardest known biominerals: enamel and nacre. Perhaps even more remarkable, the predicted abrasion resistance against a blunt contact exceeds that of zirconia (ZrO_2, a common ceramic used in load-bearing applications) [26] and is equivalent to the hardest structural ceramics such as silicon carbide (SiC) and boron carbide (B_4C). For reference, a geological magnetite mineral standard is also shown on the plot. Interestingly, the latter exhibits hardness values (10.5 ± 0.2 GPa) equivalent to the radular teeth of *C. stelleri*, but is significantly stiffer (175 GPa), i.e., 1.6 to 1.9 more stiff than the radular teeth. Small-scale sliding at the mineral/organic interfaces during external loading is a plausible cause to explain the larger compliance of radular tooth magnetite. From the materials selection plot, one expects the radular tooth magnetite to exhibit a higher tolerance to abrasion, here expressed in terms of residual indentation depth after contact loading, i.e., the smaller the residual depth, the better abrasion

resistance. We performed indentation curves with a spherical tip (nominal tip radius 1 μm) on the two materials to verify this assertion up to normal peak load of 1 mN. Representative curves are presented in Figure 2.13, together with the predicted curves from the elastic Hertzian solution (with the actual radius tip calibrated from indentation curves on fused quartz in the elastic domain). Since deviation from the elastic solution corresponds to the onset of yielding, comparison between the elastic solution and the obtained experimental data allows detection of the critical load at yielding [27]. The data and analysis confirm that (1) the critical load at yielding is indeed higher for the radular teeth as predicted from the index $P_y \propto H^3/E^2$, and (2) the residual indentation depth h_r of the radular teeth after incursion at a peak load of 1 mN is smaller, resulting in a better tolerance to abrasion than geological magnetite (in the absence of friction).

When abrasion is produced by sharp stiff particles, plastic deformation initially occurs at the contact and the abrasion resistance approximately scales with the hardness[25]. In such a case, the radular teeth from *C. stelleri* again outperform all other known biominerals. But yielding can be quickly followed by cracking at the contact in brittle materials [24, 27-29], and micro-cracking becomes the dominant wear mechanism. It can be shown that abrasion damage is then proportional to the material property group $K_{Ic}^4/H \cdot E^2$ where K_{Ic} is the fracture toughness [30]. Hence, a moderate increment of fracture toughness significantly improves the abrasion resistance (power-law exponent of 4). While K_{Ic} of radular tooth magnetite still awaits experimental determination, it is anticipated that its complex hierarchical microstructure toughens the structure against catastrophic fracture in comparison to monolithic magnetite, much to what has been

established for hierarchical calcium carbonate microstructures of nacre and conch shells [31, 32]. Additionally, tolerance to abrasion is proportional to the factor $1/H{\cdot}E^2$. Table 2.1 compares this index (as well as those discussed earlier) with literature values for various biominerals and engineering ceramics. These data suggest that the radular teeth from *C. stelleri* perform as well as hard ceramics, but appear less tolerant to microcracking from a sharp abrasive than enamel or mollusk shells. Knowledge of the radular tooth's fracture toughness, however, will be necessary to confirm this prediction. These results emphasize the importance of the geometry of the contact in defining the abrasion tolerance of biominerals. A comprehensive experimental study of wear at the micro-scale will be present in chapter 4.

	H [GPa]	**E [GPa]**	**H^3/E^2, [GPa]**	**$1/H\,E^2$ [GPa^{-3}]**	**References**
Radular teeth from *C. stelleri*	9 – 12	90 - 125	0.10 – 0.14	$7{\cdot}10^{-6}$ – $1{\cdot}4{\cdot}10^{-5}$	This study
Magnetite	10.5	175	0.03	$7{\cdot}10^{-6}$	This study
Enamel	3.5 – 4.5	65 – 75	0.01 – 0.02	$4{\cdot}10^{-5}$ – $6.8{\cdot}10^{-5}$	[33-35]
Aragonite (Abalone and Conch shells)	3 – 4	70 – 75	0.01	$6.3{\cdot}10^{-5}$	This study, [36, 37]
Guanoine	4.5	62	0.02	$5.8{\cdot}10^{-5}$	[38]
Zirconia	10 – 15	140 – 240	0.05 – 0.06	$1.2{\cdot}10^{-6}$ – $5.1{\cdot}10^{-6}$	[26, 39, 40]
SiC	20 – 30	410 – 480	0.05 – 0.12	$1.5{\cdot}10^{-7}$ – $3{\cdot}10^{-7}$	[40, 41]
B_4C	30	430 – 480	0.13	$1.6{\cdot}10^{-7}$	[40, 42]

Table 2.1 Materials property group of various biominerals and structural ceramics. Yield damage from a blunt contact is proportional to H^3/E^2; yield from a sharp contact mostly depends on H, while microcraking from a sharp abrasive depends on the index $K^4_{Ic}/H{\cdot}E^2$. K_{Ic} of the radular teeth is unknown, hence only the factor $1/H{\cdot}E^2$ is presented and used for comparison.

2.4 Conclusions

The results obtained from the investigations outlined above have the potential to enable progress in the emerging fields of nanotechnology and nanomanufacturing, exploiting control mechanisms established by nature to make novel materials and devices exhibiting unique properties. For example, the graded modulus design of the radular teeth and their anisotropic rod-like substructure provides design cues that could be used in the fabrication of ultrahard materials for precision cutting or wear-resistant components. The graded modulus design would be particularly useful for creating a self-sharpening condition in instances where location or situation would not permit regular replacement or sharpening of the cutting blades. In addition to understanding the structure function relationships in these unique abrasion- and impact-tolerant materials, the high abundance of crystalline magnetite also make them an ideal model system for elucidating the synthesis mechanisms of magnetic materials at ambient temperatures and pressures and near-neutral pH. Toward this endeavor, future investigation of the structure and composition of the tooth organic matrix could ultimately lead to the identification of specific chemical functionalities that play a critical role in controlling magnetite nucleation and growth.

2.5 Acknowledgements

We thank Philip Bruecker and Shane Anderson for help with specimen acquisition, Sara Krause for the illustration in Figure 1B, and Dr. Kenneth Evans-Lutterodt of the National Synchrotron Light Source for contributing his expertise at the microdiffraction endstation X13B. The NSLS is supported under USDOE Contract DE-AC02-98CH10886.

2.6 References

[1] H. N. Moseley, *Report of the scientific results of the voyage of H.M.S. Challenger during the years 1873-76: Zoology Part VII. Report on certain Hydroid, Alcyonarian, and Madreporarian Corals*, Neill and Company, Edinburgh, UK **1881**.

[2] F. E. Schulze, *Report of the scientific results of the voyage of H.M.S. Challenger during the years 1873-76: Zoology Part LIII. Report on the Hexactinellida*, Neill and Company, Edinburgh, UK **1887**.

[3] R. B. Watson, *Report of the scientific results of the voyage of H.M.S. Challenger during the years 1873-76: Zoology Part XLII. Report on the Scaphopoda and Gasteropoda*, Neill and Company, Ediburgh, UK **1886**.

[4] S. W. Heinz A. Lowenstam, *On biomineralization*, Oxford University Press, **1989**.

[5] K. M. Towe, Lowensta.Ha, *Journal of Ultrastructure Research* **1967**, *17*, 1.

[6] D. Vielzeuf, J. Garrabou, A. Baronnet, O. Grauby, C. Marschal, *American Mineralogist* **2008**, *93*, 1799.

[7] J. C. E. Ricketts, *Between Pacific Tides: Fifth Edition*, Stanford University, Stanford **1985**.

[8] D. P. A. R. H. Morris, E. C. Haderlie, *Intertidal Invertebrates of California*, Stanford Press, Stanford **1980**.

[9] R. Lydekker, *The Royal Natural History*, London Warne F. & Co., New York **1896**.

[10] S. Weiner, L. Addadi, *Science* **2002**, *298*, 375.

[11] D. J. Macey, L. R. Brooker, *Journal of Morphology* **1996**, *230*, 33.

[12] A. P. Lee, L. R. Brooker, D. J. Macey, J. Webb, W. van Bronswijk, *Journal of Biological Inorganic Chemistry* **2003**, *8*, 256.

[13] L. R. Brooker, A. P. Lee, D. J. Macey, W. van Bronswijk, J. Webb, *Marine Biology* **2003**, *142*, 447.

[14] F. Barthelat, H. D. Espinosa, *Experimental Mechanics* **2007**, *47*, 311.

[15] K. M. Towe, Lowensta.H.A., *Journal of Ultrastructure Research* **1967**, *17*, 1.

[16] T. H. Carefoot, *Proceedings of the Malacological Society of London*, London **1965**.

[17] K. Zaghib, C. M. Julien, *Journal of Power Sources* **2005**, *142*, 279.

[18] H. U. a. Y. Gremlich, B., *Infrared and Raman Spectroscopy of Biological Materials*, Marcel Dekker, New York **2001**.

[19] D. J. Macey, L. R. Brooker, J. Webb, T. G. StPierre, *Acta Zoologica* **1996**, *77*, 287.

[20] L. A. Evans, D. J. Macey, J. Webb, *Philosophical Transactions of the Royal Society of London Series B-Biological Sciences* **1990**, *329*, 87.

[21] M. F. Ashby, L. J. Gibson, U. Wegst, R. Olive, *Proceedings of the Royal Society of London Series a-Mathematical and Physical Sciences* **1995**, *450*, 123.

[22] P. van der Wal, H. J. Giesen, J. J. Videler, *Materials Science & Engineering C-Biomimetic and Supramolecular Systems* **2000**, *7*, 129.

[23] K. S. Chan, M. Y. He, J. W. Hutchinson, *Materials Science and Engineering a-Structural Materials Properties Microstructure and Processing* **1993**, *167*, 57.

[24] F. W. Zok, A. Miserez, *Acta Materialia* **2007**, *55*, 6365.

[25] G. Cardenas, G. Cabrera, E. Taboada, S. P. Miranda, *Journal of Applied Polymer Science* **2004**, *93*, 1876.

[26] E. Medvedovski, *Wear* **2001**, *249*, 821.

[27] C. A. Schuh, A. C. Lund, *Journal of Materials Research* **2004**, *19*, 2152.

[28] J. A. Williams, *Tribology International* **2005**, *38*, 786.

[29] S. M. Hsu, M. Shen, *Wear* **2004**, *256*, 867.

[30] S. J. Sharp, M. F. Ashby, N. A. Fleck, *Acta Metallurgica Et Materialia* **1993**, *41*, 685.

[31] A. Miserez, J. C. Weaver, P. J. Thurner, J. Aizenberg, Y. Dauphin, P. Fratzl, D. E. Morse, F. W. Zok, *Advanced Functional Materials* **2008**, *18*, 1241.

[32] S. Kamat, X. Su, R. Ballarini, A. H. Heuer, *Nature* **2000**, *405*, 1036.

[33] S. Habelitz, G. W. Marshall, M. Balooch, S. J. Marshall, *Journal of Biomechanics* **2002**, *35*, 995.

[34] A. P. Jackson, J. F. V. Vincent, R. M. Turner, *Proceedings of the Royal Society of London Series B-Biological Sciences* **1988**, *234*, 415.

[35] G. W. Marshall, M. Balooch, R. R. Gallagher, S. A. Gansky, S. J. Marshall, *Journal of Biomedical Materials Research* **2001**, *54*, 87.

[36] V. Imbeni, J. J. Kruzic, G. W. Marshall, S. J. Marshall, R. O. Ritchie, *Nature Materials* **2005**, *4*, 229.

[37] R. Menig, M. H. Meyers, M. A. Meyers, K. S. Vecchio, *Acta Materialia* **2000**, *48*, 2383.

[38] B. J. F. Bruet, J. H. Song, M. C. Boyce, C. Ortiz, *Nature Materials* **2008**, *7*, 748.

[39] J. D. Cawley, *The Encyclopedia of Materials Science and Technology (Buschow, K.H. et al.,)*, Pergamon, **2001**.

[40] R. E. Tressler, *The Encyclopedia of Materials Science and Technology (Buschow, K.H., et al.,)*, Pergamon, **2001**.

[41] M. Srinavassan, and Rafaneillo, W., *Carbide, Nitride and Boride Materials Synthesis and Processing (Weimler, A.)*, Springer, **1996**.

[42] G. Dewith, *Journal of Materials Science* **1984**, *19*, 457.

3 Chapter 3. Phase transformations and structural developments in the radular teeth of *Cryptochiton stelleri*

3.1 Introduction

Minerals have been used by organisms for at least 3500 million years. About 540 million years ago, there was a period that some organisms succeeded in constructing their skeletons with minerals. Today more than sixty different minerals (including amorphous minerals, inorganic crystals, and organic crystals) are widespread in all five kingdoms of organisms and the predominant ones on the earth consist of silica and calcium carbonate. Amorphous minerals, like calcium carbonate and phosphate, are usually used as temporary storage depots for ions essential for cellular metabolism. Other fairly common and somewhat unusual uses of amorphous minerals are fulfilling of skeleton functions or working as repository for embedding toxic metals. On the other hand, crystalline minerals are commonly used in gravity perception for mobile organisms. One exception to that is the navigation function of single crystals of iron oxides [1].

Among all the outstanding functions of these minerals serving in biological systems, the superior mechanical properties developed through diversification and specialization have obtained the most attention from materials scientists. Nano- and micro-scale hierarchically-designed structures of some biominerals have been revealed and related to their functions; layers of calcium carbonate with organic binder in the mollusks shells contribute to their high strength, toughness and impact resistance;

cylindrical rods of hydroxyapaptite with proteins and water make the rat tooth enamel hard and damage tolerant; silica in various shapes makes the diatoms hard and malleable [2]. Composite structural materials with outstanding hardness, abrasion resistance and impact tolerance are highly desirable for industrial and military-based applications. One way to obtain these composites is to learn from nature about how to control the synthesis of the nano- and micro-scale features of these biomaterials, as nature has built extraordinary systems through evolution for millions of years. Furthermore, nature has utilized room temperature and neutral pH-based synthesis strategies, which are low cost and environmental friendly [3].

One such example is found in the heavily mineralized and abrasion-resistant radular teeth of mollusks. Chitons and limpets are two specific groups that have attracted attention from scientists. Chitons, a group of elongated herbivorous mollusks, are protected dorsally by eight overlapping shell plates. The chitons graze for algae on hard substrates using a specialized rasping organ called the radula (Figure 3.1) [4-6], a conveyor belt-like structure located in the mouth (Figure 3.1A) that contains numerous parallel rows of mineralized teeth. Limpets are marine snails with a simple shell that is more or less conical in shape. They have a similar habitat and radular structure as chitons. Iron oxide minerals were found in the radula of both groups. During the feeding process, the first several rows of teeth at the anterior of the radula are involved in grazing and become worn. New teeth are continuously synthesized and enter the wear zone at the same rate at which teeth in the anterior-most row are shed from the growing ribbon [7, 8]. Approximately 0.40, 0.36 and 0.51 rows per day are produced for the chitons

Acanthopleura hirtosa and *Plaxiphora albida*, and for the limpet *Patelloida alticostata*, respectively.

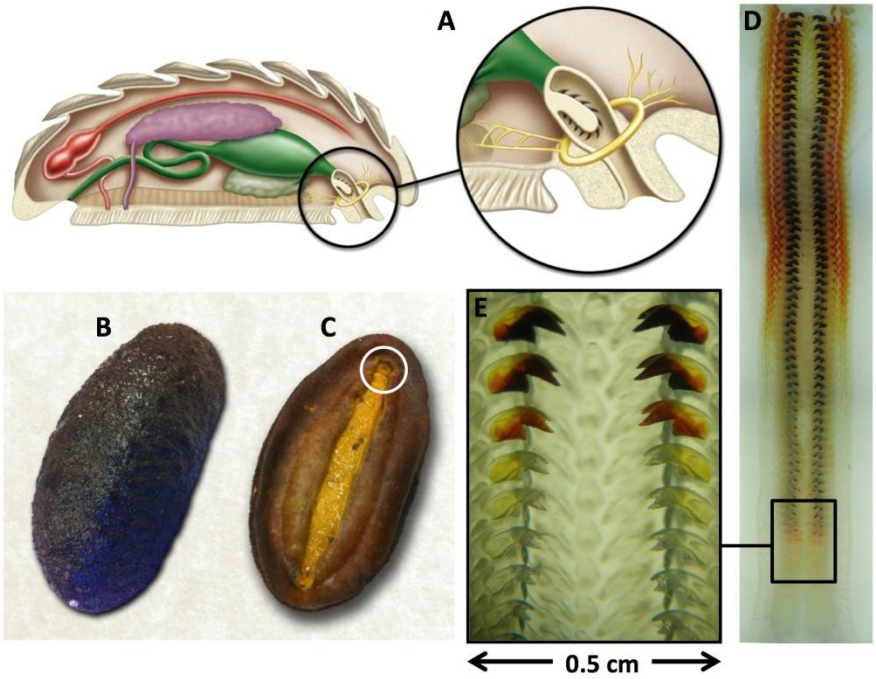

Figure 3.1 Chiton anatomy and gross morphological features of the radular teeth. (A) Diagrammatic lateral view of a representative chiton body plan, (B) dorsal and (C) ventral views of *Cryptochiton stelleri* (in this species, the characteristic overlapping shell plates shown in (A) are internal and thus not visible in the photo). The location of the mouth (which contains the radula) is circled in white. (D) Optical image of an entire radula from *C. stelleri*, containing more than 70 rows of parallel mineralized teeth. (E) Transitional zone near the posterior end of the radula demonstrating a gradual change in tooth color from transparent to black, representing the earliest stages of mineralization.

The new teeth of radula are initially made of organic matrix, and then mature gradually through mineralization to rasp for food and finally fall off the radula ribbon because of wear. The superior epithelium surrounding the teeth is responsible for delivering the elements required for mineralization and producing materials that harden

the radula. Dramatic ultrastructural changes of the apical cusp epithelium have been observed concurrently with the onset of the mineral in the teeth. Their cells die and the epithelium detach from the radula after the radula is hardened. A subradular membrane is secreted by the epithelium and serves to attach the epithelium to the radula. The membrane detaches from the radula after they undergo a change of the reversal of the tanning process [9, 10].

Ferritin is the major iron storage protein during the mineralization of the radula in limpets and chitons. Ferritin aggregates, usually found in the sidersome, contain considerable amounts of iron and are found in the superior epithelium just before the onsite of the mineralization in the tooth cusp. Some of these aggregates pass through the microvilli and deliver iron into the cusp of the tooth for the mineralization of the iron oxide [11, 12]. In *Acanthopleura hirtosa* and 18 other chiton species, ferritin was also found in the stylus canal, which appeared to be the other delivery pathway for the elements required for mineralization for the tooth cusp [13].

Mature radular teeth usually consist a hard shell / soft-core structure. For limpets, the mineral in the outer shell is goethite, while the core is siliceous [11, 14-22]. For chitons, the mineral contents vary in different species. In *Acanthopleura hirtosa,* the outer shell consists of magnetite, while the core is made of calcium apatite; lepidocrocite and goethite are found as a thin layer between the core and shell [12, 13, 23-28]. A magnetite-containing shell and an iron (III) phosphate core in *Plaxiphora albida* was claimed by Macey et al. in 1995 [26]. However, seven years later (2002) Lee et al.

analyzed the mature tooth with Raman microscopy and found that a narrow band of a hydrated iron (III) oxide (limonite) was shown to separate the magnetite of the tooth surface from a lepidocrocite and limonite containing central core region, without a separate iron phosphate mineral present [29]. They argued that the high concentration of phosphorus observed by energy dispersive spectroscopy in the core region of *P. albida* tooth may have come from the adsorption of phosphorous onto the surface of the iron oxides. XRD analysis through three species, *Acanthopleura echinata, Acanthopleura echinatum, and Chiton tuberculatus*, revealed a magnetite shell / apatite core, separated by a thin lepidocrocite layer structure [30]. A veneer of ferrihydrite on the surface of the mature tooth of *Acanthopleura echinata* was detected with Raman microscopy [31]. In *Liolophura loochooana*, the anterior side is formed with lepidocrocite, while the posterior side consists of magnetite [32]. Transformation of amorphous calcium phosphate to crystalline dahllite in the radular teeth of *Acanthopleura haddoni* was detected [33]. EDS analysis of radular teeth from *Cryptoplax striata* revealed that the mineralization starts with iron infiltration, followed by phosphorus and then calcium [34].

The Gumboot Chiton, *Cryptochiton stelleri*, a common inhabitant of the rocky shores of the temperate Northeastern Pacific, is the world's largest species of chiton, reaching a maximum length of more than 30 cm (Figure 3.1B, C) [35-37]. The radula of *C. stelleri* contains more than 70 rows of mineralized and curved tricuspid teeth (Figure 3.1D). The fully mineralized radular teeth consist of an iron phosphate / magnetite core-shell structure that displays remarkable mechanical properties including the highest reported hardness and modulus of any known biomineral [38]. The organic matrix of

these teeth consists primarily of α-chitin (a polymer of β-1, 4 linked N-acetylglucosamine units) and provides a three-dimensional structural framework onto which the mineral phases are precipitated. The resulting mature teeth exhibit a decreasing hardness and modulus from the leading to trailing tooth edges and due to asymmetrical wear patterns, creates a self-sharpening condition. This design affords the teeth the ability to withstand abrasion, impact, and fatigue during substrate rasping events, similar to conditions experienced by industrial machinery such as tunnel boring, oil drilling, shaping and machining tools [8].

Thus, the biomineralization process is paramount in driving the formation of the complex architecture of the radular teeth, which results in their distinct, region specific mechanical properties. Since every stage of tooth development is contained within a single radula (Figure 3.1E), it thus provides an ideal model system for investigating the dynamic processes of biomineralization during tooth growth and maturation [9, 12, 23].

The radular teeth of *C. stelleri* were first studied by Towe and Lowenstam in the 1960s, who identified the presence of ferritin, in both crystalline and paracrystalline phases, as a likely shuttling vehicle for iron during tooth mineralization [39]. Lowenstam further showed that an open framework organic matrix was present in non-mineralized teeth and likely acted as a template for mineral deposition *[40]*. In 1979, Kirschvink and Lowenstam confirmed that during the earliest stages of mineralization in the outer margins of the teeth of *C. stelleri*, ferrihydrite was first precipitated and was later transformed to magnetite *[41]*. In these early studies, however, the magnetite mineral

phase was assumed to be approximately homogeneous throughout the shell region and nothing was known regarding the gradient in mechanical properties from the leading to trailing edge of the teeth, which was only recently described [3]. In light of these new observations, and to help clarify how the dynamics of tooth mineralization can influence the local mechanical properties, we report here an interdisciplinary study into the sequential stages of radular tooth mineralization in *C. stelleri* using synchrotron X-ray diffraction (XRD), synchrotron micro-X-ray fluorescence (μ-XRF), transmission electron microscopy (TEM) and scanning electron microscopy (SEM).

3.2 Materials and experiments

3.2.1 Research Specimens

Live specimens of *Cryptochiton stelleri* were collected from the temperate Eastern Pacific Ocean (Monterey, CA) and maintained in recirculating seawater system at 15 °C before use. Collection of *Cryptochiton stelleri* is permitted by the Department of Fish and Game and the California Natural Resources Agency. The radulae were dissected from these specimens and rinsed in fresh seawater to remove any loose organic debris.

3.2.2 Energy Dispersive Spectroscopy

For elemental mapping via EDS, 20 rows of immature teeth, centered on the site of initial mineral deposition and still attached to the basal ribbon, were cut from an intact radula with a razor blade and then serially dehydrated to 100% ethanol. The tooth rows were then critically point dried with CO_2 to avoid damage or shrinkage of organic structures, mounted to conductive carbon tape and examined with a Tescan VEGA TS-

5130MM SEM equipped with an IXRF systems energy dispersive spectrometer. EDS mapping was performed at an accelerator voltage of 20keV.

3.2.3 Synchrotron X-ray Diffraction

24 partially mineralized radular teeth (removed from the posterior end of the radula), still attached to the basal ribbon, were cut from an intact radula with a razorblade and then serially dehydrated to 100% ethanol. The isolated teeth were then critical point dried with CO_2 and attached to a silicon wafer using conductive carbon tape. The radular teeth were transversely analyzed at beamline X6B of the National Synchrotron Light Source (NSLS) in Brookhaven National Laboratory using 19 keV X-rays and a beam spot focused to 100 x 100 μm. X-ray transmission mapping was performed on the entire sample using 1 second scans with a 50 μm step size to investigate the progressive change in electron density along the length of the radula. X-ray diffraction mapping was performed on the entire sample using a 100 second diffraction time with a 100 μm step size to reveal the crystalline phases present in the teeth. X-ray diffraction of reference standards, including α-chitin, magnetite, goethite, lepidocrocite and alumina were also performed using the same beamline settings. The synchrotron X-ray diffraction data collected were imported into Datasqueeze 2.2.4 and initially calibrated with an Al_2O_3 powder standard and using the magnetite from the fully mineralized teeth as an internal reference. Intensity vs. Q ($Q=2\pi/d$) plots were integrated from the diffraction patterns and used for mineral phase analysis. Intensity vs. 2θ plots were generated and selected reflections were fitted with polynomial and Lorentzian parameters to calculate the relative concentrations of the specific mineral phases.

3.2.4 Synchrotron Micro X-ray Fluorescence

Four partially mineralized teeth (#1, #2, #3 and #4, all still attached to the basal ribbon) were cut from an intact radula with a razor blade and fixed with gluteraldehyde (2.5%) in phosphate buffer for 2 hours, followed by an overnight post fixation with OsO_4 (1%) at 4 ºC. The sample was then serially dehydrated to 100% ethanol, embedded in Spurrs resin and cured for 24 hours at 60 °C. The obtained resin block was sectioned with a diamond saw and polished in the longitudinal direction with silicon carbide grit paper to P1200, followed by polishing with diamond lapping films down to 0.25 μm. The result was a thin, finely polished specimen containing longitudinal cross sections of 4 partially mineralized teeth. μXRF imaging was performed on the polished sample at beamline 2-3 of the Stanford Synchrotron Radiation Lightsource (SSRL) using a Si (111) monochrometer detuned 20% at 7 keV and calibrated using Fe metal foil at 7112 eV. The sample was rastered across a 2.5 x 2.5 μm micro-focused X-ray beam and positioned at a 45° angle to the incident beam, with a 5 μm pixel step size and 125 ms dwell time per pixel. Multiple energy (ME) mapping was conducted near the Fe K-edge by rastering each line of the map at five discrete energies (7115, 7122, 7125, 7130 and 7140 eV) using a single element Vortex silicon drift detector (SII Nano Technology USA Inc.) situated perpendicular to the incident beam. These energies were selected based on XANES spectra of previously-collected model Fe compounds and chosen at points intended to maximize differences between ferrihydrite and magnetite [42]. Principal component analysis (PCA) was conducted on the multiple energy Fe maps using the MicroAnalysis Toolkit (SMAK), yielding principal component maps which showed the

spatial distribution of the dominant mineral phases which comprised the sample. These maps were in turn used to identify several (2-5) discrete points per radular tooth for micro X-ray absorption near edge structure (μXANES) analysis. All μXANES spectra were collected from 6880 eV to 7530 eV and then dwell time corrected, background-subtracted, and normalized for the incident X-ray beam intensity using the SIXPACK software package [43].

3.2.5 Transmission Electron Microscopy

To investigate the early stages of magnetite mineralization, tooth #4 was cut from an intact radula with a razor blade and then fixed with gluteraldehyde (2.5%) in HEPES buffer (0.2M, pH7.2) for 2 hours, followed by an overnight post-fixation with OsO_4 (1%) at 4°C. The sample was then serially dehydrated to 100% ethanol, embedded in Spurrs resin and cured for 24 hours at 60 °C in a microtome sample holder. 80 nm thick sections from several regions were microtomed from the resin block with a glass knife and imaged with a Tecnai T12 Transmission Electron Microscope at 120 kV.

3.2.6 Scanning Electron Microscopy

For fracture surface analyses, a single tooth still attached to the basal ribbon was cut from an intact radula with a razor blade and then serially dehydrated to 100% ethanol. The tooth rows were then critical point dried with CO_2, mounted on an aluminum pin mount with conductive carbon tape. Silver paste was applied between the base of the tooth and the carbon tape to dissipate charge build-up from the SEM. Fracture surfaces of

these teeth were created via impact with a razor blade. The samples were gold coated and then imaged with an XL30-FEG Scanning Electron Microscope at 10 kV.

3.2.7 Statistical Analysis

The calculation of particle size, fiber spacing and rod diameter were performed manually by measuring their dimensions directly from SEM or TEM micrographs. Approximately 50 measurements were acquired from each image and the means and standard deviations were determined. The particle densities in TEM images were obtained by dividing the total number of the particles by the area of the corresponding image.

3.2.8 Biomimetic synthesis of ferrihydrite within nonmineralized teeth

To investigate the capability of the nonmineralized teeth at different stages to template ferrihydrite nucleation, ferrihydrite nucleation studies were carried out within the nonmineralized teeth. 9 nonmineralized teeth were dissected from a hydrated radula, washed with DI water, and then immersed in 10^{-4} M Fe $(NO_3)_3 \cdot 9H_2O$ aqueous solution with stirring. The solution was hydrolyzed for 12 min at 75 °C, followed by 24 hours at room temperature. After that, the radular teeth were taken out of the solution, washed with DI water, and serially dehydrated to 100% ethanol then air dried. Characterization was performed by SEM and EDS.

3.2.9 Biomimetic synthesis of ferrihydrite on AAO templates

In order to verify the heterogeneous nucleation of ferrihydrite on the organic matrix, biomimetic syntheses of ferrihydrite were performed on bare and surface-modified Anodic Aluminum Oxide (AAO) membranes by nucleating ferrihydrite within these pore channels. This was achieved by immersing these membranes within aqueous 10^{-2} M $Fe(NO_3)_3 \cdot 9H_2O$ solution at 25°C (with the pH adjusted to 7) for 3 days. The AAO membranes (60 μm thick discs with pores of 200 nm in diameter) were purchased from Whatman. The surface-modified AAO membranes were prepared by gold coating using an E-beam evaporator with subsequent immersion for 24 hours in 10 mM ethanol-based alkanethiol solutions, including 1-Undecanethiol ($-CH_3$), and 11-Mercapto-1-undecanol (-OH). After the surface modification, coated membranes were immersed in the same ferric nitrate solutions as described above. After the 3 day reactions, membranes were removed from the ferric nitrate solutions, rinsed with DI water and air dried. Characterization was performed by SEM and EDS.

3.3 Results

3.3.1 Ultrastructure of the Mature Radular Tooth

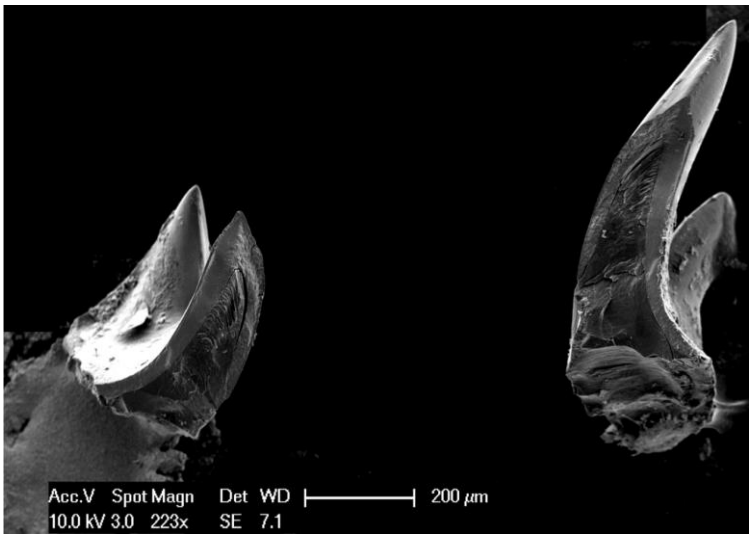

Figure 3.2 A mature tooth of *C. stelleri* was fractured longitudinally. Both sides of the fracture pieces were analyzed with SEM and the shell-core structure was revealed.

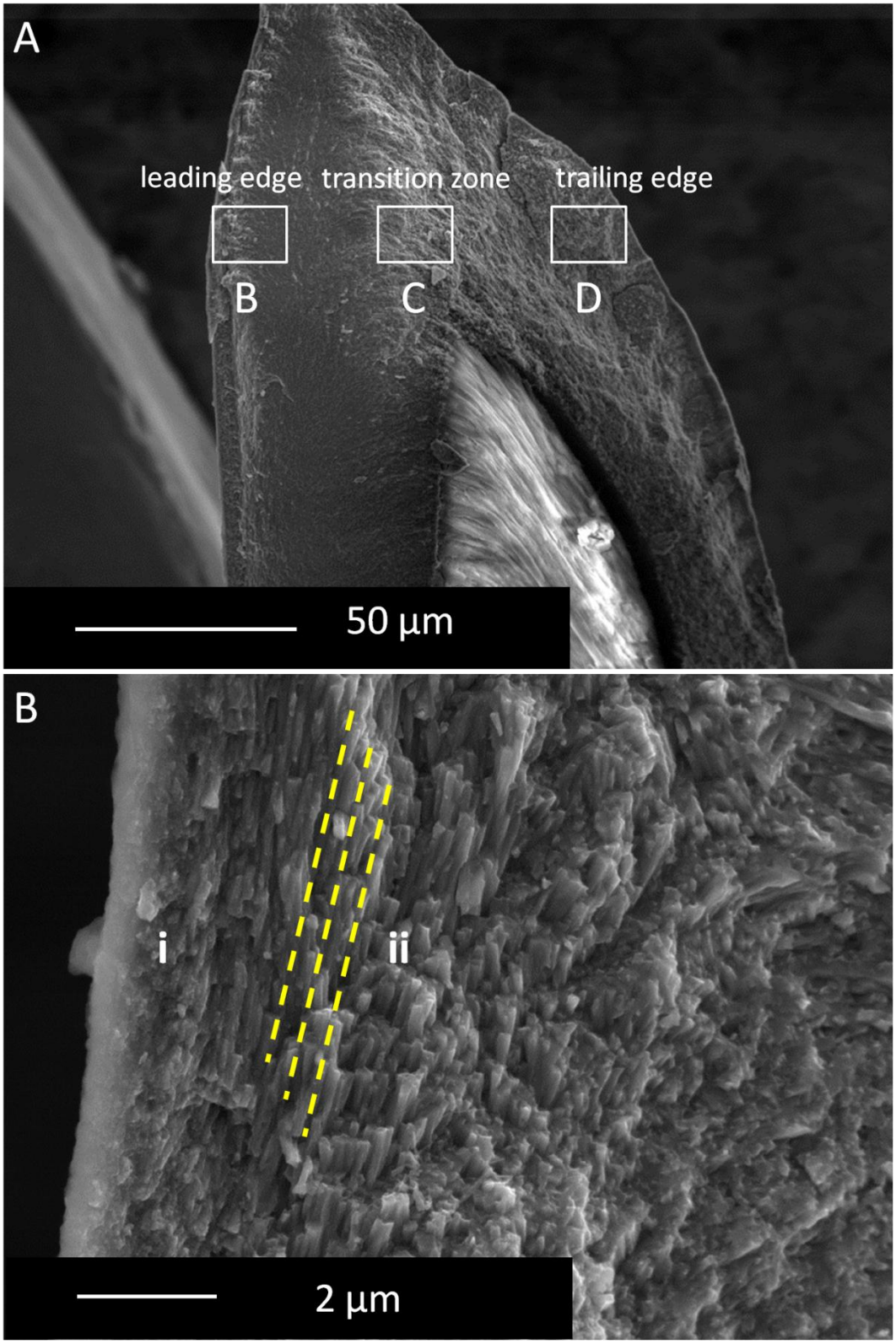
A
leading edge
transition zone
trailing edge
B
C
D
50 µm
B
i
ii
2 µm

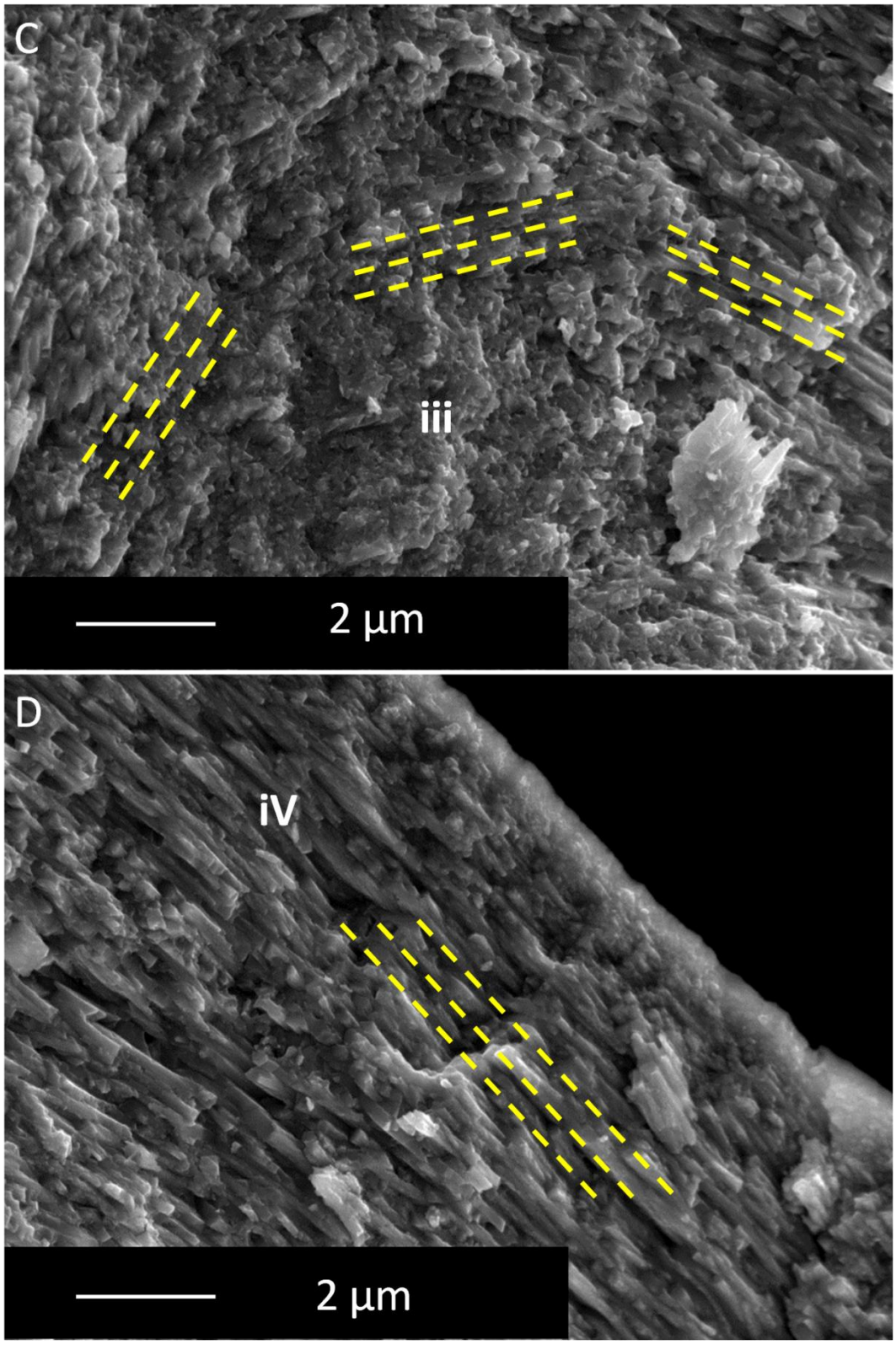
C
iii
2 µm
D
iV
2 µm

Figure 3.3 SEM analysis reveals the magnetite structural diversity at the apex of a fully mineralized radular tooth from *C. stelleri*. (A) The longitudinal fracture surface of a mature radular tooth uncovers the loose iron phosphate core (lighter) and the solid magnetite shell region (darker). Regional structural heterogeneity includes (i) the granular magnetite veneer, the magnetite rods oriented parallel to the leading (ii) and trailing (iv) tooth edges and a gradual bending at transitional zone between them (iii). The yellow dashed lines represent the prevalent orientation of the rods in regions (ii), (iii) and (iv).

A radular tooth from the mature zone was separated and fractured into 2 parts longitudinally. Both of the fracture pieces, with fracture surfaces facing upwards, were put on carbon tape onto a SEM stub for analysis (Figure 3.2). SEM analysis of the fracture surface (Figure 3.3) reveals a regionally segregated composite core-shell structure. Outside of the iron phosphate core region of the tooth is the shell region, consisting of either magnetite particles or rods, whose longitudinal axes are oriented relative to the tooth's surface curvature. From the leading edge of the tooth to the trailing edge, there are four distinct morphological transitions in the magnetite phase (Figure 3.3): *(i)* surrounding the entire periphery of each tooth is a very thin zone of condensed magnetite nanoparticles, which is thickened to a width of up to 2 μm at the outermost surface of the leading edge, *(ii)* beneath this thin granular veneer are bundles of magnetite rods oriented parallel to the leading edge of the tooth, *(iii)* these rods undergo a gradual bending around the iron phosphate core until, *(iv)* their orientation becomes once again parallel with the trailing edge of the tooth. SEM measurements of the magnetite rods from these specific regions reveal an increase in rod diameter from the leading edge (162

± 22 nm) to the trailing edge (194 ± 30 nm) of the tooth which is correlated with a significant decrease in hardness and modulus throughout the same region [3].

3.3.2 Phase Transformations

Progressive mineralization in the immature teeth was revealed though synchrotron X-ray transmission mapping, EDS mapping, and BS-SEM. A sequential decrease in X-ray transmittance through a set of 24 immature radular teeth (still attached to the basal membrane via their nonmineralized stalk) of *C. stelleri* suggests a gradual increase of mineral content (Figure 3.4A), an observation further supported by BS-SEM and EDS analysis (Figure 3.4B-E) with mineralization first occurring in the leading edges of the teeth.

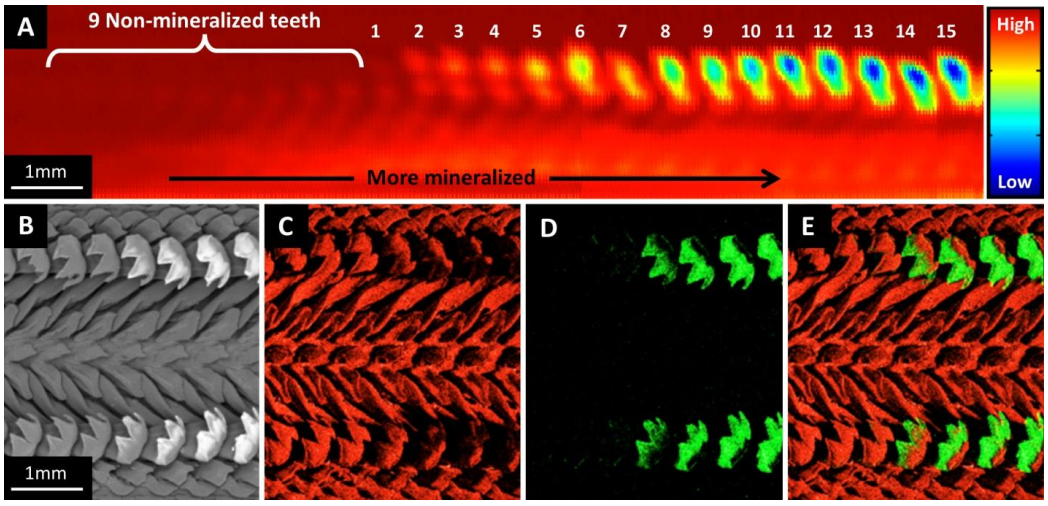

Figure 3.4 Early stages of radular tooth mineralization. (A) Synchrotron X-ray transmission map (lateral view) of 24 partially mineralized radular teeth (still attached to the basal ribbon) reveals a gradual increase in electron density from the posterior to the anterior regions, corresponding to an increase in the extent of mineralization. (B) Dorsal view back-scattered scanning electron microscopy (BS-SEM) and energy dispersive spectroscopy (EDS) highlighting (C) carbon, (D) iron, and (E) carbon-iron distribution during the transition from the nonmineralized to partially mineralized state.

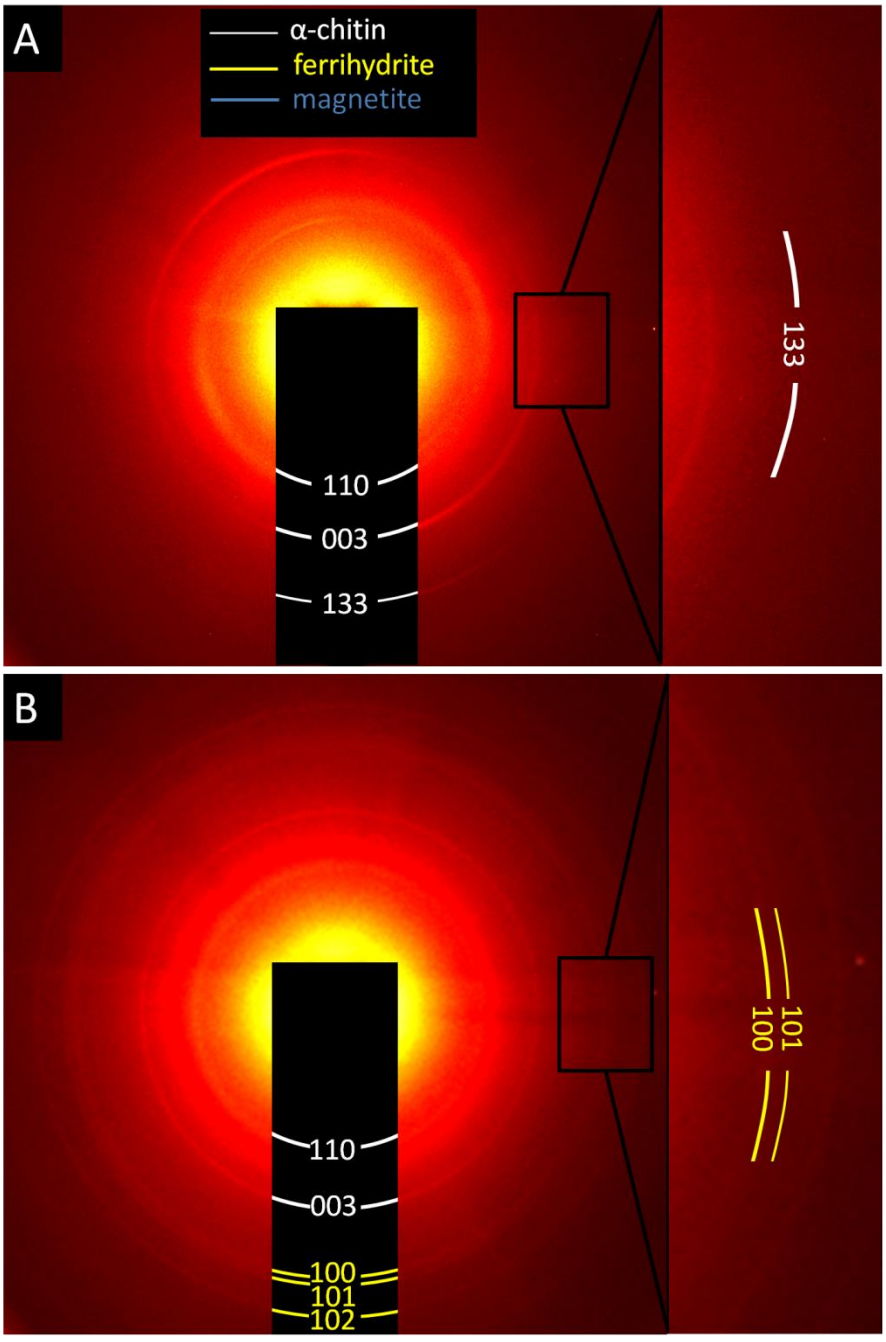
A
α-chitin
ferrihydrite
magnetite
133
110
003
133
B
101
100
110
003
100
101
102

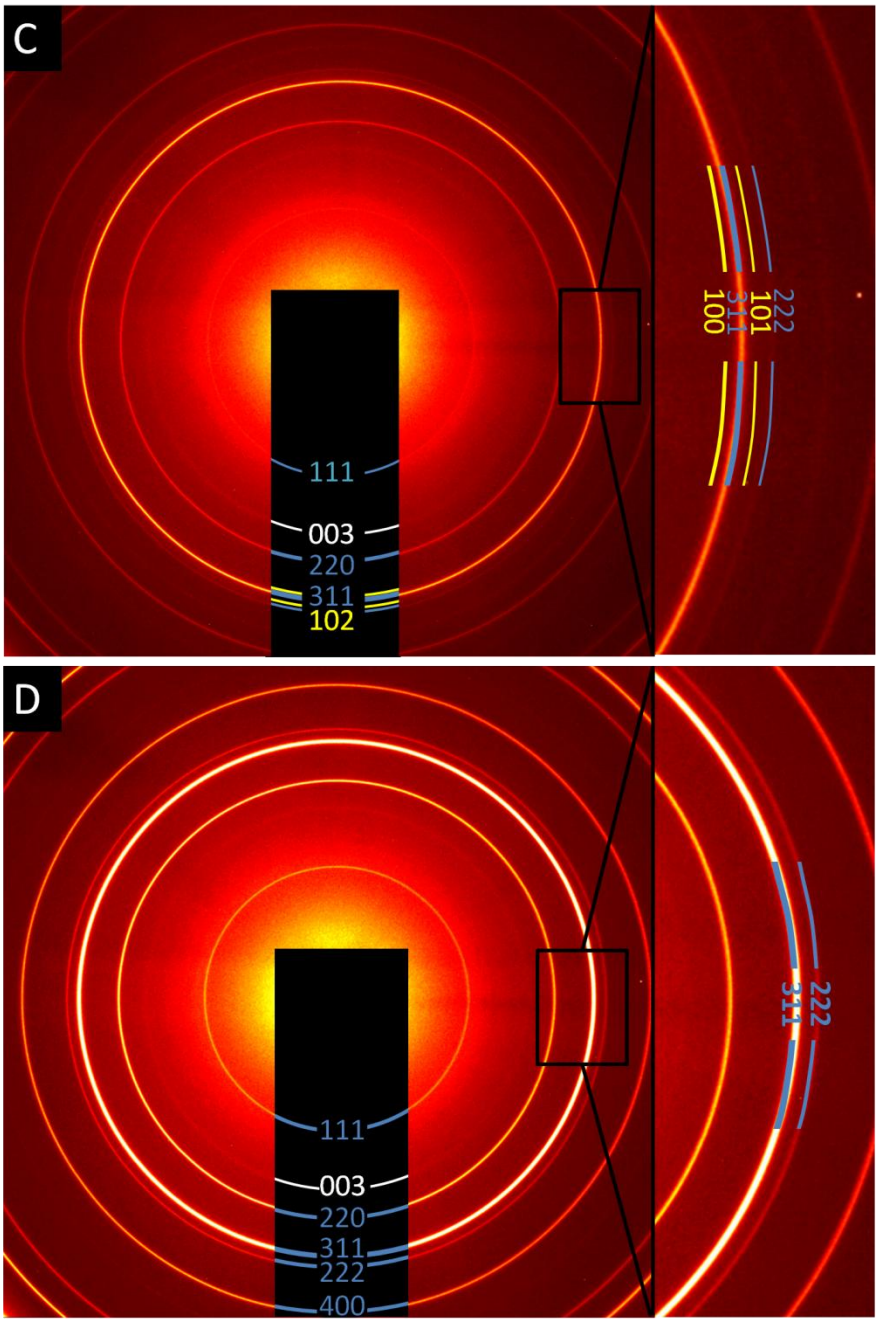

Figure 3.5 Representative synchrotron X-ray diffraction frames from (A) nonmineralized teeth, (B) tooth #1, (C) tooth #3, and (D) tooth #5 snapshots the transformation from ferrihydrite to magnetite during the early stages of radular tooth mineralization. Peaks indexed from these patterns are confirmed by reference to the azimuthally integrated patterns shown in Figure 5A and in some cases, arcs in this figure are primarily guides for the eye. Miller indices of each phase are labeled on the frames based on the analysis

from Figure 3.6. White, yellow and blue arches correspond to α-chitin, ferrihydrite and magnetite, respectively.

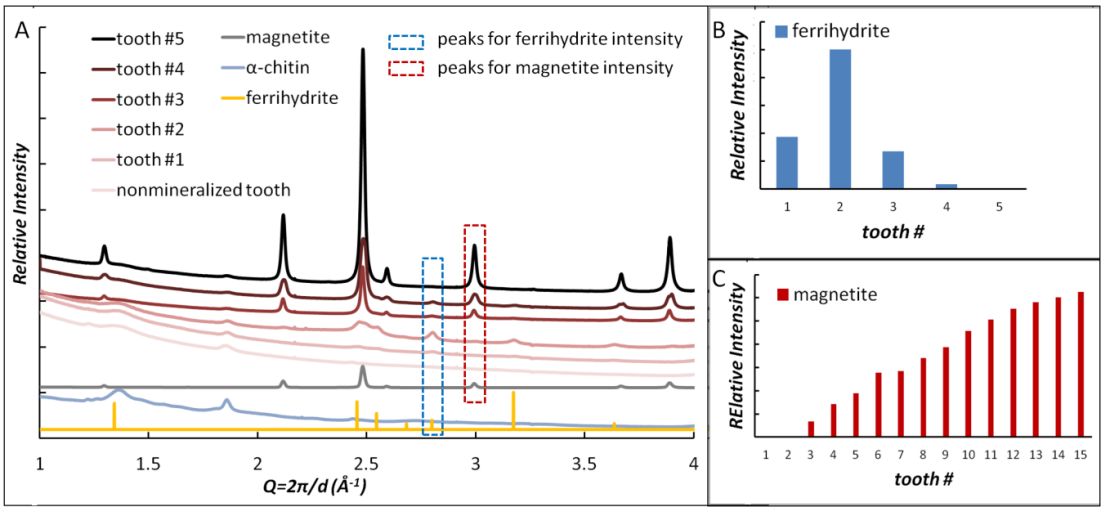

Figure 3.6 Qualitative phase transformations during early radular tooth mineralization. (A) Intensity vs. Q (Q=2π/d) plots extracted from representative synchrotron X-ray diffraction patterns of a nonmineralized tooth and teeth #1,#2, #3 and #5 compared to diffraction standards. Q=2.802 $Å^{-1}$ (specific to ferrihydrite) and Q=2.991 $Å^{-1}$ (specific to magnetite) reflections were used to investigate the change in (B) ferrihydrite and (C) magnetite concentrations during tooth maturation.

For all subsequent analyses discussed in this report, the teeth will be numbered sequentially referenced from the earliest visible signs of mineral deposition (which we call "Tooth #1"). This tooth is easily identifiable with optical microscopy as the first tooth to change from transparent to yellow (the third tooth from bottom in Figure 1E), and via EDS, is the first tooth to contain detectable levels of iron.

To study the phase transformation in the radular teeth at this early stage of development, synchrotron X-ray diffraction mapping in transmission geometry with a

100μm-step size (and a 100μm-spot size) was performed along the entire radula, with comparison measurements made against magnetite, α-chitin, and ferrihydrite reference standards. Four representative diffraction frames (Figure 3.5) from (A) nonmineralized teeth, (B) tooth #1, (C) tooth #3 and (D) tooth #5 provide snapshots of the early stages of the mineralization process. Integrated XRD patterns plotted as Intensity vs. Q ($Q=2\pi/d$) from these frames allow us to discern the presence of multiple mineral phases within each tooth (Figure 3.6A). Based on the comparison of representative plots from radular teeth and mineral standards (Table 3.1), α-chitin is the only crystalline phase detected in the nonmineralized teeth and persists throughout all of the examined teeth. Six-line ferrihydrite appears in tooth #1 and persists until tooth #5. Magnetite is first detected in tooth #2 and is observed in all subsequent teeth. The only mineral detected in tooth #5 is magnetite, which indicates the end point of the large scale iron oxide phase transformation. Miller indices corresponding to each crystalline phase are included on the representative synchrotron X-ray diffractograms (Figure 3.5) *[44-46]*.

α-chitin (standard)	ferrihydrite [a]	magnetite (standard)	nonmineralized tooth	tooth #1	tooth #3	tooth #5
1.216						
1.256			1.220	1.231	1.231	1.231
		1.297			1.297	1.297
	1.341			1.347	1.347	

1.360			1.364			
1.854			1.858	1.858	1.858	1.858
		2.115			2.115	2.115
2.434			2.449			
	2.455			2.461	2.465	
		2.479			2.492	2.479
	2.545			2.551	2.546	
		2.591			2.591	2.591
	2.682			2.690	2.667	
	2.798			2.802	2.802	
		2.991			2.991	2.991
	3.173			3.175	3.175	
	3.636			3.634	3.634	
		3.665			3.665	3.665
		3.890			3.890	3.890

Table 3.1 Q (Å-1) values derived from diffraction peaks in Figure 3.6A.

[a] E. Jansen, A. Kyek, W. Schafer, U. Schwertmann, *Applied Physics a-Materials Science & Processing* **2002**, *74*, S1004.

There is a difference in Q values, about 0.002 ~ 0.006 (Å-1), between the ferrihydrite reference and the ferrihydrite phase that were detected from the synchrotron X-ray diffraction. This discrepancy may come from the calculation error of the standards in synchrotron X-ray diffraction. The assumption during calculation that the distance between the sample and the detector is the same as that between the aluminum standard and the detector results in the small shift in the Q values as there is about 50 ~ 100 μm difference in thickness between the tooth sample and the alumina standard.

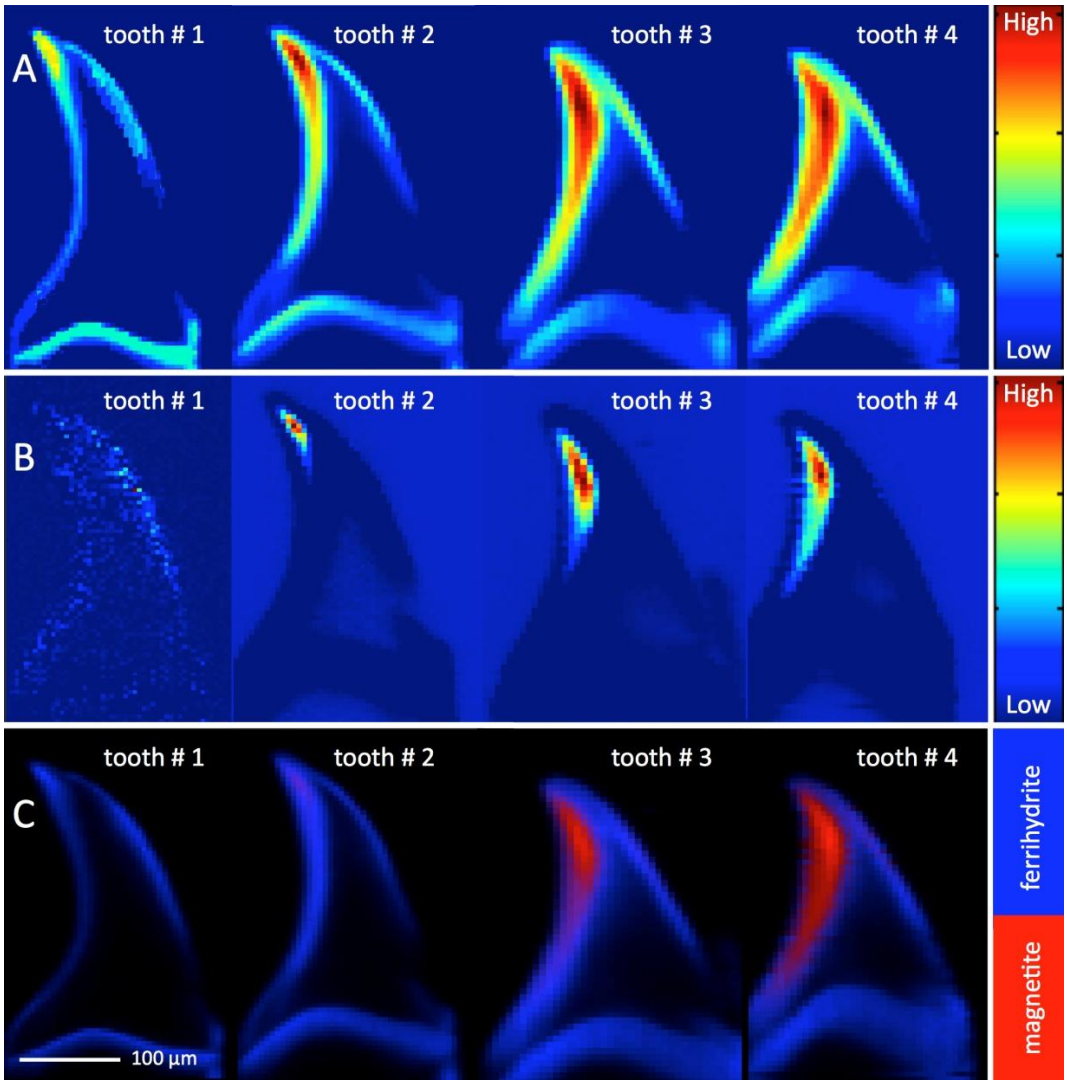

Figure 3.7 Micro X-ray Fluorescence (μXRF) analysis of longitudinal thin sections of radular teeth #1-4 reveals the local iron oxide transformation in *C. stelleri*. Both the

intensity of (A) total iron and (B) ferrous iron increase across the leading edge with increasing tooth maturation. (C) Micro X-ray Absorption Near Edge Structure (μXANES) analysis reveals an increasing abundance of magnetite across the shell region along the leading edge of radular teeth.

To investigate the compositional change of ferrihydrite to magnetite with increasing tooth maturation, the Q=2.802 $Å^{-1}$ (specific to ferrihydrite) and Q=2.991 $Å^{-1}$ (specific to magnetite) reflections were analyzed separately. Polynomial and Lorentzian functions were applied to fit the Intensity vs. Q plots for the selected reflections. The area under each curve was obtained and used as a metric to quantify the corresponding mineral phases. The compiled results (shown in Figures 3.6B and C) were averaged from the integrated peak areas from the 10 point locations on each tooth that corresponded to the highest x-ray absorbance. From these measurements, it was determined that ferrihydrite concentration reaches a maximum in tooth #2, decreasing to about 1/3 of the maximum concentration in tooth #3, and disappearing entirely by tooth #5 (Figure 3.6B). In contrast, magnetite peak intensity, which first appears in tooth #2, increases steadily for the next 20+ teeth (Figure 3.6C) until finally reaching a stable maximum throughout the remaining radular teeth.

In order to more accurately spatially resolve the phases transformations in the radular teeth of *C. stelleri* observed with synchrotron XRD, synchrotron μXRF (Figure 3.7) was performed on radular teeth #1-4 using a 2.5 x 2.5 μm beam spot size (1600 times smaller than that used for the XRD analysis). Principal component analysis (PCA) was then applied to the multiple Fe μXRF maps, resulting in two principal component

maps which were correlated with the concentrations of total iron (Figure 3.7A) and ferrous iron (Figure 3.7B) in each tooth. The resulting PCA maps indicated that the concentrations of both total iron and ferrous iron increase with tooth maturity. Furthermore, from a comparison of the PCA maps, the presence of ferric iron can be inferred wherever total iron is present and ferrous iron is absent. Accordingly, ferric iron appears to be prevalent across all teeth surfaces, including the interface between each tooth and its base, while ferrous iron first appears at the tip of tooth #2 and then propagates along the leading edge with increasing tooth maturation.

Based on synchrotron XRD analyses, the ferrous and ferric iron identified by μXRF/PCA can be assigned to magnetite and ferrihydrite, respectively. To more clearly distinguish between the two species, several (2-5) discrete points per radular tooth were selected using the PCA maps for Micro X-ray Absorption Near Edge Structure (μXANES) analysis [42]. From the resulting μXANES spectra, the two spectra exhibiting the greatest differences in the Fe K-edge position (a proxy for oxidation state) were selected as end members to represent the most ferric and ferrous locations among all four teeth. The Fe K-edge Multiple Energy (ME) μXRF maps were then fitted in a non-negative linear least-squares format using normalized fluorescence values obtained from the two end member μXANES corresponding to the 5 different map energies, similar to the method applied by Mayhew et al [47]. The resulting manually scaled two-color map shows the increasing abundance of a ferric (ferrihydrite) phase across the surface of the radular teeth and the evolution of a more ferrous (magnetite) phase along the leading edge (Figure 3.7C), consistent with the results of the PCA analysis. Based on the synchrotron μXRF analysis,

both the ferrihydrite deposition and the phase transformation to magnetite initiate at the tip of the leading edge of the tooth.

3.3.3 Structural Development

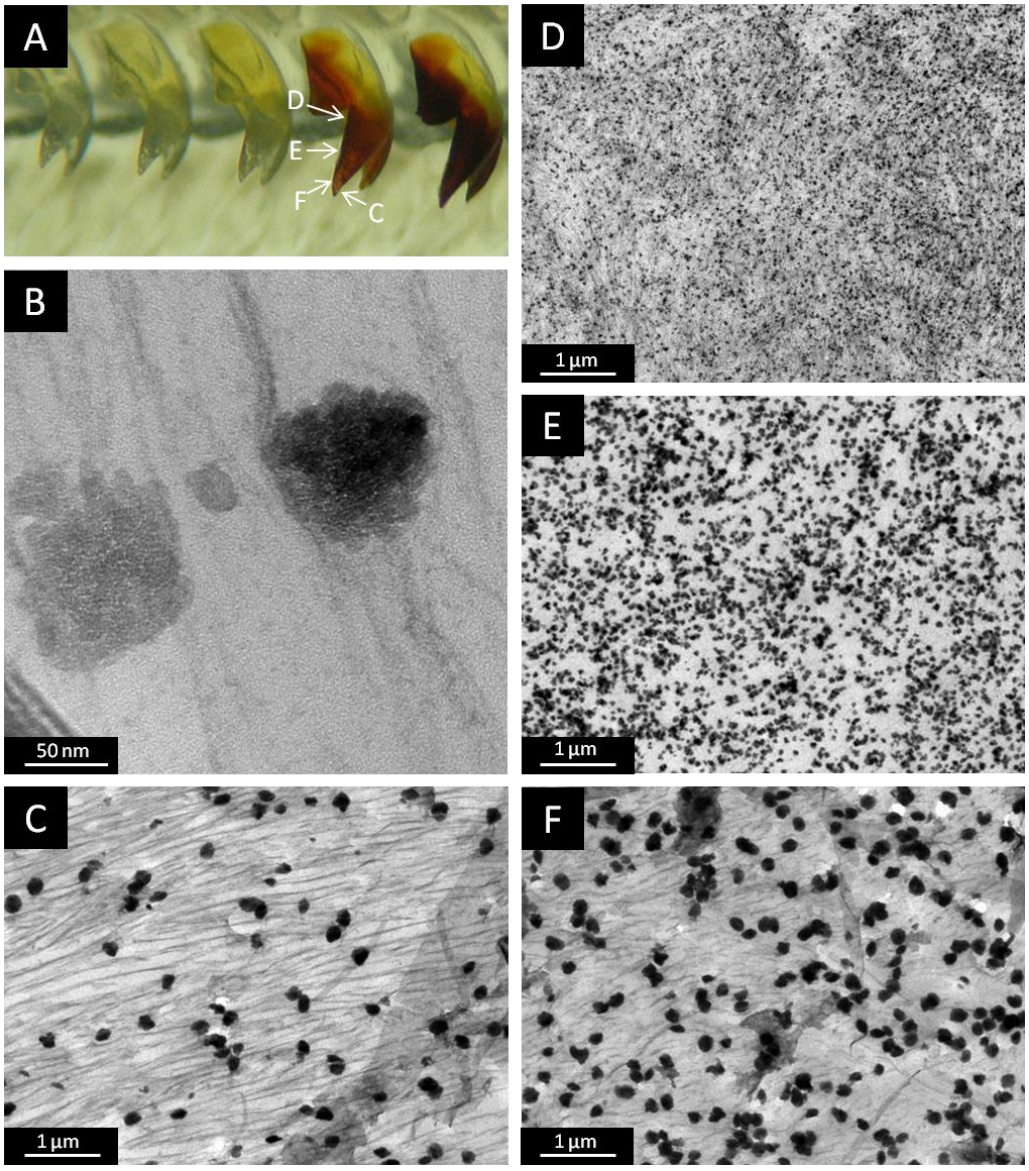

Figure 3.8 Transmission Electron Microscopy (TEM) analyses of regional differences in magnetite nucleation density and aggregation during early radular tooth mineralization (tooth #4). (A) An optical micrograph shows the locations of TEM sections. Magnetite deposition is spatially confined by the fibrillar organic matrix and consists of aggregated

nanocrystallites measuring 10-15nm in diameter (B). From the bottom to the tip of the leading edge of the tooth (D, E and F), there is a progressive decrease in particle density and a corresponding increase in particle size of mineral. Bigger spacing of organic matrix at the trailing edge results in lower particle density of mineral (C).

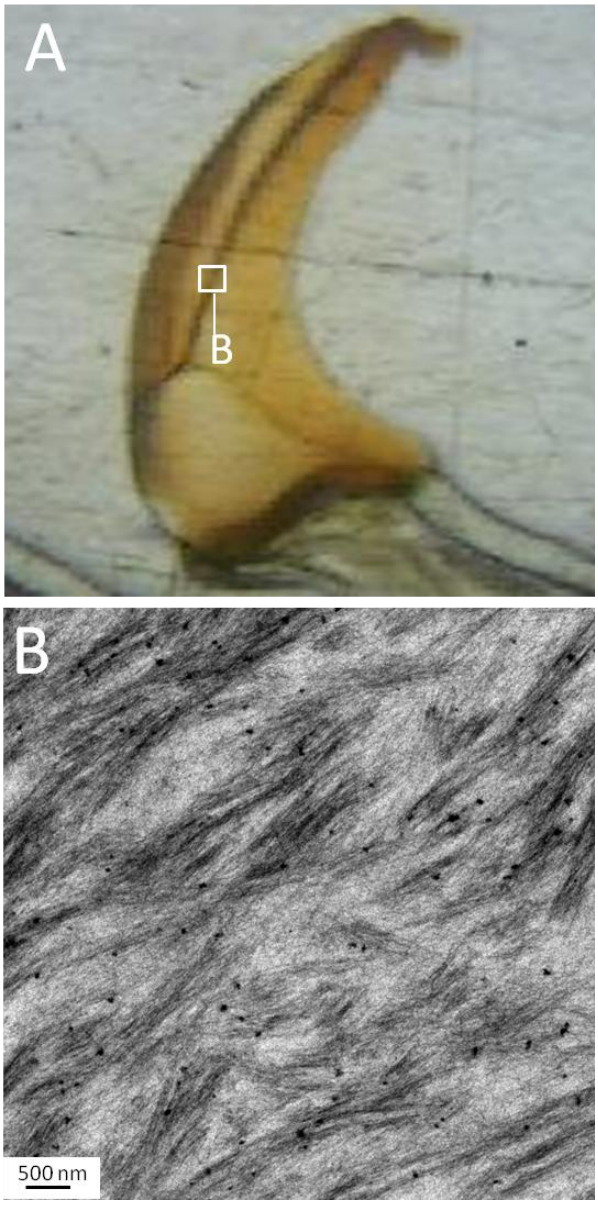

Figure 3.9 The core region of the tooth #4 consists of loose bundles of organic fibers with rare mineral particles attached.

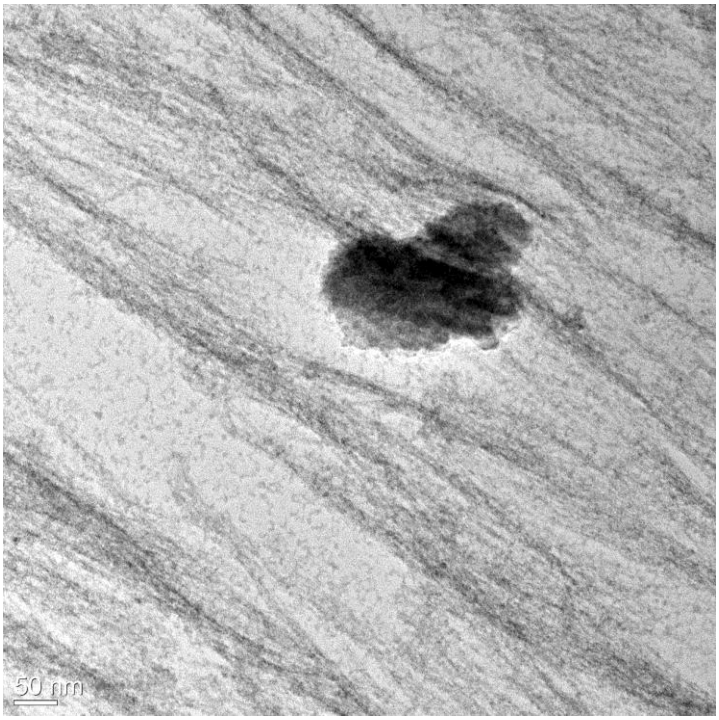

Figure 3.10 Mineral particles aggregate at the two sides of the same site of an organic fiber.

The magnetite rod formation process, including the organic matrix-mediated mineral aggregation and growth, was investigated using TEM and SEM. TEM analyses of the proximal, medial, and distal regions of the leading edge and the distal region of the trailing edge from longitudinal sections of tooth #4 (Figure 3.8A) were investigated to look for any regional differences in mineral deposition during tooth formation. Mineral particles were observed on the organic fibers in all four regions analyzed and were deposited along the fibrous organic matrix. A representative high resolution TEM micrograph from the tip of the trailing edge reveals that each magnetite aggregate consists of 10 - 15nm crystallites that appear to have nucleated on the organic fibers (Figure 3.8B).

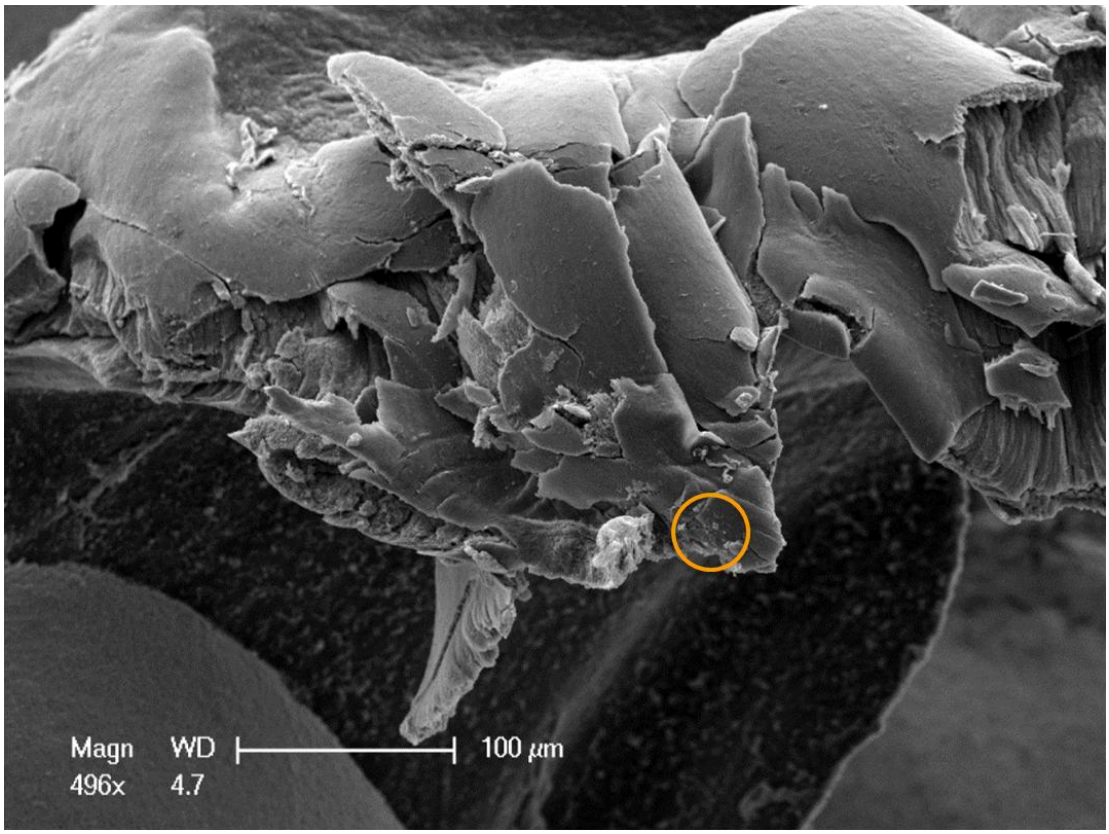

Figure 3.11 Representative fracture of the tooth from an immature zone of the radula shows the fragility of the partially mineralized teeth. SEM images from figures 3.12-3.16 were taken from the tip area of each fractured tooth at the yellow circle shown in the figure.

Analyses of the three regions at the leading edge reveal an increase in aggregate size and a decrease in particle number from the tooth base to its tip (Figure 3.8D-F). Along the tooth, the average mineral aggregate size is 40.5 ± 8 nm at the base, 70.7 ± 14 nm at the middle and 175.0 ± 24 nm at the tip. The aggregate density (number of aggregates per unit area) is 106.2/μm^2 at the bottom, decreasing to 66.9/μm^2 at the middle and 6.4/μm^2 at the tip. At the tip of the tooth, a decrease of particle size and an increase

of particle density from the trailing edge to the leading edge is revealed concurrently with the decrease of the spacing of the organic matrix (Figure 3.8C, F). At the tip of the trailing edge, the particle size is 211.0 ± 29nm and particle density is 2.6/μm^2 (Figure 3.8C).

Loose bundles of fibers are found at the core region of tooth #4. A small amount of mineral particles are found attaching to fibers (Figure 3.9). Mineral aggregates surrounding the organic fiber are representative of the relationship between the mineral and organic in the shell region of the partially mineralized teeth (Figure 3.10).

To fully understand the process of magnetite nanorod formation, the dynamic structural transformation was studied by analyzing the fracture surfaces from the tips of teeth #1 - #4 with SEM (Figure 3.11-3.16). The partially mineralized teeth are more fragile than the mature teeth as they crush more under similar force (Figure 3.11). An increase of particle size coupled with a decrease in the diameter of surrounding fibrillar matrix is found with increasing tooth maturation. Particles measuring 41 ± 6 nm in diameter begin to aggregate along the closely packed fibers at the tip of tooth #1 (Figure 3.12), the location where BS-SEM, TEM, and EDS indicate that mineral is first deposited. The size of the aggregates in the same tooth region increases dramatically to 74 ± 10 nm in tooth #2 (Figure 3.13), where the phase transformation from ferrihydrite to magnetite is initiated as revealed by XRD and μXRF. The aggregates continue to grow to 90 ± 11 nm in tooth #3 (Figure 3.14), 107 ± 18 nm in tooth #4 (Figure 3.15) and finally form continuous rods with diameters 171 ± 20 nm in the fully mineralized teeth (Figures 3.16E

and J). Additionally, the diameters of the fibers decrease from 37 ± 2 nm in tooth #1 to 20 ± 3 nm in tooth #4 and are indistinguishable under SEM in the fully mineralized teeth. The five sequential stages of the formation process of the magnetite rods are arranged in Figure 3.16.

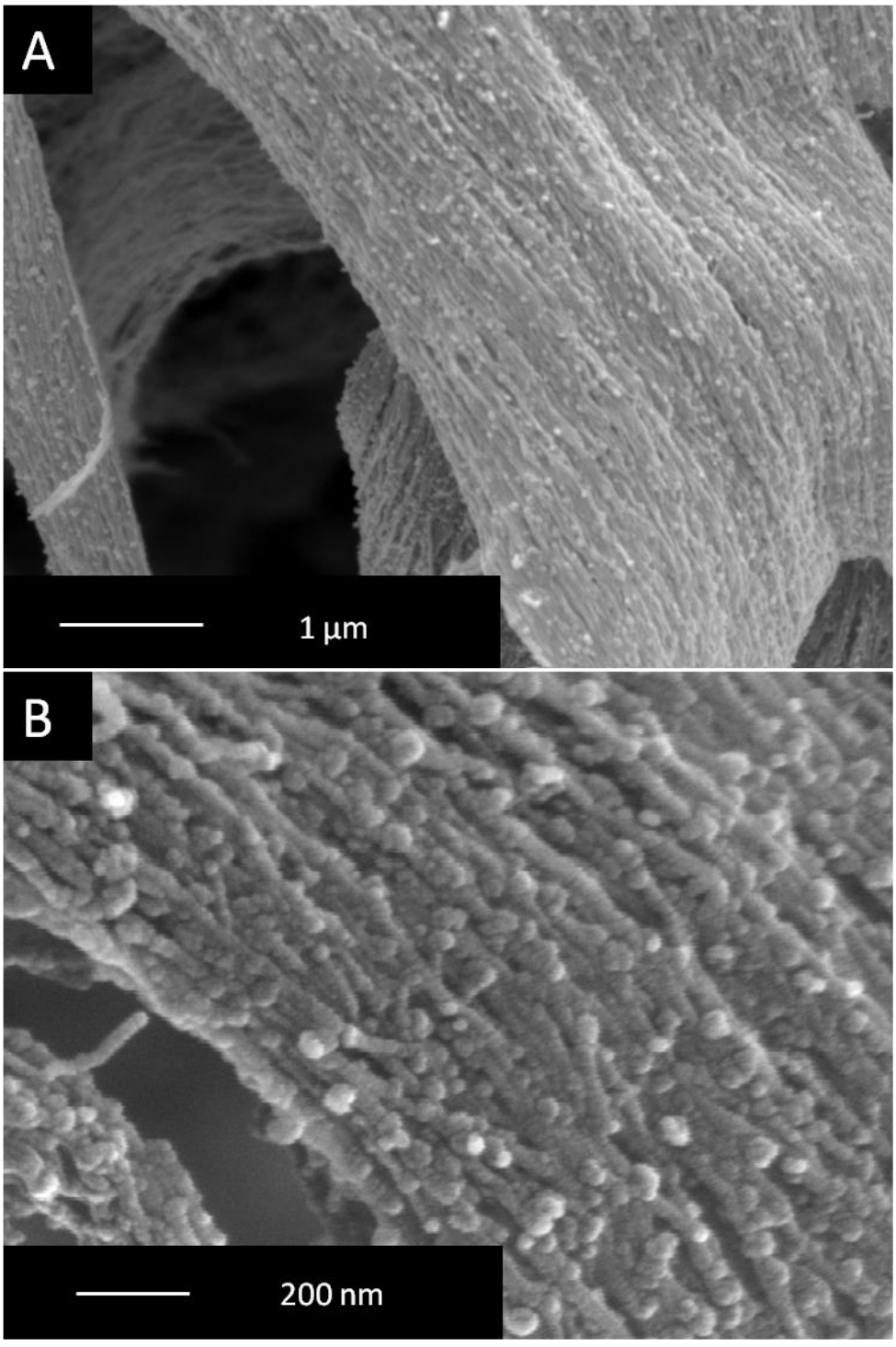

Figure 3.12 SEM imaging showing mineral particles attached to the dense-packing organic fibers were found at the fracture surface of the tip of tooth #1.

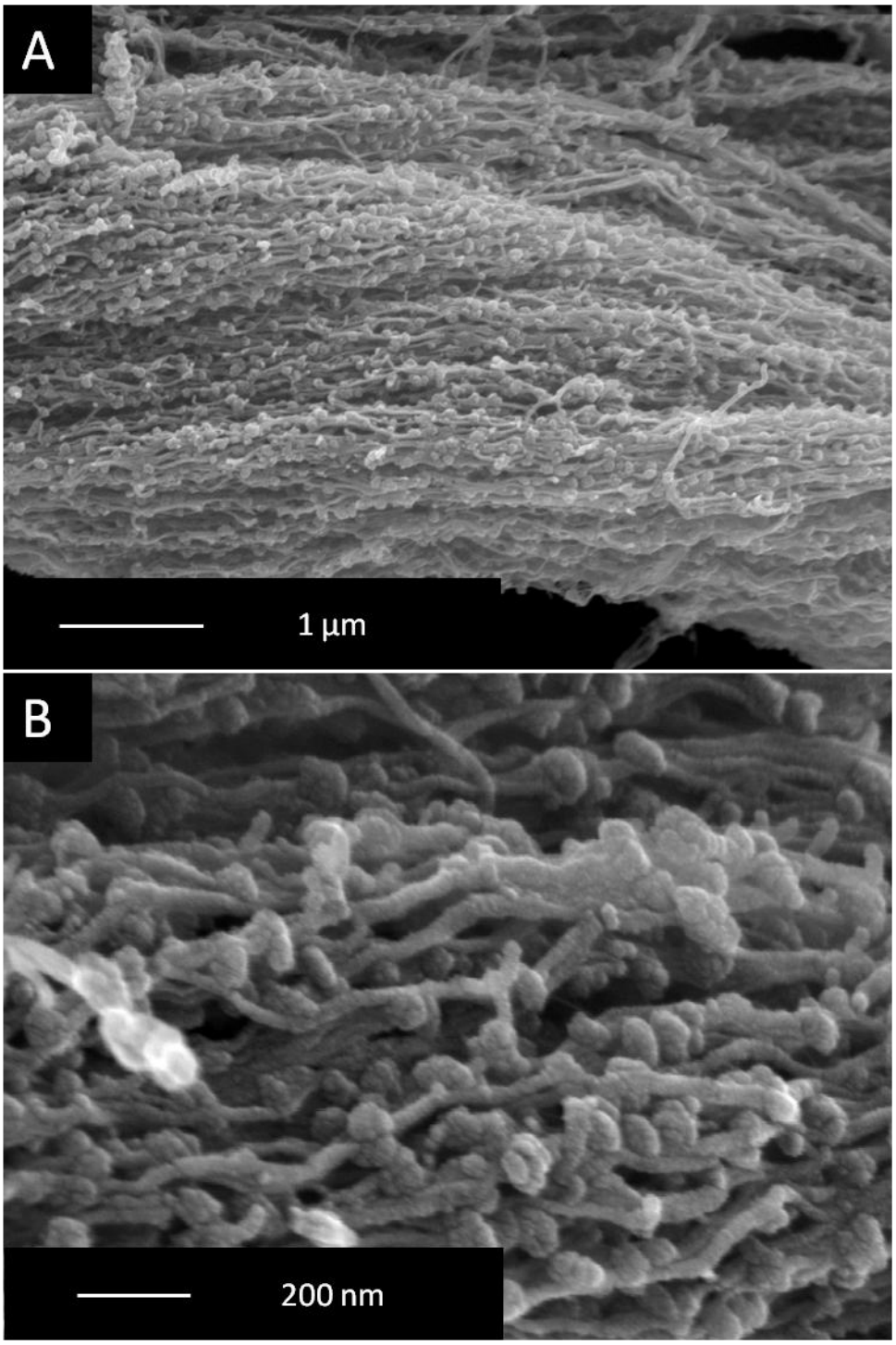

Figure 3.13 SEM imaging showing mineral particles attached to the organic fibers were found at the fracture surface of the tip of tooth #2.

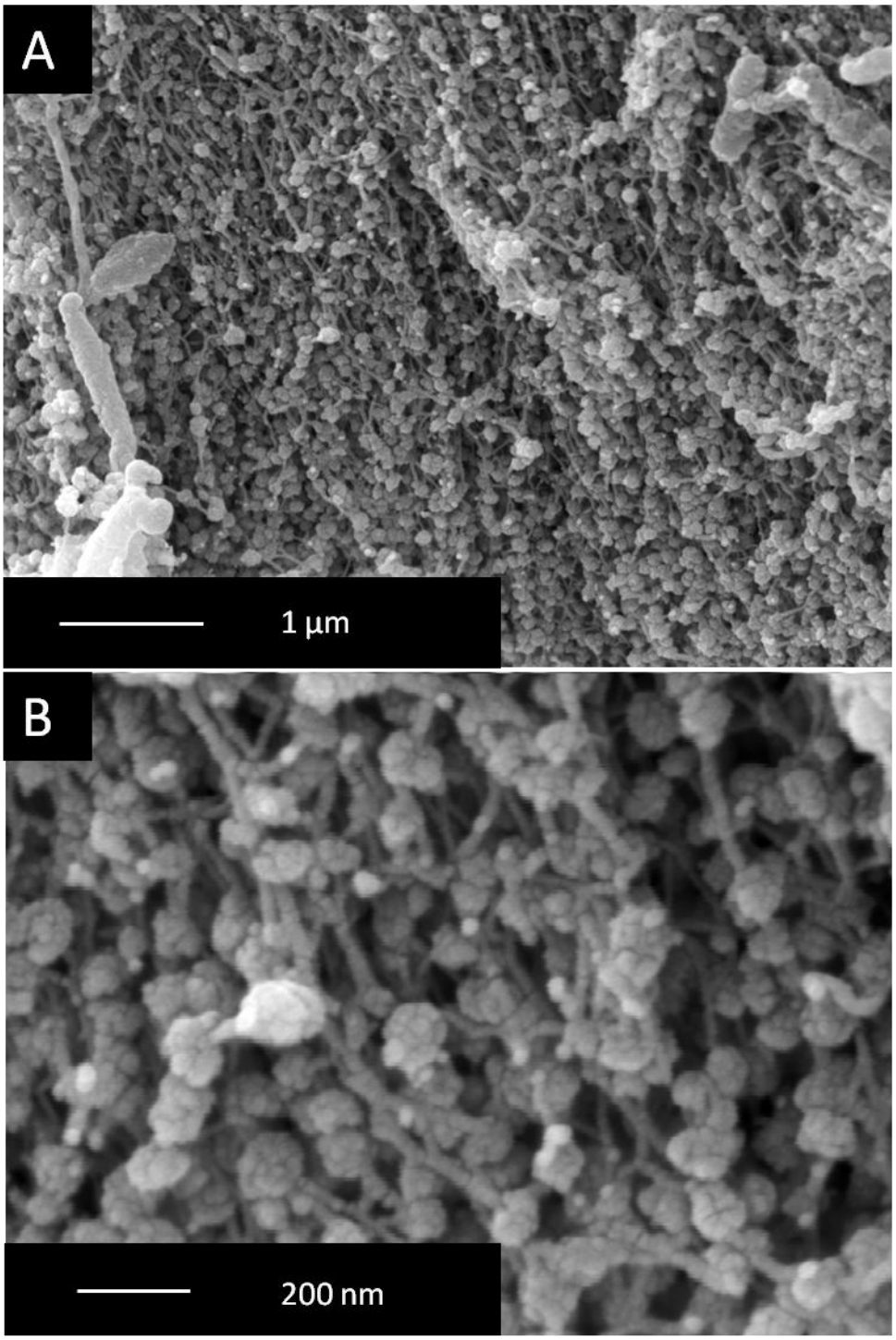

Figure 3.14 SEM imaging showing mineral particles attached to organic fibers were found at the fracture surface of the tip of tooth #3.

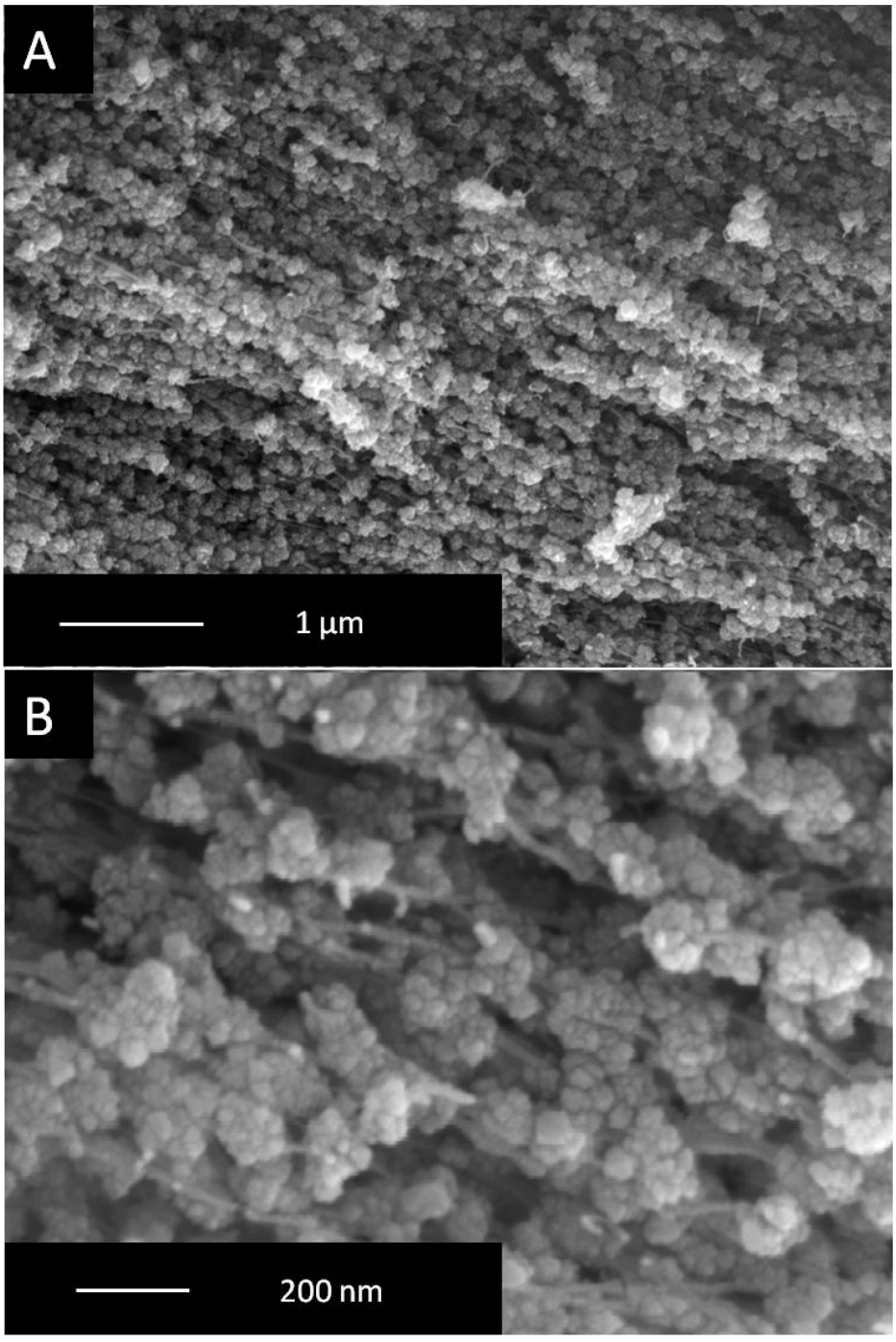

Figure 3.15 SEM imaging showing mineral particles attached to organic fibers were found at the fracture surface of the tip of tooth #4. Semi- rods structures have been revealed.

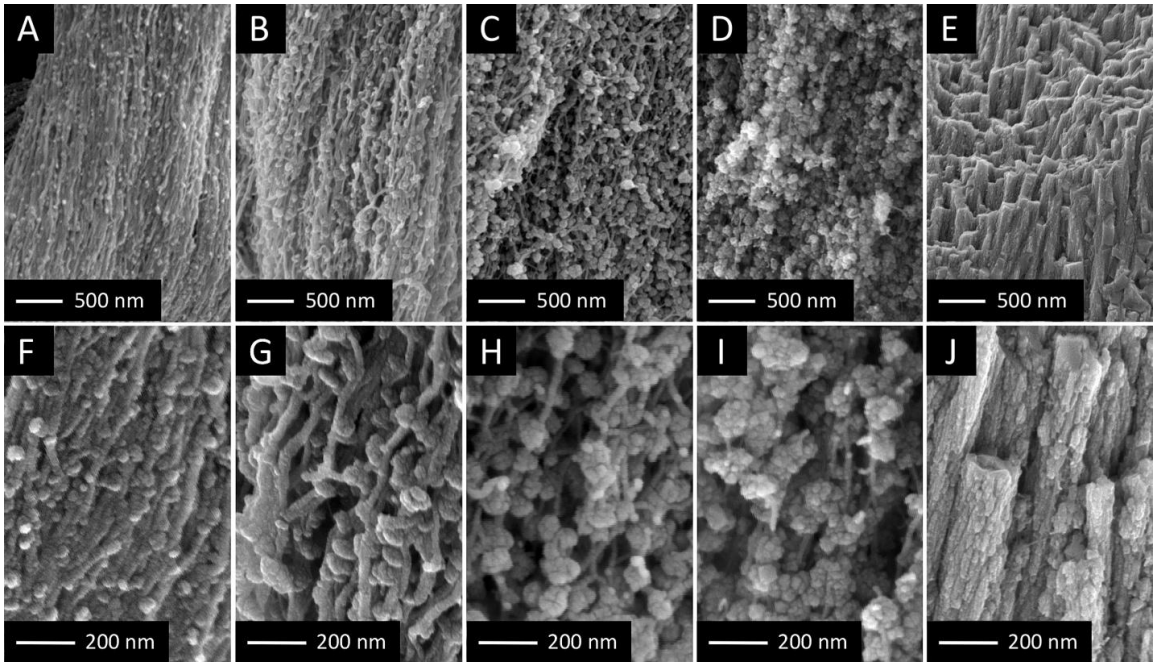

Figure 3.16 Sequential stages of magnetite rod formation during radular tooth maturation. Scanning Electron Microscopy analyses of fracture surfaces from (A,F) the tips of tooth #1, (B,G) tooth #2, (C,H) tooth #3, (D,I) tooth #4 and (E,J) a fully mineralized tooth.

3.3.4 Biomimetic synthesis

To investigate the capability of the nonmineralized teeth at different stages to template ferrihydrite, ferrihydrite nucleation studies were carried out within the nonmineralized teeth. All the 9 nonmineralized teeth used in this study are transparent under optical microscope. We label the tooth right before the initiation of infiltration of mineral (which was labeled as tooth #1) as tooth #-1, so the least mature tooth is #-9 (Figure 3.17A). The shrinkage of the teeth due to sample preparation occurs more significantly on the less mature teeth (#-4 ~ #-9). Close examination of the teeth shows that they consist of organic fibrils with rough surfaces (Figure 3.17B). EDS analysis shows that the weight percent of iron at the tip of tooth #-1 is 3.54, while only 0.61% at

the middle of the same tooth (Figure 3.17C). The weight percentage of iron decreases to 2.32 at the tip of tooth #-2, and 1.06 at the tip of tooth #-3 (Figure 3.17C).

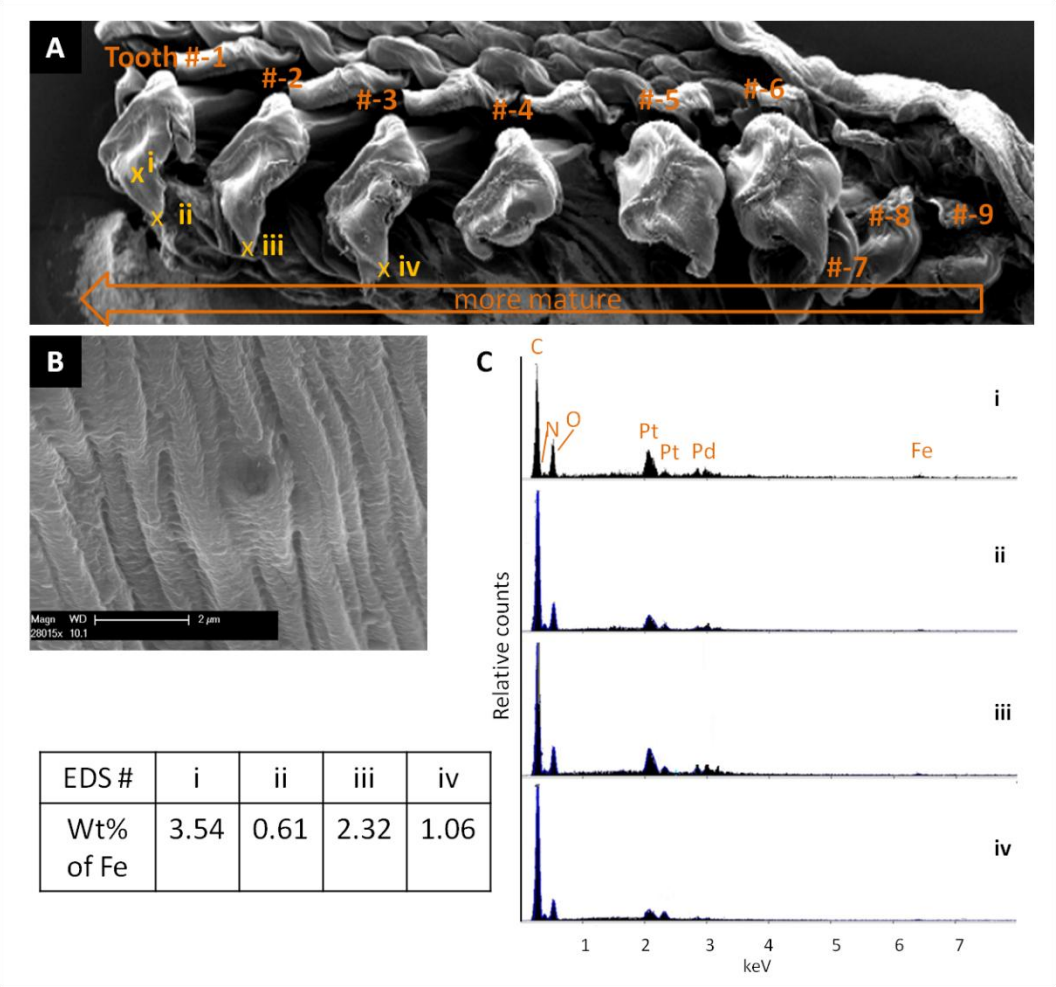

EDS #	i	ii	iii	iv
Wt% of Fe	3.54	0.61	2.32	1.06

Figure 3.17 SEM (A and B) and EDS (C) analysis of biomimetic synthesis of ferrihydrite in nonmineralized radular teeth. The surface of the teeth is made of organic fibrils (B). The "x" in figure A mark the spots of EDS analysis, including the middle (i) and tip (ii) of tooth #-1, the tips of tooth #-2 (iii) and #-3 (iv). Weight percent of Fe in these four areas was calculated by EDS.

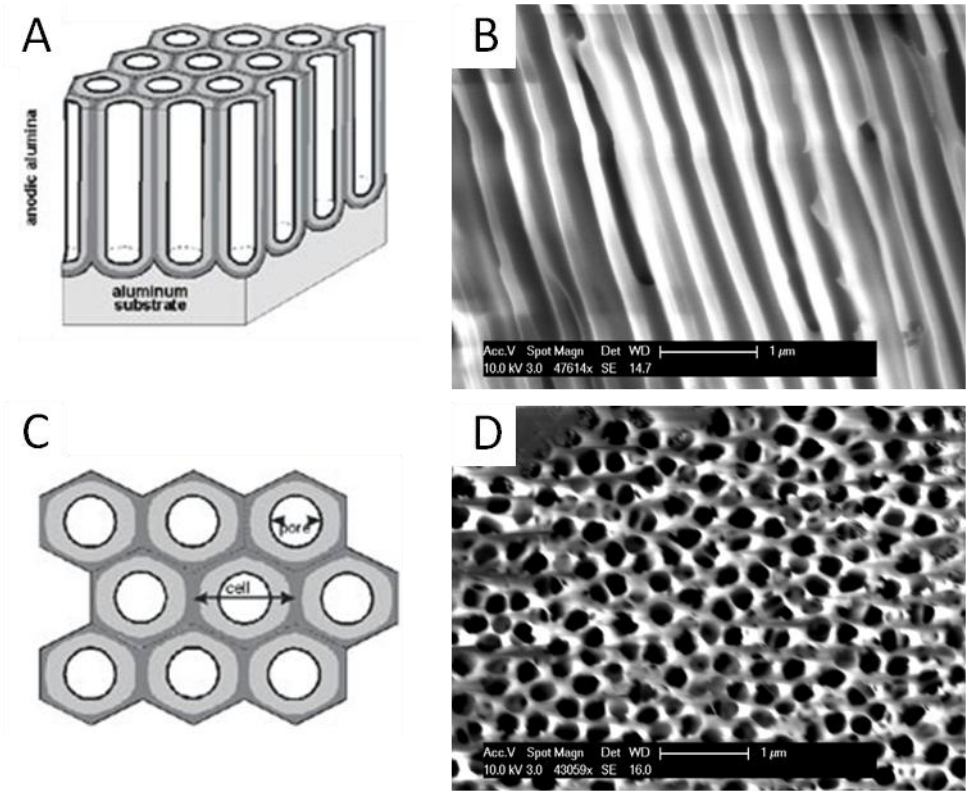

Figure 3.18 Side (A, B) and top (C, D) view of Anodic Aluminum Oxide discs. A and C are cartoon drawing, B and D are from SEM.

In order to verify and mimic the organic matrix controlled mineralization process, ferrihydrite nucleation was performed in Anodic Aluminum Oxide templates (Figure 3.18) by hydrolysis of an aqueous 10^{-2} M $Fe(NO_3)_3 \cdot 9H_2O$ solution at 25°C with pH=7. The reaction parameters, including reaction temperature and pH, were set to be similar as the living habitat of *C. stelleri*, with the exception of the concentration of iron, which is currently not known within the teeth during mineralization. SEM images of the fractured membranes after reaction show that particles deposit on the –OH and -CH3 modified

AAO membranes, but not on the bare AAO templates (Figure 3.19). EDS confirmed that about 0.5% by weight of iron were present on each of the modified membranes.

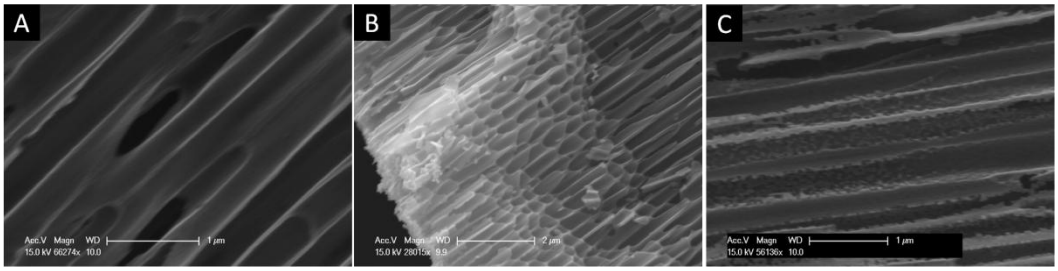

Figure 3.19 SEM analysis on fractured surfaces of biomimetic synthesis of ferrihydrite on bare (A) AAO template and –OH (B), and $–CH_3$ (C) alkanethiol modified AAO templates.

3.4 Discussion

Dynamic studies of the mineralization process of the hard outer magnetite containing region of the radular teeth of *C. stelleri* provides insights of the relationship between the phase transformation and structural development during the four distinct stages of mineralization: *(i)* the formation of a crystalline α-chitin organic matrix that forms the structural framework of the non-mineralized teeth, *(ii)* the synthesis of ferrihydrite particles along these organic fibers, *(iii)* aggregation of the mineral particles with concurrent phase transformation from ferrihydrite to magnetite, and *(iv)*, progressive magnetite crystal growth to form continuous parallel rods within the mature teeth.

3.4.1 Phase Transformation

Chitin $(C_8H_{13}O_5N)_n$ is one of the most abundant biopolymers on the earth and serves as the architectural support for biomineralization in bone, teeth and shell structures for a multitude of organisms. The molecular structure of chitin is known as 2-acetamido-

2-deoxy-β-D-glucose through a β (1→4) linkage (Figure 3.20). Chitin is a white, hard, inelastic, insoluble, nitrogenous polysaccharide and has excellent thermal stability and sturdy mechanical properties. As it is also biodegradable, nontoxic, and physiologically inert, chitin is widely used in wound-dressing, controlled drug release, and tissue engineering. Chitin has also been used as templates for biomimetic studies [48]. Depending on how the polysaccharide is bonded, three crystal structures of chitin can exist: α-chitin, β-chitin, and γ-chitin. Being thermodynamically more stable, α-chitin is much more abundant than the other two phases. Previous studies revealed that α-chitin has a two-chain orthorhombic structure with $P2_12_12_1$ space group [49-51].

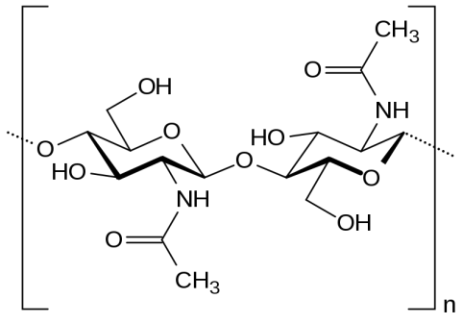

Figure 3.20 Molecular structure of chitin.

Our study demonstrates that α-chitin (which is easily distinguished from the β and γ forms by XRD *[52]*) is the only crystalline organic phase produced in the teeth of *C. stelleri*, confirming the Towe and Lowenstam's speculation about the chitin-like organic fibers in the early stages of radular tooth development [40].

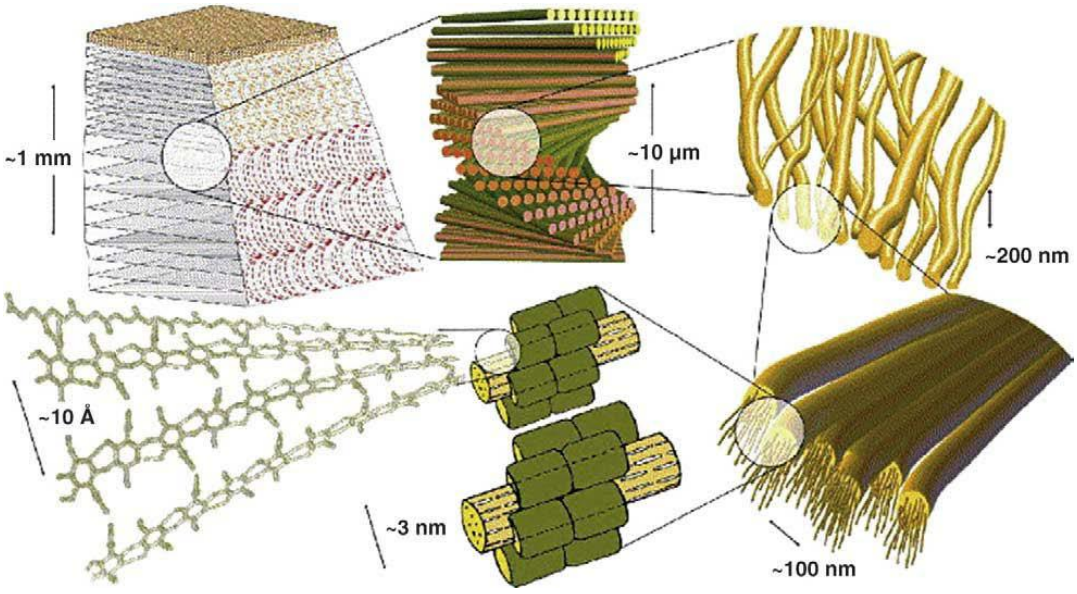

Figure 3.21 The assembled polysaccharide chains of chitin hierarchy organization comprising six structural levels of chitin in crustaceans. Counterclockwise, from the bottom left: A, assembly of the chitin chains to form alpha crystals; B, nanofibrils (clear cylinders) surrounded by proteins (dark); C, settlement of nanofibrils in microfibers of chitin and proteins; D, lamina of a net of fibers of chitin and proteins, calcite crystallizes in the openings; E, arrangement of laminas with a rotating orientation visible under the optical microscope; F, structure of the cuticle (exo and endo) whose plane section shows the typical arched pattern as a consequence of the grades of rotation of the laminas [53].

α-chitin is not strongly implicated for the selection of iron ions as it is also found in biominerals devoid of iron oxides, such as the calcified exoskeletons of crustaceans [54]. The hierarchical organization of chitin in the crustaceans involves six structural levels (Figure 3.21). Chitin, together with the surrounding protein or other macromolecules, induces the nucleation of calcium minerals [55]. In addition, α-chitin alone does not necessarily control the initial phase of the precipitated minerals, as goethite is found to be the initial mineral phase that formed on the chitin fibers within the

radular teeth of limpets [14]. It therefore seems most reasonable that it is the chitin-associated proteins and not the chitinous organic scaffold itself that are responsible for the nucleation, growth and phase transformations within the radular teeth [23].

6-line ferrihydrite was detected after 9 rows of nonmineralized teeth. The longer hydrolysis time results in the better crystallized 6-line ferrihydrite, rather than 2-line ferrihydrite [Schwertmann, From Fe (III) ions to ferrihydrite and then to Hematite]. Kim et al. presumed that the iron transported into the radular teeth of chiton *Acanthopleura hirtosa* was Fe(II), which then oxidized to form ferrihydrite [12]. However, our μXRF data provides evidence that ferrous iron is present after ferric iron. Therefore, the suggested redox mechanism of ferrihydrite formation in *Acanthopleura hirtosa* does likely not apply to the radular teeth in *C. stelleri*. Since the natural habitat of *C. stelleri* is at ~15 °C, we propose that ferric iron hydrolyzes in water and forms positively charged ferric iron hydroxides [56]. Due to the low solubility of Fe(III) compounds at near-neutral pH, similar to that of seawater, supersaturation with respect to ferrihydrite solubility can rapidly occur, resulting in the spontaneous precipitation of metastable ferrihydrite.

Heterogeneous nucleation induced by chitin fibers covered with macromolecules has been found in calcified biomineralization [55]. Heterogeneous nucleation, which is considered as crystal nucleation process catalyzed or assisted by surface features, occurs more readily than homogeneous nucleation. The Gibbs free energy of heterogeneous nucleation is lower than that of homogeneous nucleation due to the presence of surfaces, which have unsatisfied bonds. For same material, the critical radius for nucleation is

constant during all the nucleation processes. However, the total volume required during heterogeneous nucleation is smaller than homogeneous nucleation due to the difference in activation energy (Figure 3.22). In another words, a lower supersaturation is required for heterogeneous nucleation.

Nucleation of ferrihydrite occurs on the alkanethiol molecules (with –OH, and -CH_3 function groups) modified AAO membranes, but not on the bare ones. The alkanethiol solution forms a single layer of molecular species on the surface of the AAO templates (Figure 3.24). These two functional groups (OH and CH_3) are also found in α-chitin molecules (Figure 3.20). Although the mechanism regarding how α-chitin assists in the mineralization process has not been uncovered, this biomimetic work confirms that the –OH and –CH_3 groups on α-chitin does facilitate the ferrihydrite nucleation.

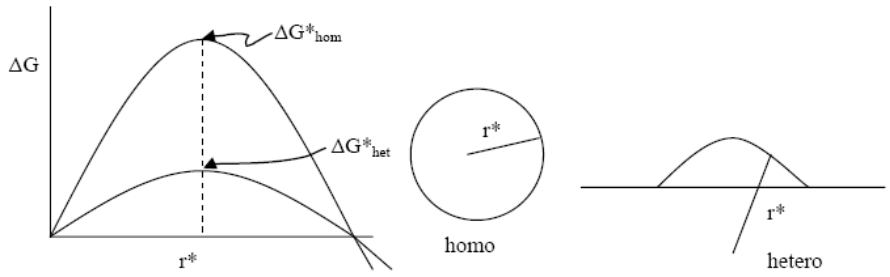

Figure 3.22 Gibbs free energy required for heterogeneous nucleation is lower than that for homogeneous nucleation. Smaller volume of materials is required for heterogeneous nucleation due to a lower activation energy barrier.

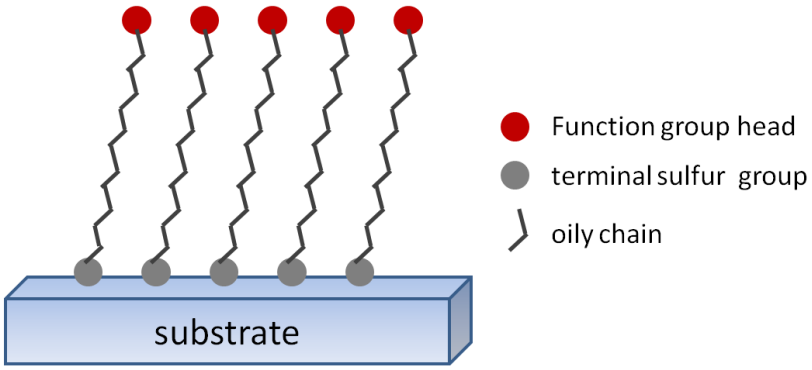

Figure 3.23 Alkanethiols self-assembled on substrate.

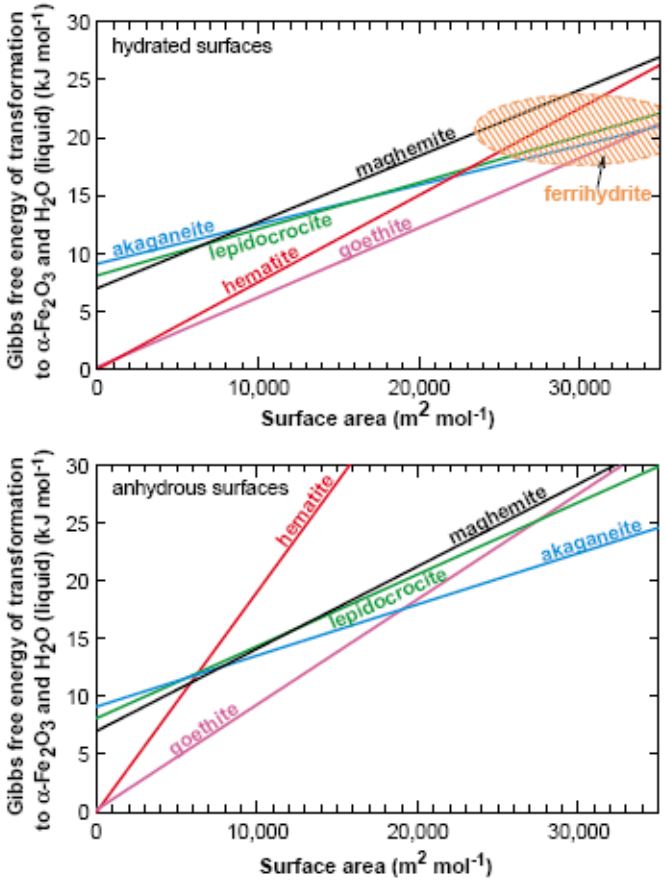

Figure 3.24 Enthalpy, relative to coarse Fe_2O_3 (hematite) plus liquid water at 298 K, of various iron oxide and oxyhydroxide polymorphs as a formation of surface area per mole of $FeO_{1.5}$, FeOOH, or $Fe(OH)_3$ [57].

From TEM images of the radular teeth, all the mineral particles are attached to the organic fibers, demonstrating heterogeneous nucleation and ferrihydrite is synthesized *de novo*. The α-chitin fibers, likely coated with iron-attracting peptides, provide nucleation sites for the ferrihydrite. Since the Gibbs free energy of ferrihydrite formation is comparable to other iron oxides like goethite (α-FeO(OH)), lepidocrocite (γ-FeO(OH)), or akaganeite (β-FeO(OH)), and the surface enthalpies of hydrous phases are lower than that of anhydrous ones, it is not surprising that the first mineral phase appearing in radular teeth is ferrihydrite (Figure 3.24) [56].

An increase of the capability for templating ferrihydrite nucleation with the maturity of nonmineralized teeth is observed from the biomimetic synthesis of ferrihydrite in 9 nonmineralized teeth (Figure 3.17). This suggests that the maturity of the organic complex (including the structure of matrix and the concentration of peptides) helps control of the initiation of the mineralization. The fact that much less iron was detected at the middle of tooth #-1 than at the tip confirms our observation that the mineralization process initiates at the tip of the radular teeth.

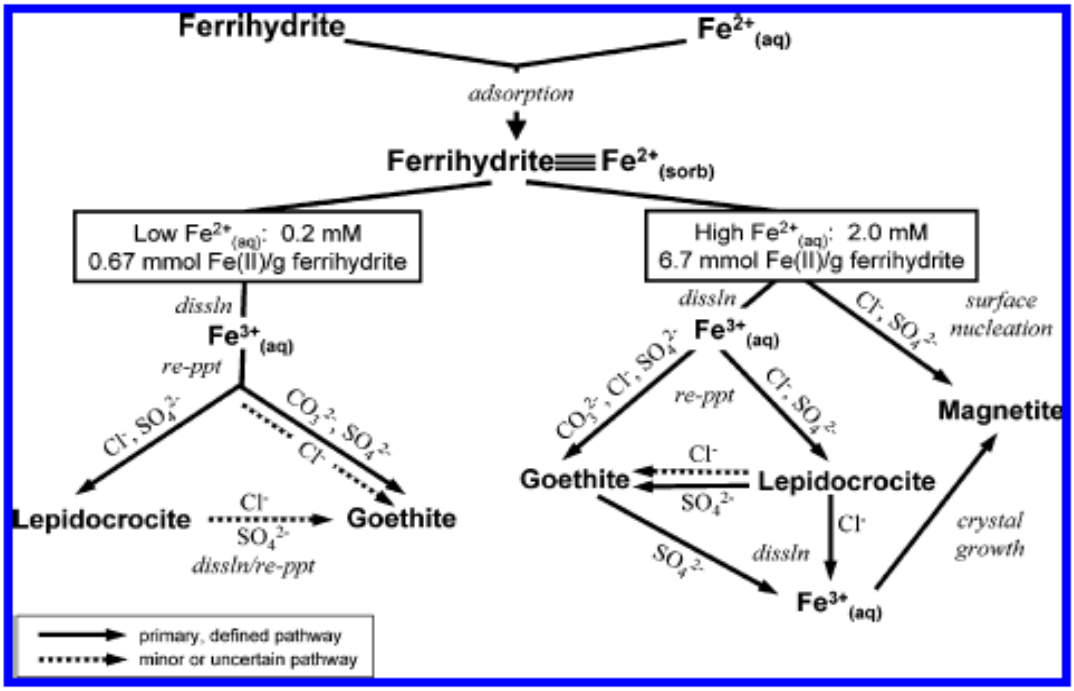

Figure 3.25 Conceptual model from Hansel et al. depicting the secondary phase transformation of ferrihydrite as a function of Fe(II) concentration and ligand (circumneutral pH). dissln = dissolution; re-ppt = reprecipitation.

A phase transformation from ferrihydrite to magnetite is initiated at tooth #2, where a dramatic increase of particle size occurs. Following nucleation, crystal growth and aggregation ultimately results in a reduction of free surface area, thus making the hydrolyzed structure thermodynamically less stable and susceptible to transformation. Furthermore, a metastable mineral phase, nanocrystalline ferrihydrite, with active adsorption sites on its surface, tends to transform to thermodynamically more stable phases. The crystal structure of ferrihydrite ($5Fe_2O_3 \cdot 9H_2O$) belongs to the P-31c group and is thermodynamically less stable than the inverse-spinel structure of magnetite (Fe_3O_4) [44, 46]. One reason for this is that the ferrihydrite contains face-sharing

octahedra, which places the iron ions closer to each other, thereby increasing the repulsive forces between them. This phase transformation first occurs at the tip of the leading edge of the radular teeth, where more ferrihydrite is formed and the critical particle size at which ferrihydrite becomes unstable relative to other iron oxide phases is achieved. Study of secondary phase transformations from ferrihydrite to magnetite, goethite or lepidocrocite were performed by Hansel et al. and a computing model of these phase transformations have been built. According their study, the phase transformation from ferrihydrite to magnetite can be achieved by surface nucleation when the Fe(II) concentration is high (Figure 3.25).

3.4.2 Structural Development

The underlying α-chitin organic matrix appears to influence magnetite particle density (number of particles per unit area) and the diameter and curvature of the resulting rods, all of which likely play critical roles in determining the local mechanical properties of the mature radular teeth.

We have measured both particle diameters and spacing between α-chitin fibrils. Interestingly, an identical ratio, approximately 1.8, of the particle size to the spacing between fibers is found in three separate regions (i.e., where the spacing between fibers is clear enough to calculate (Figure 3.8C, F and TEM image from the middle of the trailing edge that is not shown). The average spacing between fibers at the middle of the trailing edge is 56 ± 13 nm, which is much smaller than the 116n ± 35 nm average spacing at the top of the trailing edge. The average spacing between fibers at the tip of the leading edge

is about 106 ± 24 nm, which is also smaller than that at the tip of the trailing edge. The fact that the mineral particle size is coupled to the spacing between organic fibers suggests that the α-chitin fiber matrix plays a major role in determining the rod structure within the shell region. We believe that this spacing, in conjunction with proteins that are likely affiliated with the α-chitin, regulates the supersaturation levels in a confined environment and therefore controls nucleation of mineral. At the leading edge, where there is a denser packing of fibers, we can expect a greater confinement of mineral nutrient and therefore, a higher supersaturation level leading to a greater density of small nuclei and thus, smaller diameter rods. In the trailing edge, the fibers are sparser and thus, we expect a lower number of nuclei, which will subsequently grow to larger diameters and subsequently, larger diameter rods.

In addition, ionic strength and other local environmental conditions can have profound effects on nucleation density and particle aggregation, and thus may play important roles in differentially regulating these phenomena in the proximal and distal regions of the mineralizing teeth. As discussed earlier, the resulting size of these aggregated particles also affects the likelihood of phase transformations; accordingly, the presence of these organic matrices precisely controls the resulting mineral size, phase and morphology and subsequently, the mechanical performance of this regionally modified composite.

3.5 Conclusions

The results reported here detail the dynamic phase and microstructural transformations that occurs during mineralization in the radular teeth of *C. stelleri*. Mineralization is initiated via the deposition of six-line ferrihydrite aggregates at the leading edge of the tooth tips. These aggregates subsequently transform to magnetite, which further grow into highly oriented rod-like elements that exhibit regionally defined geometries that depend of the periodic spacing of the surrounding organic matrix and in turn affect the regional mechanical properties of the mature teeth. These studies into the biomineralization processes in the radular teeth of *C. stelleri* illustrate several design principles that could be potentially applied to not only the biomimetic synthesis of iron oxides, but also for the spatially confined template-directed growth of a wide range of inorganic materials and structural ceramics with graded moduli.

3.6 Acknowledgements:

We thank Sara Krause for the illustration in Figure 1A, Dr. Kenneth Evans-Lutterodt of the National Synchrotron Light Source in Brookhaven National Laboratory for contributing his expertise at the microdiffraction endstation X13B, Dr. Vesna Stanic of the NSLS in BNL for her help in conducting experiments at the diffraction endstation X6B, Dr. Sam Webb of Stanford Synchrotron Radiation Lightsource for his instrumental help with the μXRF measurements, and John Stegemeier and Dr. Christopher Kim from Chapman University for their help with μXRF analysis and interpretation. The NSLS is supported under USDOE Contract DE-AC02-98CH10886. Portions of this research were carried out at the Stanford Synchrotron Radiation Lightsource, a Directorate of SLAC

National Accelerator Laboratory and an Office of Science User Facility operated for the U.S. Department of Energy Office of Science by Stanford University.

3.7 References

[1] L. Addadi, S. Weiner, *Angewandte Chemie-International Edition in English* **1992**, *31*, 153.

[2] C. Santulli, *Proceedings of the International School on Advanced Material Science and Technology* **2004**.

[3] J. C. Weaver, Q. Q. Wang, A. Miserez, A. Tantuccio, R. Stromberg, K. N. Bozhilov, P. Maxwell, R. Nay, S. T. Heier, E. DiMasi, D. Kisailus, *Materials Today* **2010**, *13*, 42.

[4] J. C. E. Ricketts, *Between Pacific Tides: Fifth Edition*, Stanford University, Stanford **1985**.

[5] S. W. Heinz A. Lowenstam, *On biomineralization*, Oxford University Press, **1989**.

[6] D. P. A. R. H. Morris, E. C. Haderlie, *Intertidal Invertebrates of California*, Stanford Press, Stanford **1980**.

[7] J. A. Shaw, D. J. Macey, L. R. Brooker, *Journal of the Marine Biological Association of the United Kingdom* **2008**, *88*, 597.

[8] P. van der Wal, H. J. Giesen, J. J. Videler, *Materials Science and Engineering C* **2000**, *7*.

[9] J. A. Shaw, D. J. Macey, L. R. Brooker, E. J. Stockdale, M. Saunders, P. L. Clode, *Microscopy and Microanalysis* **2009**, *15*, 154.

[10] N. W. Runham, *Quarterly Journal of Microscopical Science* **1963**, *104*, 271.

[11] H. K. Lu, C. M. Huang, C. W. Li, *Experimental Cell Research* **1995**, *219*, 137.

[12] K. S. Kim, D. J. Macey, J. Webb, S. Mann, *Proceedings of the Royal Society of London Series B-Biological Sciences* **1989**, *237*, 335.

[13] J. A. Shaw, D. J. Macey, L. R. Brooker, E. J. Stockdale, M. Saunders, P. L. Clode, *Journal of Morphology* **2009**, *270*, 588.

[14] E. D. Sone, S. Weiner, L. Addadi, *Journal of Structural Biology* **2007**, *158*, 428.

[15] B. Rinkevich, *Marine Biology* **1993**, *117*, 269.

[16] C. M. Huang, C. W. Li, M. C. Deng, T. S. Chin, *Ieee Transactions on Magnetics* **1992**, *28*, 2409.

[17] M. R. Carriker, J. G. Schaadt, V. Peters, *Marine Biology* **1974**, *25*, 63.

[18] D. A. Smith, *Journal of Experimental Biology* **1988**, *136*, 89.

[19] P. van der Wal, H. J. Giesen, J. J. Videler, *Materials Science & Engineering C-Biomimetic and Supramolecular Systems* **2000**, *7*, 129.

[20] N. W. Runham, *Quarterly Journal of Microscopical Science* **1961**, *102*, 371.

[21] N. W. Runham, P. R. Thornton, D. A. Shaw, R. C. Wayte, *Zeitschrift Fur Zellforschung Und Mikroskopische Anatomie* **1969**, *99*, 608.

[22] M. S. Davies, D. J. Proudlock, A. Mistry, *Ecotoxicology* **2005**, *14*, 465.

[23] L. A. Evans, D. J. Macey, J. Webb, *Marine Biology* **1991**, *109*, 281.

[24] L. A. Evans, D. J. Macey, J. Webb, *Calcified Tissue International* **1992**, *51*, 78.

[25] A. P. Lee, J. Webb, D. J. Macey, W. van Bronswijk, A. R. Savarese, G. C. de Witt, *Journal of Biological Inorganic Chemistry* **1998**, *3*, 614.

[26] D. J. Macey, L. R. Brooker, J. Webb, T. G. StPierre, *Acta Zoologica* **1996**, *77*, 287.

[27] M. Saunders, C. Kong, J. A. Shaw, P. L. Clode, *Microscopy and Microanalysis* **2011**, *17*, 220.

[28] M. Saunders, C. Kong, J. A. Shaw, D. J. Macey, P. L. Clode, *Journal of Structural Biology* **2009**, *167*, 277.

[29] A. P. Lee, L. R. Brooker, D. J. Macey, J. Webb, W. van Bronswijk, *Journal of Biological Inorganic Chemistry* **2003**, *8*, 256.

[30] H. A. Lowenstam, *Science* **1967**, *156*, 1373.

[31] L. R. Brooker, A. P. Lee, D. J. Macey, W. van Bronswijk, J. Webb, *Marine Biology* **2003**, *142*, 447.

[32] C. W. Li, T. S. Chin, J. S. Li, S. H. Huang, *Ieee Transactions on Magnetics* **1989**, *25*, 3818.

[33] H. A. Lowenstam, S. Weiner, *Science* **1985**, *227*, 51.

[34] D. J. Macey, L. R. Brooker, *Journal of Morphology* **1996**, *230*, 33.

[35] H. A. Lowenstam, S. Weiner, *On Biomineralization*, Oxford University Press, Oxford **1989**.

[36] R. H. Morris, D. P. Abbott, E. C. Haderlie, *Intertidal Invertebrates of California*, Stanford Press, Stanford **1980**.

[37] E. Ricketts, J. Calvin, *Between Pacific Tides: Fifth Edition*, Stanford University, Stanford **1985**.

[38] M. F. Ashby, L. J. Gibson, U. Wegst, R. Olive, *Proceedings of the Royal Society of London Series a-Mathematical and Physical Sciences* **1995**, *450*, 123.

[39] K. M. Towe, H. A. Lowenstam, M. H. Nesson, *Science* **1963**, *142*, 63.

[40] K. M. Towe, H. A. Lowenstam, *Journal of Ultrastructure Research* **1967**, *17*, 1.

[41] J. L. Kirschvink, H. A. Lowenstam, *Earth and Planetary Science Letters* **1979**, *44*, 193.

[42] P. A. O'day, N. Rivera, R. Root, S. A. Carroll, *American Mineralogist* **2004**, *89*, 572.

[43] S. M. Webb, *Physica Scripta* **2005**, *T115*, 1011.

[44] B. A. Wechsler, D. H. Lindsley, C. T. Prewitt, *American Mineralogist* **1984**, *69*, 754.

[45] K. M. Paralikar, R. H. Balasubramanya, *Journal of Polymer Science Part C-Polymer Letters* **1984**, *22*, 543.

[46] E. Jansen, A. Kyek, W. Schafer, U. Schwertmann, *Applied Physics a-Materials Science & Processing* **2002**, *74*, S1004.

[47] L. E. Mayhew, S. M. Webb, A. S. Templeton, *Environmental Science & Technology* **2011**, *45*, 4468.

[48] K. E. Park, S. Y. Jung, S. J. Lee, B. M. Min, W. H. Park, *International Journal of Biological Macromolecules* **2006**, *38*, 165.

[49] R. Minke, J. Blackwell, *Journal of Molecular Biology* **1978**, *120*, 167.

[50] Y. Saito, T. Okano, H. Chanzy, J. Sugiyama, *Journal of Structural Biology* **1995**, *114*, 218.

[51] P. Sikorski, R. Hori, M. Wada, *Biomacromolecules* **2009**, *10*, 1100.

[52] M. K. Jang, B. G. Kong, Y. I. Jeong, C. H. Lee, J. W. Nah, *Journal of Polymer Science Part a-Polymer Chemistry* **2004**, *42*, 3423.

[53] P. Morganti, G. Morganti, *Clinics in Dermatology* **2008**, *26*, 334.

[54] M. M. Giraudguille, *Tissue Cell* **1984**, *16*, 75.

[55] G. Falini, S. Albeck, S. Weiner, L. Addadi, *Science* **1996**, *271*, 67.

[56] C. F. Baes, R. E. Messmer, *The Hydrolysis of Cations*, John Wiley & Sons Inc, **1976**.

[57] A. Navrotsky, L. Mazeina, J. Majzlan, *Science* **2008**, *319*, 1635.

4 Chapter 4. Structure and function relationship of the mature radular tooth in *C. Stelleri*

4.1 Introduction

Composite materials, with extraordinary mechanical performance and simplified manufacturing processes, have been utilized to achieve the specific design requirements in industry. Nature has developed mechanisms for organisms to obtain composites that exhibit extraordinary mechanical properties through millions of years of evolution. Abrasion resistant and self-sharpening materials have broad applications in both military and daily life, like tunnel boring, oil drilling and shaping and machining tools. Design principles of the abrasion resistant and self-sharpening materials can be obtained and optimized by learning from biological systems. *Cryptochiton stelleri*, mollusks living at the intertidal line of the ocean, feed on the algae growing on and inside the hard surface of rocks using a conveyer belt-like toothed structure, which is called a radula. The radular teeth are hard and abrasion resistant to eat away the rock together with algae. The hard and abrasion resistant outer layer of the radular teeth is a composite made of polycrystalline magnetite nanorods surrounded by α-chitin layers. By identifying the local micro- and nanostructures, mechanical properties, combined with using finite elemental analysis of the observations of the hard veneer of the teeth, we aim to provide designing strategies for abrasion resistant and shelf-sharpening composite materials that can be applied in industry.

Composite materials, or composites, are loosely defined as "engineered or naturally occurring materials made from two or more constituent materials with significantly different physical or chemical properties which remain separate and distinct within the finished structure". With heterogeneous structures, composites fulfill the requirements for specific working conditions and functions. Mankind has being using composite materials for thousands of years even without being fully aware about how those composites succeeded in improving daily life; for example, they found that the houses built with bricks lined with straw are more stable and last longer than those without straw. Today, with prosperous research and incredible technique developments during the past decades, composites have found their applications in multiple areas, including glass fiber-reinforced composites in automobile bodies and particulate composites for aerospace use.

There are two ways to classify composites, referring to the types of the matrix constituent or the reinforcement form. With respect to the matrix constituent, the major composites can be divided into four classes: Metal Matrix Composites (MMCs), Ceramic Matrix Composites (CMCs) and Organic Matrix Composites (OMCs). Organic matrix composites refer to two types of composites, Polymer Matrix Composites (PMCs) and carbon matrix composites, which refer to carbon-carbon composites.

The basic mechanical functions of the matrix in composites are (i) binding the reinforcement in place and (ii) deforming to distribute the stresses under applied forces. On the other hand, modified organic matrices as templates for crystal nucleation, growth

or aggregation have been developed and provide a different aspect to materials synthesis [1, 2].

Based on the reinforcement form, three classes of composites have been identified: fiber reinforced composites, laminar composites and particulate composites, which refer to the reinforcement forms embedded in matrix: fibers, layers of materials and particles, respectively.

For fiber-reinforced composites, if the elastic modulus of the composite varies with the length of the fiber, they are considered as discontinuous or short fiber composites. If not, the composites are defined as continuous fiber reinforcement. Orientation of fibers is crucial for their mechanical performance in both short and continuous fiber composites. It has been shown that composites achieve the highest strength when the long axis of the fibers is along the loading direction [3]. Both organic and inorganic fibers have been utilized nowadays, including glass fibers, boron fibers, metal fibers and wires, graphite fibers, silicon carbide fibers, high silica and quartz fibers, alumina fibers, aramid fibers, and multiphase fibers. Among these, glass fibers are the most widely used, making up 95% of the market.

Composites typically do not fail catastrophically as the reinforcements do not fail at the same time and the matrix usually remains intact after the failure of reinforcements [4]. This makes the composites highly desirable in multiple areas.

Mechanical properties of materials depend on their structure at both the nano- and macroscales. According to European commission, nanomaterials are defined as: “A

natural, incidental or manufactured material containing particles, in an unbound state or as an aggregate or as an agglomerate and where, for 50% or more of the particles in the number size distribution, one or more external dimensions is in the size range 1 nm – 100 nm. In specific cases and where warranted by concerns for the environment, health, safety or competitiveness, the number size distribution threshold of 50% may be replaced by a threshold between 1 and 50%."

With large volume fractions of grain boundaries, the mechanical behavior of nanomaterials is quite different from conventional coarse-grained polycrystalline materials. Remarkably higher strength and strain to failure of nanocrystalline Cu and Pd compared to their coarse-grained counterpart have been observed [5]. Mechanisms of plastic deformation vary based on the size of the grains and three regimes have been claimed by several investigators with atomistic simulations: i) for grains with $d > 1$ μm, the plasticity is controlled by unit dislocations and work hardening; ii) for grains smaller than 10 nm, the plasticity is controlled by the grain-boundary shear caused by limited intragranular dislocation activity; iii) for grains with size is between 10 nm to 1 μm, the mechanism is less well understood [6, 7].

A single radula consists of about 50-80 rows of teeth mounted on organic styli. The teeth are either tricuspid or unicuspid. Each of them consists of a hard shell and a soft core. Old radular teeth are replaced by new teeth continuously. New teeth, which are nonmineralized, grow at the posterior end of the radula, and then get infiltrated with mineral during maturation, utilized in the feeding process, and are finally worn and

separated from the radular base. Research on the radular teeth has been carried out mainly on two groups of mollusks, the chitons (*Polyplacophora*) and the limpets (*Gastropoda*). Mature radular teeth of the limpets are made of goethite within the shell and silica mineral in the core [8-17], while the teeth of chitons consist mainly magnetite within the shell and apatite or iron phosphate in the core [18-34].

Studies of the function and service life of the radula have been carried out on several species. A study of the replacement mechanism of the pulmonate radula from *L. stagnalis* and *Helix pomatia* shows that the radular teeth are attached to the lateral radula tensor muscles by the subradular membrane [35]. The radula kinematics during grazing in *Helisoma trivolvis* (gastropoda pulmonata) involves the sliding of the radula over the underlying cartilage while the cartilage accelerates independently across the substrate during each feeding process to optimize both the food excavation and the food transportation [12]. Comparisons of the tooth use and wear from three species, *Acanthopleura hirtosa* and *Plaxiphora albida* (both chitons) and *Patelloida alticostata* (limpet), shows that unicuspid radulae work like a spade and eat algae beneath the rock, while tricuspid radulae (like ones from *Cryptochiton stelleri*) work like a rake and eat the algae on the surface of the rock [36]. The production rates of the three aforementioned species are 0.40, 0.36 and 0.51 rows per day [37]. Research on the shape, internal structural, positioning and distribution of hardness and elastic moduli of eight species of chitons and one species of limpets showed that all these parameters contributed concertedly in minimizing the wear rates of the teeth and optimizing cutting behavior. The self-sharpening characteristics of these radular teeth were discussed to be

implemented into industrial cutting devices [14]. The highest hardness and modulus of biominerals reported was found at the leading edge of radular teeth in *Cryptochiton stelleri*. The hard shell of the mature radular teeth in *C. stelleri* consists of ca. 250nm rod-like magnetite bundles [27].

In this study, the local micro- and nanostructures and mechanical properties of the hard outer shell of mature radular teeth were analyzed with Scanning Electron Microscope (SEM), Transmission Electron Microscopy (TEM) and Nanoindentation. The function of the tooth was verified using Finite Element Analysis with Abaqus. The relationship between these specific structures and their mechanical performance were discussed to provide design strategies for abrasion resistant composites.

4.2 Materials and Experiments

4.2.1 Research Specimens

Live specimens of *Cryptochiton stelleri* were collected from the temperate Eastern Pacific Ocean (Monterey, CA) and maintained in circulating seawater system at 15 °C before use. Collection of *Cryptochiton stelleri* is permitted by the Department of Fish and Game and the California Natural Resources Agency. The radulae were dissected from these specimens and rinsed in fresh seawater to remove any loose organic debris.

4.2.2 SEM

For fracture surface analyses, a single tooth still attached to the basal ribbon were cut from an intact radula with a razorblade and then serially dehydrated to 100% ethanol. The tooth rows were then critically point dried with CO_2, and mounted on an aluminum

pin mount with conductive carbon tape. Silver paste was applied between the base of the tooth and the carbon tape to reduce charging from the SEM. Fracture surfaces of these teeth were created via impact with a razorblade. The samples were gold coated and then imaged with an XL30-FEG Scanning Electron Microscope at 10 kV.

4.2.3 TEM

To investigate the nanostructures at the surface of the leading edge, a mature tooth was cut from an intact radula with a razorblade and then fixed with gluteraldehyde (2.5%) in HEPES buffer (0.2M, pH = 7.2) for 2 hours. The sample was then serially dehydrated to 100% ethanol, embedded in Spurrs resin and cured for 24 hours at 60°C. The obtained resin block was sectioned with a diamond saw and polished in the longitudinal direction with silicon carbide grit paper to P1200 followed by polishing with diamond lapping films down to 0.25 μm. A longitudinal section of the middle cusp of the mature tooth was obtained. About 100nm thin sections from both the leading and trailing edge were milled from the longitudinal section with Focused Ion Beam (FIB, Leo Gemini, 1540XB) and imaged using a FEI-PHILIPS CM300 TEM at 300 kV accelerating voltage.

4.2.4 Nanoindentation

Full-map indentation tests were performed on cross-sections through the longitudinal and latitudinal polished surface of the mature radular teeth from *C. stelleri* in ambient air using a Triboindenter nanomechanical testing system (TI-950, Hysitron, Minneapolis, MN, USA) with a berkovich tip at a peak force of 5mN. The load function consisted of a 5-second loading to 5 mN, followed by a 5-second hold at that force, and

then a 5-second unloading. The resulting indents in a grid-array measured ca. 12.5 μm apart for longitudinal surface and ca. 3 μm apart for latitudinal surface. The hardness and reduced modulus were calculated from the unloading curve of each, using the Oliver-Pharr method [38].

4.2.5 Confocal microscopy

To obtain the geometry of the mature tooth that can be applied in Abaqus for finite element analysis, a mature tooth was analyzed with confocal microscopy. A single tooth with a mineralized cap and a small part of stalk was removed manually from anterior-most region of radula after dehydration. The tooth was air dried and then immersed in the mixture of oil and fluorescent dye (DiI) between two thin glass slices. The prepared "sandwich" was examined under confocal microscopy with a 10X objective lens and 5μm steps to get 3-D surface information of one side of the tooth. Surface information of the other side was collected after flipping the "sandwich". Data files were in Nd2 format. ImageJ, Amira5.3.0 and Catia v5 were used to stick the two surfaces together to get geometry of a single tooth. Abaqus 6.10 was used to do finite element analysis on the tooth model.

4.3 Results

4.3.1 Microstructures of mature teeth.

To unveil the local microstructures of the mature teeth, fracture surfaces from three mature teeth were obtained manually and analyzed with SEM (Figure 4.1): (i)

longitudinal fracture at the middle cusp, (ii) latitudinal fracture at the tip, and (iii) latitudinal fracture at the bottom of the teeth.

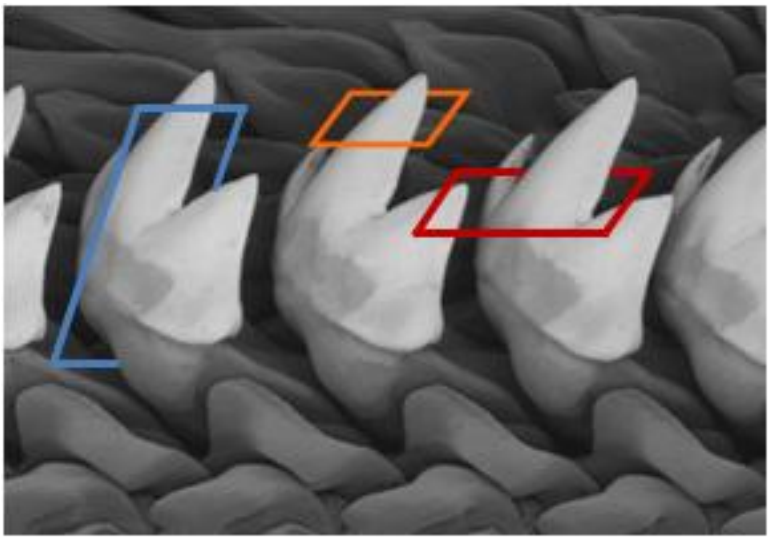

Figure 4.1 Two-dimensional planes on the Backscatter-SEM images show the positions of three fracture surfaces from mature teeth, longitudinal fracture at the middle cusp (blue), latitudinal fracture at the tip (orange), and latitudinal fracture at the bottom of the teeth (red).

4.3.1.1 Microstructures of a longitudinal fracture surface

Microstructures on the longitudinal fracture surface of a mature tooth are revealed with SEM. A shell/core structure is exhibited (Figure 4.2A). Nanorods parallel to the surfaces at both the leading and trailing edges and rotate to intersect at the central line are found at the tip of the fracture (Figures 4.2 B and C). Close examination within the 3 μm region from the tip of the fracture, where only a thin layer of the surface is peeled off, shows aggregations of particles (Figure 4.2D). Cross lamellar of rods structures are found at the central line of the tooth (Figure 4.2E). The average diameters of rods at the trailing and leading edge are 146±16 nm and 157±24 nm, respectively (Figures 4.2F and G). The

rods structures at the leading edge are covered with a 1 μm thin layer of small (Figure 4.2 G).

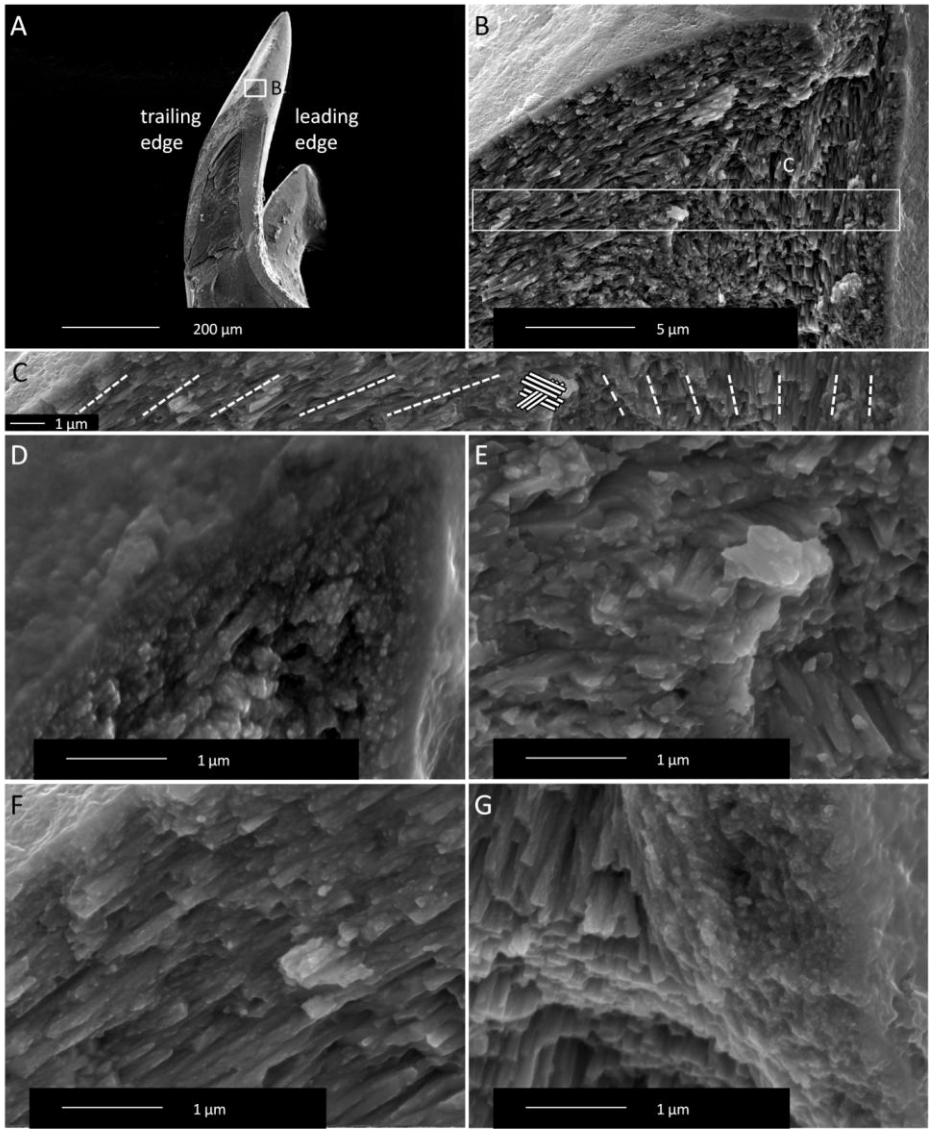

Figure 4.2 SEM analysis of the longitudinal fracture surface of a mature tooth reveals a shell/core structure; figures B-G were taken within the white box (A). At the tip of the fracture, nanorods are parallel to the surfaces at both the leading and trailing edges and rotate to intersect at the central line (B). The direction changes of the nanorods from leading edge to trailing edge are tracked by dashed lines (C). Within the 3 μm region from the tip of the fracture, where only a thin layer of the surface is peeled off, only aggregations of particles are found (D). Cross lamellar rods structures are found at the

central line of the tooth (E). Rods parallel to the surface with an average diameter of 146±16 nm are found at the trailing edge (F). Rotating nanorods with an average diameter of 157±24 nm covered with a 1 μm thick layer of small particles are found at the surface of the leading edge (G).

SEM analysis of the longitudinal fracture surface at the trailing edge at the 2/3 height of the tooth reveals parallel nanorods with an average diameter of 206±26 nm (Figure 4.3A). Close examination of the fracture surface shows that each rod is made of mineral particles growing on organic fibers, and fracture occurs not only the interfaces between rods, but also in the middle of rods (Figure 4.3B).

At 1/3 height of the tooth at the trailing edge, with indistinct boundaries and rough surfaces, the size of the rods are not quantifiable. However the rods still tend to be parallel to the surface. The particle region is about 5 μm thick (Figure 4.4A). Close examination shows that between rough rods there are aggregates of particles, which are not confined by organic fibers to form rods (Figure 4.4B).

Three regions at the surface of the leading edge at half the height of a mature tooth are revealed: (i) region of particles within 3 μm from the surface; (ii) distinct rods structures with an average diameter of 149±27 nm within 9 μm from the particle region; (iii) close-packed particles in the middle of leading edge (Figure 4.5A). Analysis at the intersection between region (i) and (ii) shows that particles start to be present between rods in region (ii) and cause the gradual disappearance of the boundaries of the rods in region (iii).

The same three regions are found at the surface at the leading edge at 2/3 height of the tooth, with variations in size though: (i) region of particles within 1 μm from the surface; (ii) distinct rods structures with a diameter of 161±37 nm within 4 μm from the particle region; (iii) close-packed particles in the middle of leading edge (Figure 4.6A). Close examination of region (iii) reveals that the particles are densely packed (Figure 4.6B).

Disassociation between the core and the leading edge due to the shrinkage of the organic fibers in the core from drying, as well as the elastic modulus mismatch between the two regions, is observed (Figure 4.7A). Mineral particles, about 69±4 nm in diameter, attached to organic fibers, are found in the core region (Figure 4.7B). Orientations of the organic fibers are from the bottom left to the upper right, similar to the curvature of the trailing edge. EDS analysis of the core region confirms the organic content is higher than at the edge.

The latitudinal fracture surface at the tip of a mature tooth was analyzed with SEM (Figure 4.8A). Close examinations have been performed in three areas: the trailing edge (Figure 4.8B-D), the leading edge (Figure 4.8F), and the conjunction zone between these two edges (Figure 4.8E). Cross sections of rods are revealed at the trailing edge (Figure 4.8B-D). The surface of the rods is rough (Figure 4.8D). The rods at the trailing edge rotate to be perpendicular to the long axis of the tooth at the conjunction zone and merge to the close-packed particle regions at the leading edge (Figure 4.8E). Close examination of the leading edge (Figure 4.8F) reveals the close-packed particles at the

relative smooth fracture region (Figure 4.8G) and the rods structures close to the surface (Figure 4.8H). With a thin layer of the surface peeled off, the rotating rods structures at the surface of the leading edge are revealed from side view (Figure 4.9).

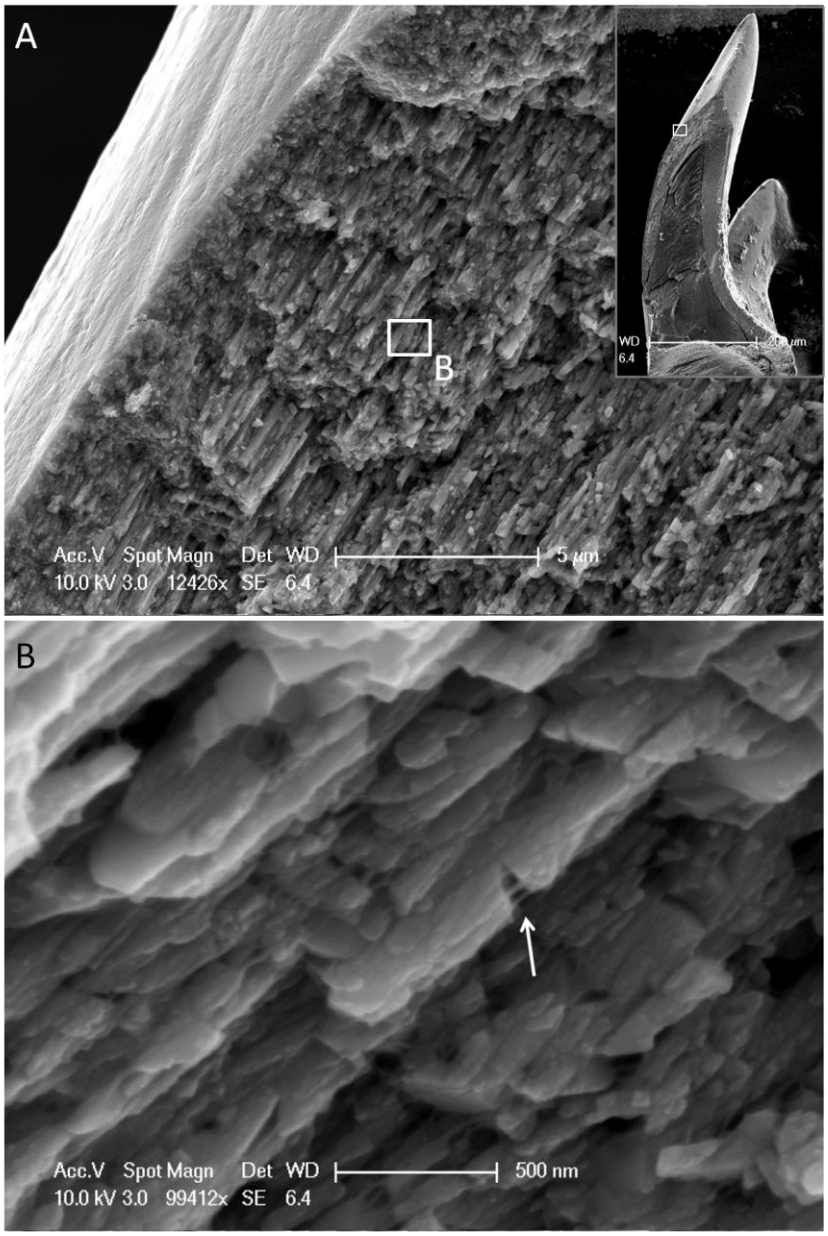

Figure 4.3 SEM analysis of the fracture surface from the trailing edge at 2/3 height of the tooth reveals parallel nanorods with an average diameter of 206±26 nm (A). The white box in the index shows the position where figure A was taken. Close examination of the

fracture shows that each rod is made of mineral particles confined by organic strings; and fracture occurs at not only at the connection between rods but also the middle of rods (B).

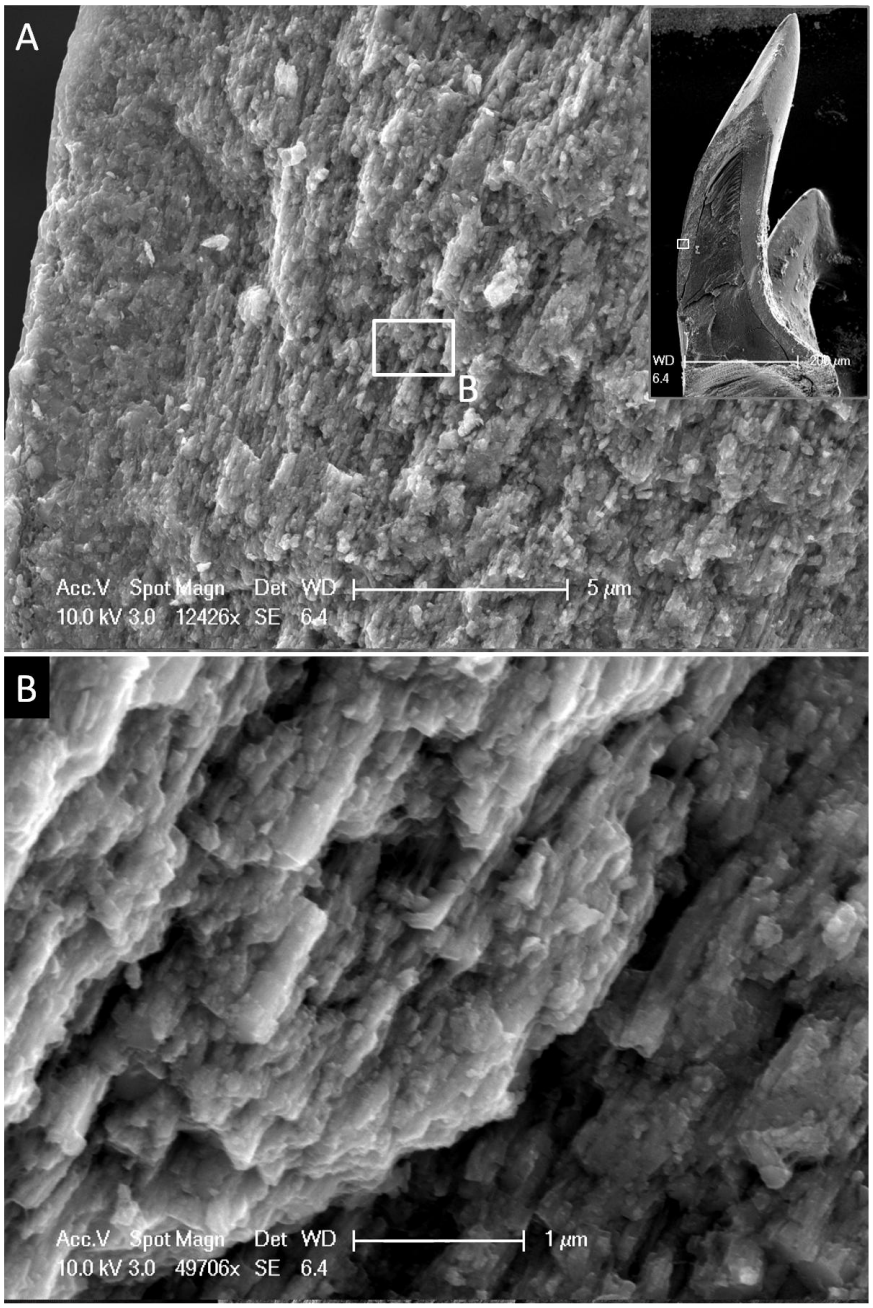

Figure 4.4 At 1/3 height of the trailing edge, with indistinct boundaries and rough surfaces, the size of the rods, or semi-rods, are not quantifiable. However the rods are still parallel to the surface. The particle region is about 5 μm thick (A). Close examination shows that there are aggregates of particles between rough rods, which are not confined by organic fibers to form rods (B).

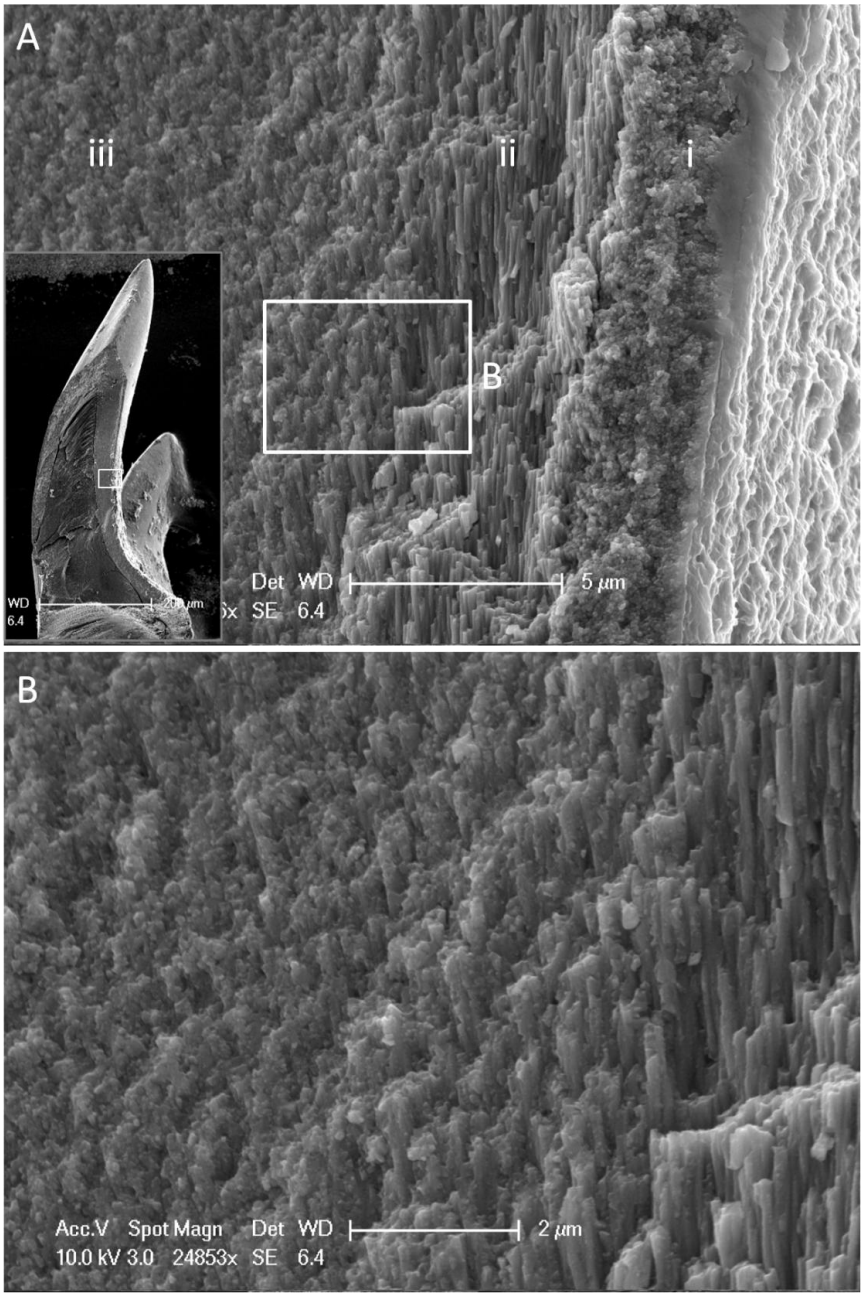

Figure 4.5 Examination of the fracture surface at the leading edge at half height of a mature tooth reveals three regions: (i) region of particles within 3 μm from the surface; (ii) distinct rods structures with an average diameter of 149±27 nm within 9 μm region from the particles; (iii) close-packed particles in the middle of leading edge (A). Analysis at the intersection between regions (ii) and (iii) shows that particles start to present between rods in region (ii) and cause the gradual disappearance of the boundaries of the rods in region (iii).

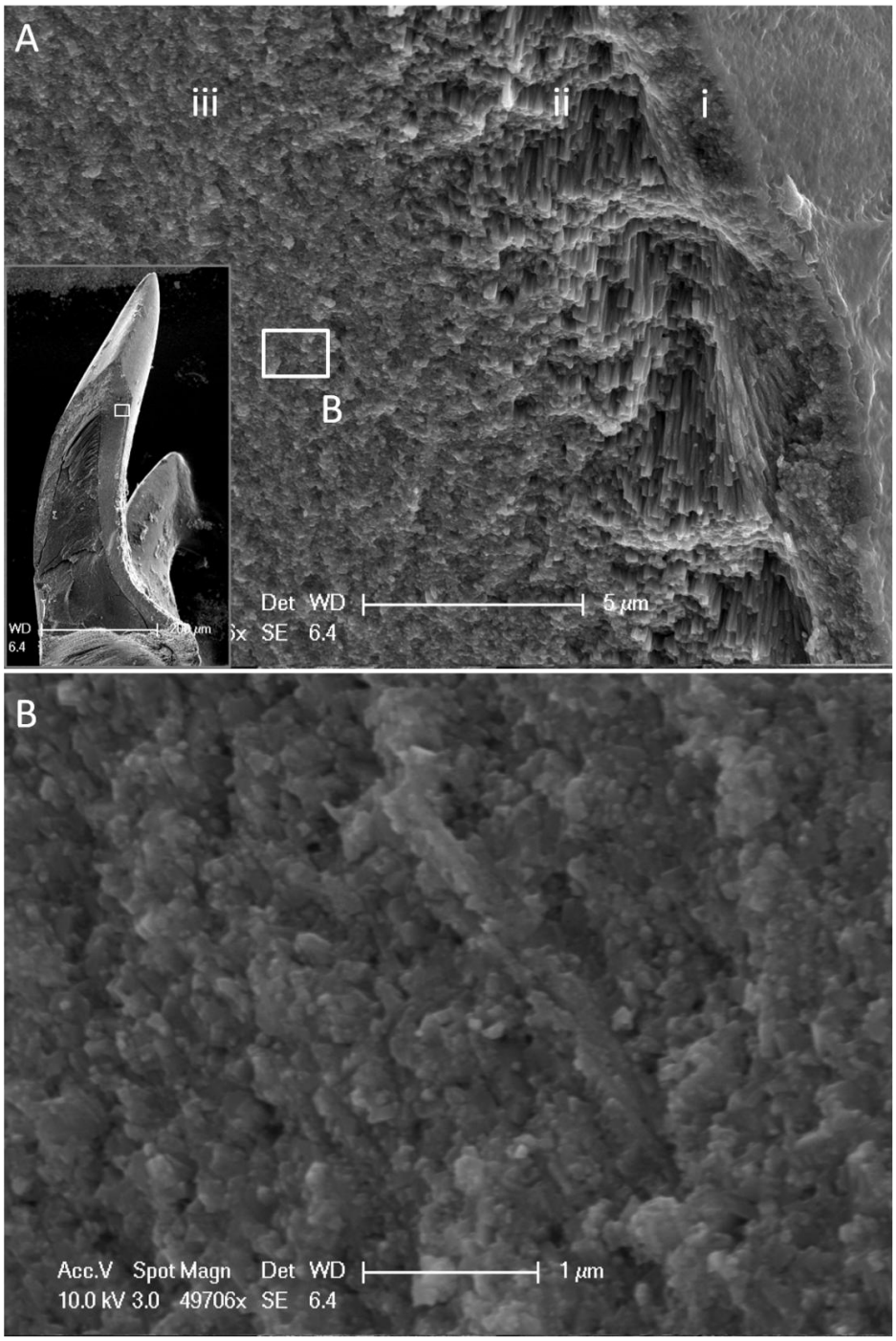

Figure 4.6 Examination of the fracture surface at the leading edge at 2/3 height of a mature tooth reveals three regions: (i) region of particles within 1 μm from the surface; (ii) distinct rods structures with an average diameter of 161±37 nm within 4 μm region from the particles; (iii) close-packed particles in the middle of leading edge (B).

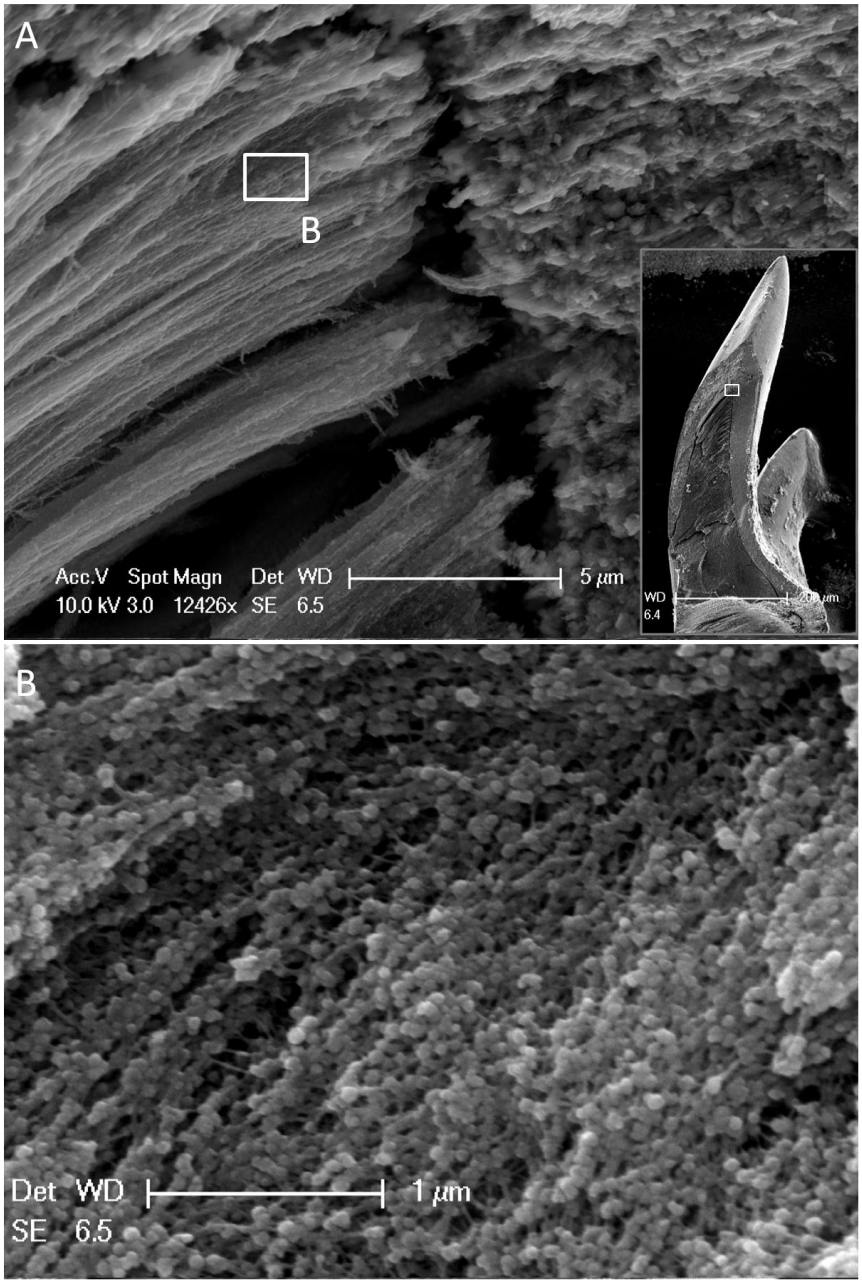

Figure 4.7 Disassociation between the core (left) and the leading edge (right) due to the shrinkage of the organic fibers in the core from drying, as well as the elastic modulus mismatch between the two regions, is observed (A). Mineral particles, about 69±4 nm in diameter, attached to organic fibers are found in the core region (B). Orientations of the organic strings are from the bottom left to the upper right, similar as the curvature of the tooth (B). EDS analysis confirms the organic content is higher in core region than at the shell.

4.3.1.2 Microstructure of a latitudinal fracture surface at the tip of a mature tooth

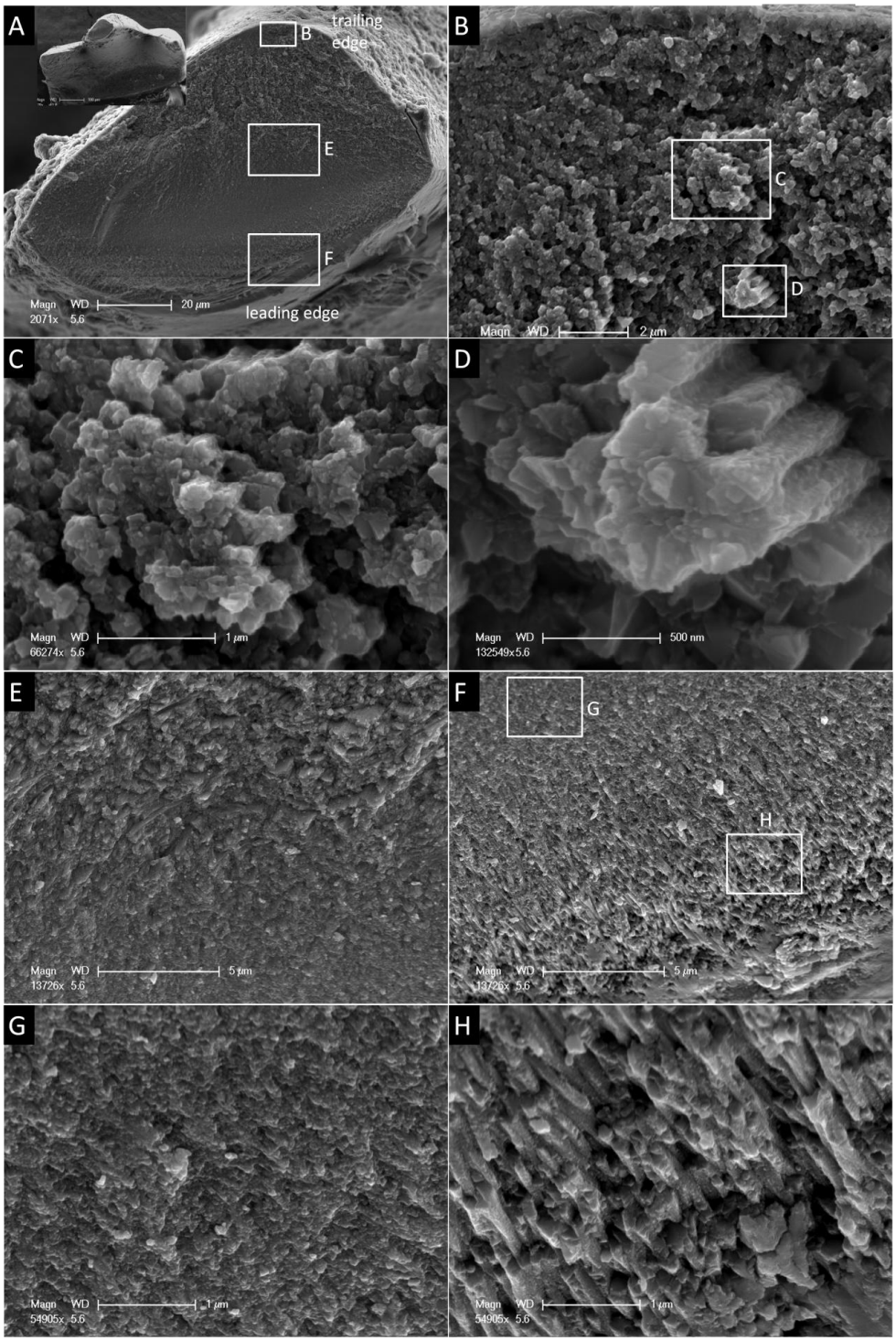

Figure 4.8 SEM analysis of the latitudinal fracture surface at the tip of a mature tooth. White boxes in (A) represent the three regions that were examined: the trailing edge (B),

the leading edge (F) and the conjunction zone between these two edges (E). Cross sections of rods are revealed at the trailing edge (B-D). The surface of the rods is rough (D). The rods at the trailing edge rotate to be perpendicular to the long axis of the tooth at the conjunction zone and merge to the close-packed particle region at the leading edge (E). Examination of the leading edge (F) reveals the close-packed particles at the relative smooth fracture region (G) and the rods structures close to the surface (H).

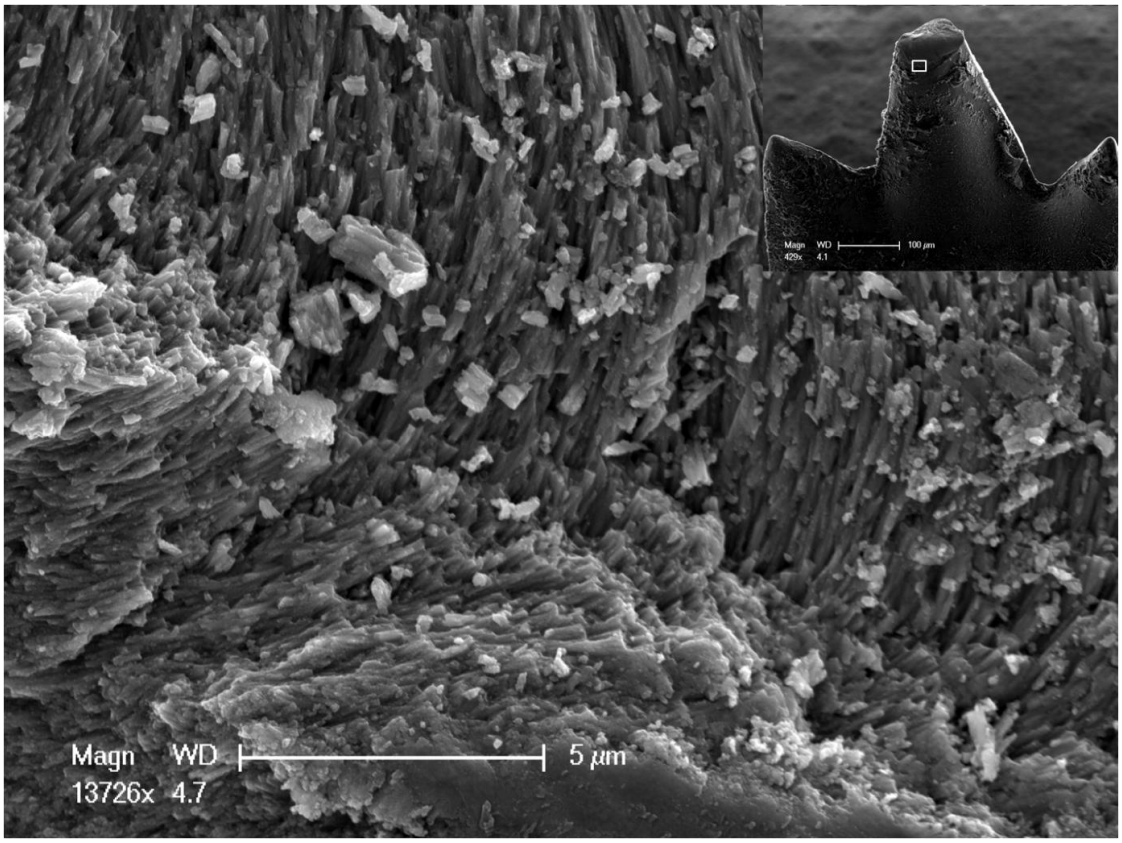

Figure 4.9 Side view from the leading edge of the fracture from figure 4.7. With a thin layer of the surface being peeled off, rods with rotating directions are revealed.

4.3.1.3 Microstructure of a latitudinal fracture surface at the bottom of a mature tooth

SEM analysis of a latitudinal fracture surface at approximately half the height of a mature tooth reveals the shell/core structure (Figure 4.10A and B). Close examinations

were performed at four areas: the trailing edge (Figure 4.10C and D), the core (Figure 4.10E and F), the middle of the leading edge (Figure 4.11), and the surface of the leading edge (Figure 4.12 and 4.13).

The trailing edge consists of particle aggregates without distinct morphology. The size of the aggregates is wide distributed (Figure 4.10C and D). The core region is made of particles nucleated on organic fibers (Figure 4.10E and F).

The fracture at the middle of the leading edge is relatively smooth (Figure 4.11A). Close examination of this area with SEM reveals an area with closely packed particles (Figure 4.11B).

SEM analysis of the surface of the leading edge shows the cross section of Figure 4.6A (Figure 4.12). The surface consists of nanorods parallel to the long axis of the tooth and covered with a 2 μm-thick particle region. The rods rotate to be perpendicular to the long axis gradually as they approaching the particle area at the surface. A decrease of the diameter of the rods occurs concurrently. Examination of the area which is 12 μm away from the surface of the leading edge (as shown by the white box in figure 4.12) reveal a mixture with cross sections of rods and small particles between them (Figure 4.13), showing a conjunction area between the rods structures at the surface and the particles in the middle of the leading edge (area ii and iii in figure 4.6A).

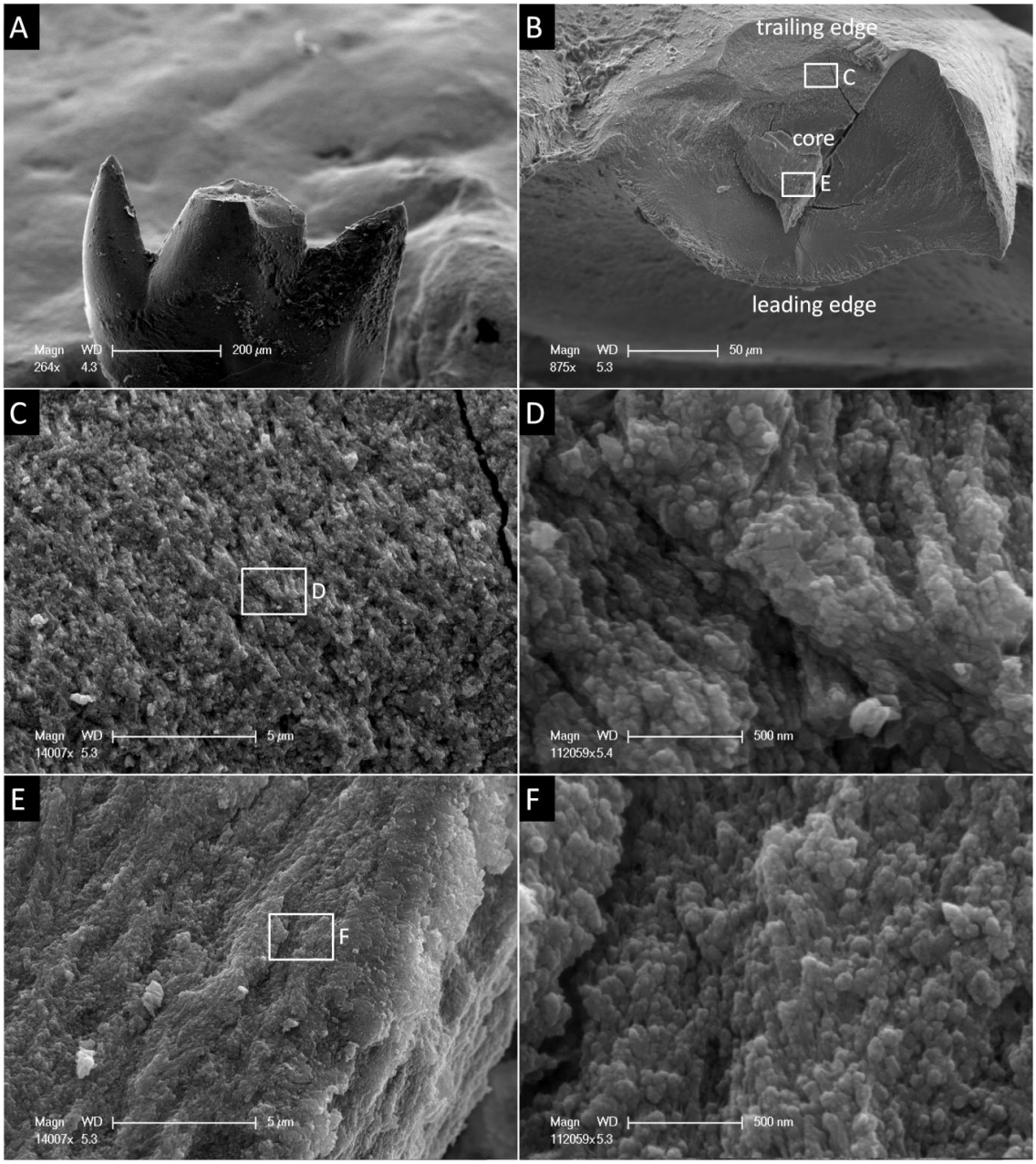

Figure 4.10 SEM analysis of a latitudinal fracture surface at approximately half the height of a mature tooth (A). The shell / core structure is exposed (B). White boxes represent the regions where the examinations at the trailing edge (C) and the core (E) were performed. The trailing edge consists of particle aggregates without distinct morphology (C, D). The core region is made of particles nucleated on organic fibers (E, F).

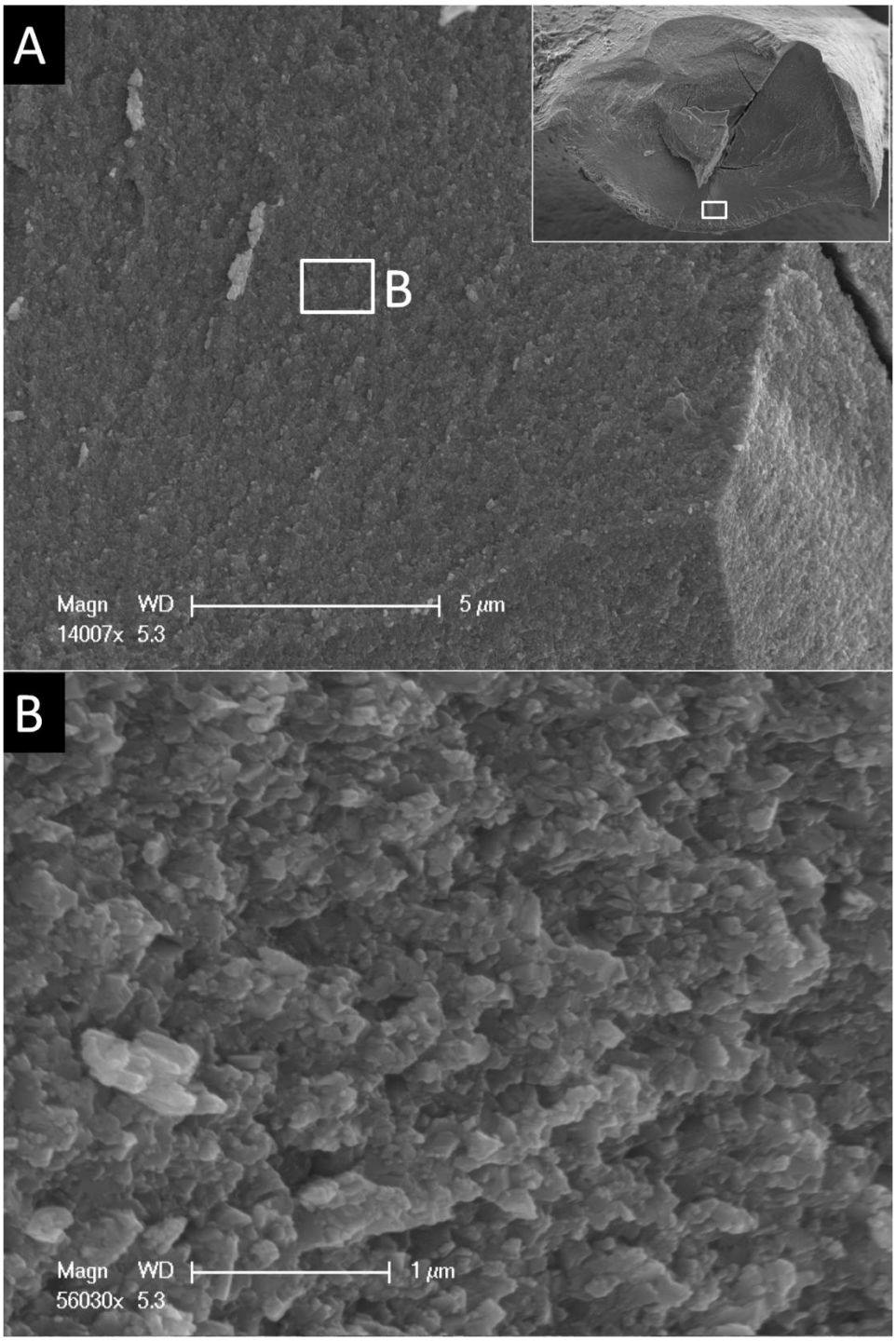

Figure 4.11 SEM analysis of the middle of the leading edge from the same fracture of figure 4.10 reveals closely packed particles with wide size distribution range (B). Index in A shows the position of (A), and the white box in (A) shows the position of (B).

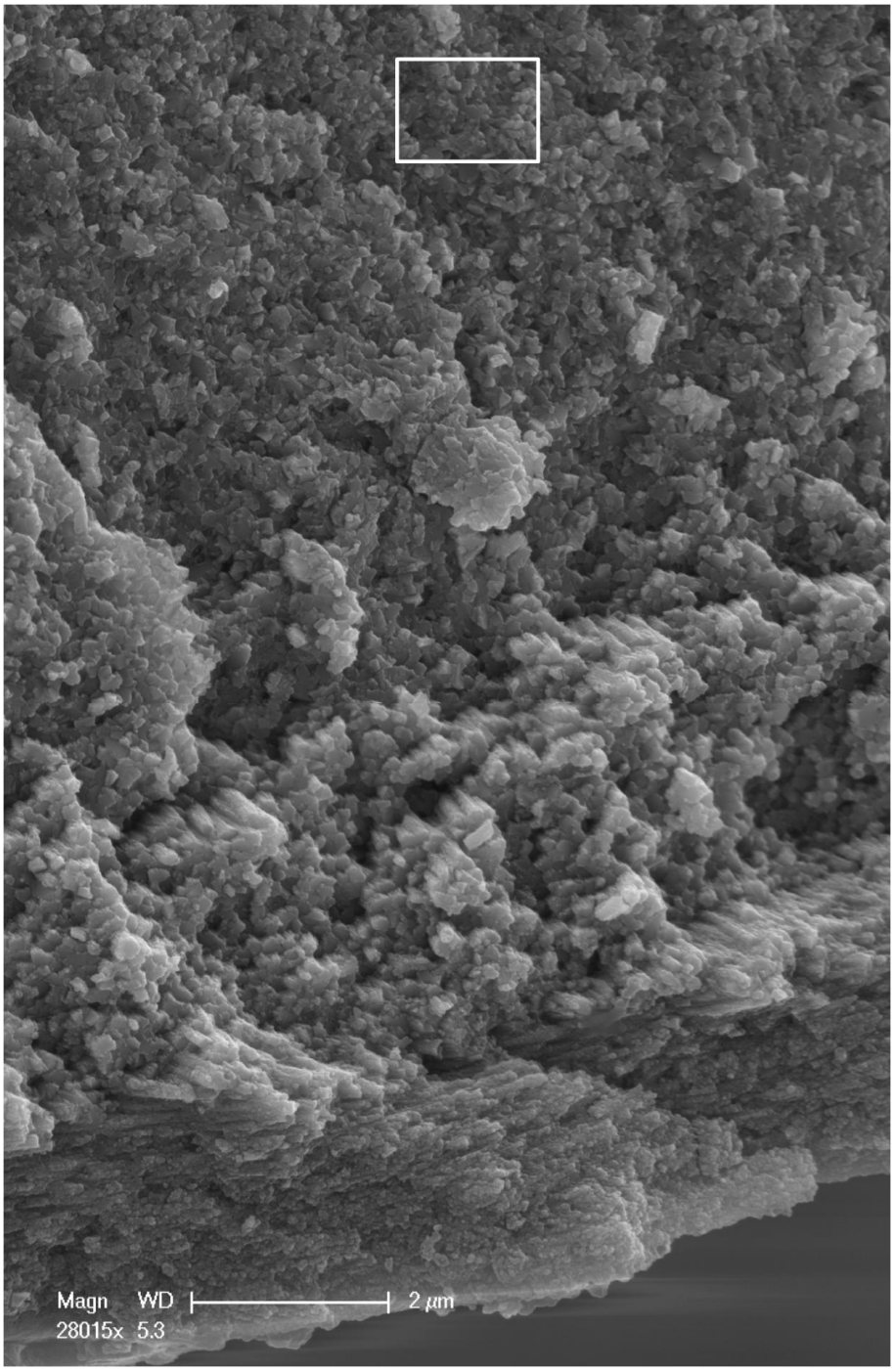

Figure 4.12 SEM analysis of the surface of the leading edge from the same fracture as seen in figure 4.10. The surface is made of nanorods parallel to the long axis of the tooth and covered with a 2 μm-thick particle region. The rods rotate to be perpendicular to the long axis gradually as they approaching the particle area at the surface. A decrease of the diameter of the rods occurs concurrently.

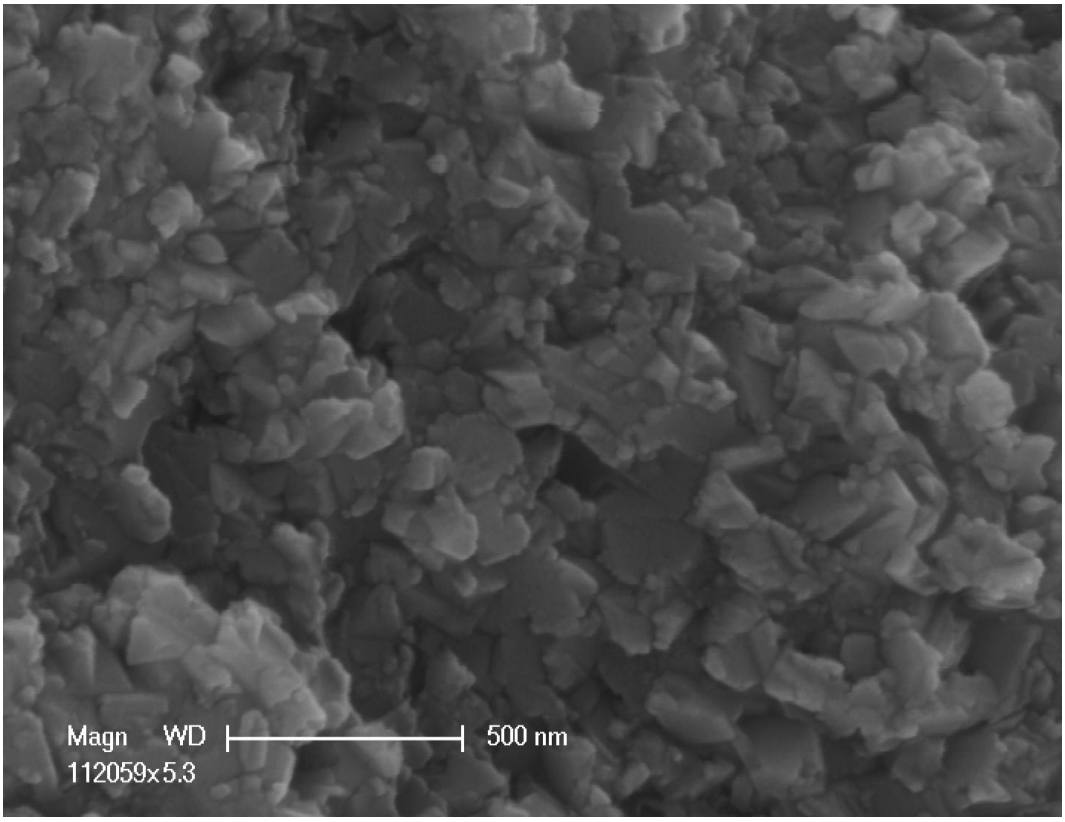

Figure 4.13 Examination on the latitudinal fracture surface of an area 12 μm inward of the surface of the leading edge (as shown by the white box in figure 4.12). A mixture with cross sections of rods and small particles between them is revealed.

4.3.2 TEM analysis of the surface of the tooth

To study the nanostructure of the surface of the leading edge, a thin section perpendicular to the long axis of the tooth was obtained with FIB from a longitudinally polished surface of a mature tooth (Figure 4.14A). Three areas of the thin section are identified under TEM: (I) closely packed particles; (II) rods perpendicular to the long axis of the tooth, labeled with dashed lines; (III) cross sections of rods that are parallel to the long axis of the tooth, labeled with dashed circles (Figure 4.14B). The striations from bottom left to upright are artifacts from FIB.

The particles in region (I) at the surface have wide size distribution, from ca. 8 nm to ca. 60 nm (Figure 4.15A, B). Selected area diffraction of the particles confirms that they are made of magnetite crystals without preferred orientation (Figure 4.15B index). HR-TEM was performed at the middle and surface of the particle area, proving the presence of the magnetite crystals and showing their arrangement. D-spacings of the lattices are labeled (Figure 4.15C, D). The darker area at the surface of the tooth is from the staining of protein during sample preparation and is not the focus of this study (Figure 4.15D).

The surfaces of the nanorods from area (III) are rough (Figure 4.16A). The striations from the bottom left to the upper right are artifacts from FIB. Close examination reveals that each rod is made of ca. 10 nm nanocrystals. Crystal bridges can be found between rods, as the arrows showing (Figure 4.16B). HR-TEM was performed at both the surface (Figure 4.16C) and the center (Figure 4.16D) of the cross section of a rod, proving the crystals consisted of magnetite. D-spacing of the lattices from magnetite crystals are labeled in this figure.

Elemental analysis across the surface of the leading edge shows the presence of iron, oxygen and small amount of carbon (Figure 4.17).

To study the nanostructures at the surface of the trailing edge, a thin section perpendicular to the long axis of the tooth was obtained with FIB from the same longitudinally-polished surface (Figure 4.18A). The thin section was milled at 1/3 height of the tooth, as shown in the index of Figure 4.18A. Irregular cross sections of mineral

aggregates are revealed with TEM (Figure 4.18B). Crystal bridges are found between mineral aggregates (Figure 4.18C). Examination of the center of the bundle reveals magnetite crystal structures (Figure 4.18D). D-spacings of the crystal lattices are labeled.

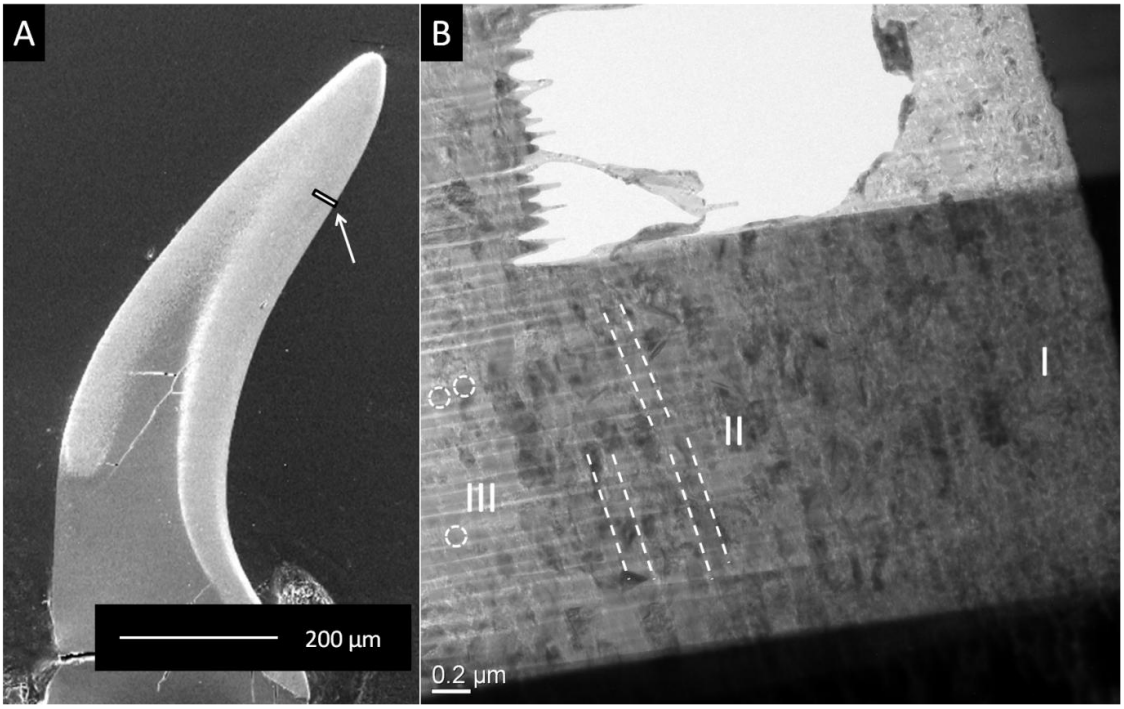

Figure 4.14 A thin section is obtained with FIB at the surface of the leading edge on a longitudinally polished surface of a mature tooth (A). The thin section is perpendicular to the long axis of the tooth. An arrow shows the location of the thin section on the tooth (A). Three areas of the thin section are identified with TEM: (I), closely-packed particles; (II), rods perpendicular to the long axis of the tooth, labeled with dashed lines; (III) cross sections of rods that are parallel to the long axis of the tooth, labeled with dashed circles (B). The striations from bottom left to upright are artifacts from FIB.

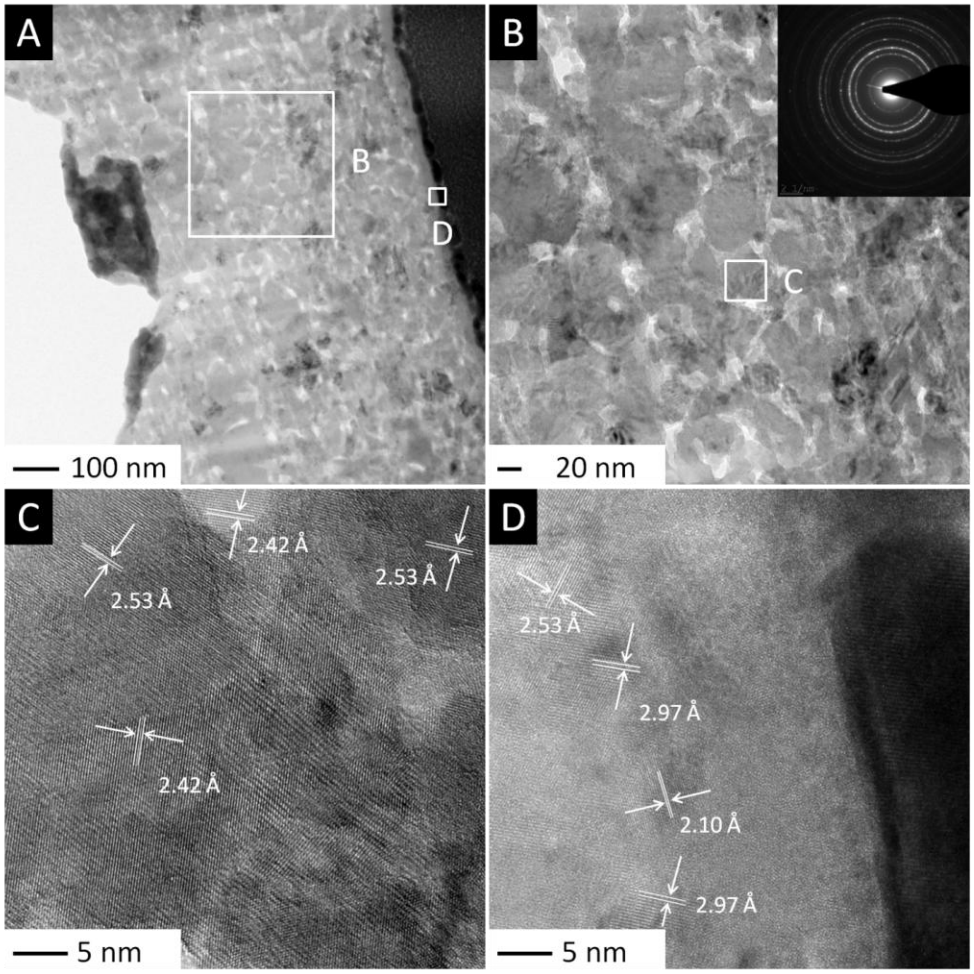

Figure 4.15 TEM analysis of the particle region at the surface. The particles at the surface have wide size distribution, from ca. 8 nm to ca. 60 nm (A, B). Selected area diffraction of the particles shows that they consist of magnetite crystals (B index). Magnetite crystals are also identified with HR-TEM from the middle of the particle area (C), as well as the very surface of the tooth (D). D-spacings of the lattices are labeled. The darker area in figure D is from the staining of protein during sample preparation and is not the focus of this study (D).

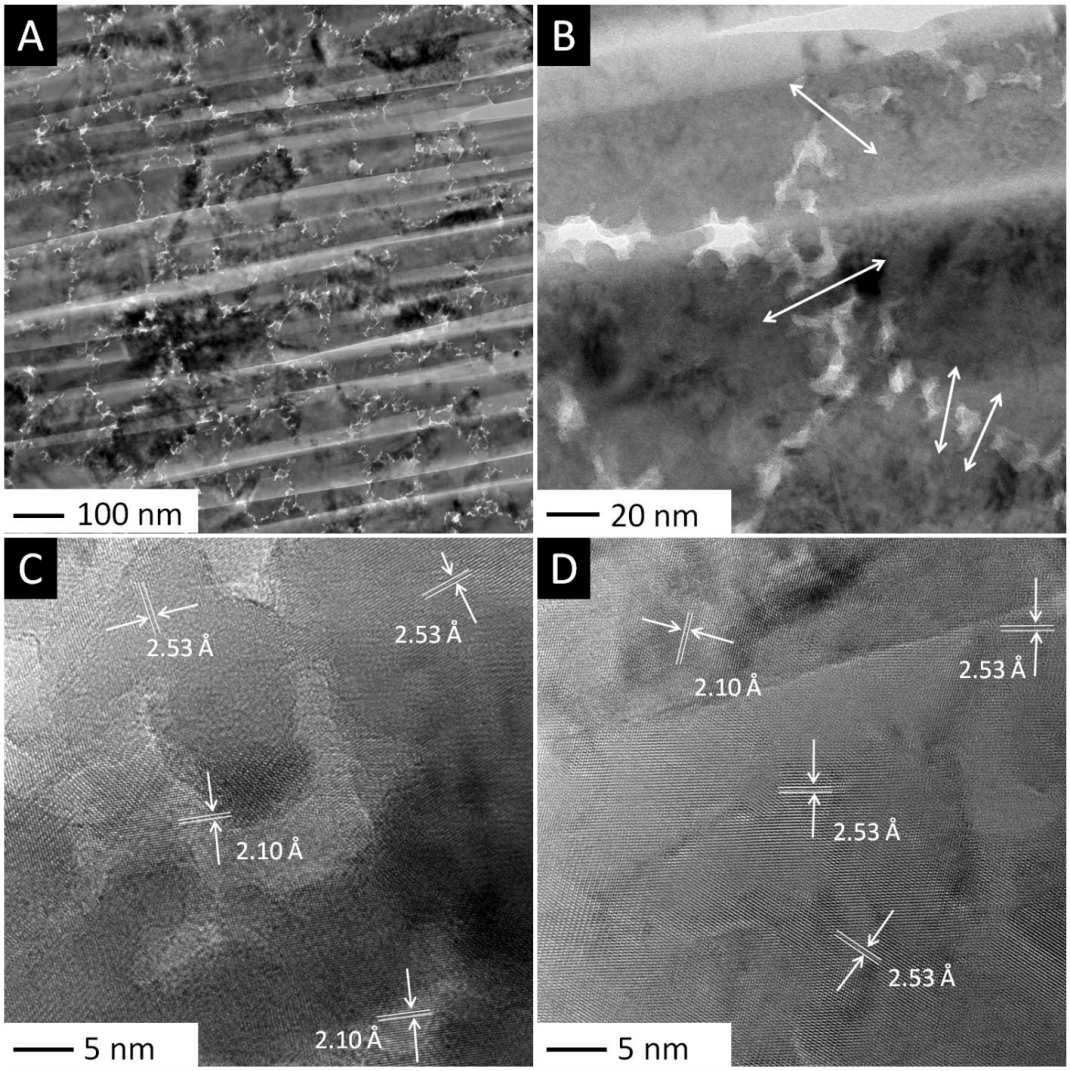

Figure 4.16 TEM examination of area (III) in figure 4.13. Cross sections of rods are exhibited. The striations from bottom left to up right are artifacts from FIB (A). Close examination reveals that each rod is made of nanocrystals, about 10nm in diameter. Crystal bridges are found between rods, as the arrows show (B). HR-TEM was performed at both the surface (C) and the center (D) of the cross section of a rod, and confirmed the presence of magnetite crystals. D-spacings of lattices from magnetite crystals are labeled in both of the two areas.

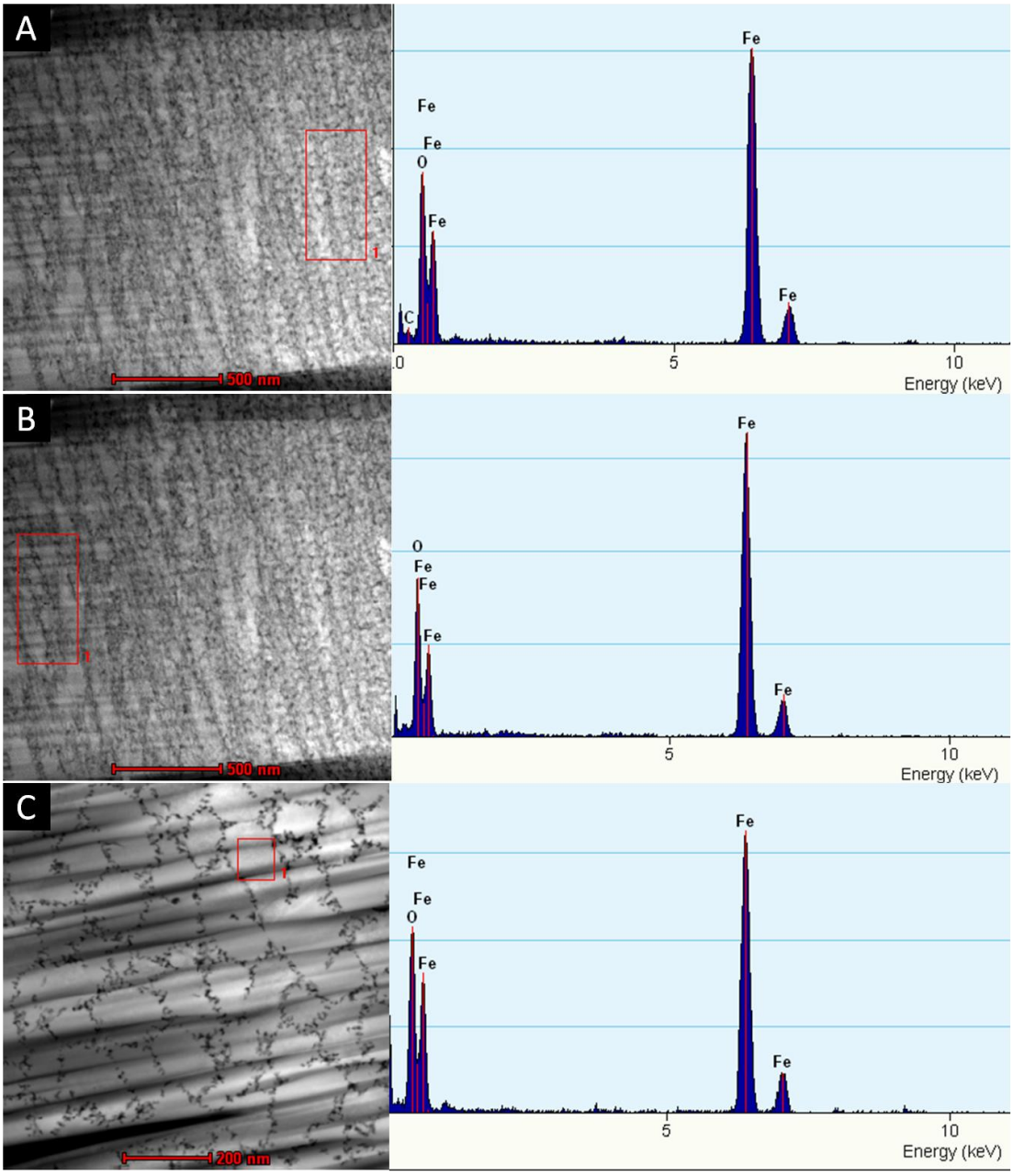

Figure 4.17 EDS of the three areas, I (A), II (B) and III (C) from the thin FIB section in figure 4.13 reveals the presence of iron, oxygen and a small amount of carbon.

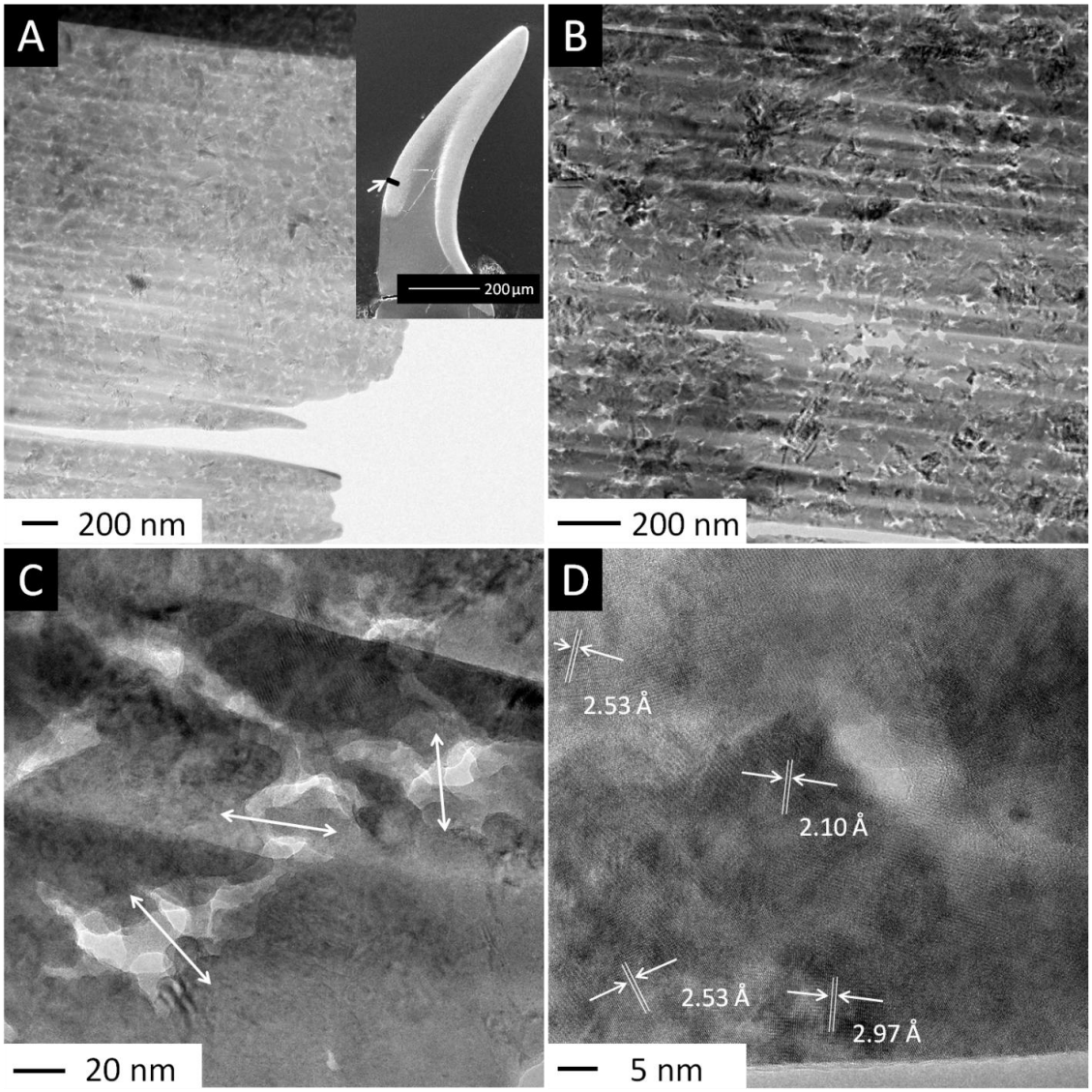

Figure 4.18 TEM analysis of a thin section obtained with FIB at the surface of the trailing edge on the same longitudinally polished surface of the mature tooth (A). The arrow in the index shows that the FIB section is perpendicular to the long axis of the tooth and at 1/3 height of the tooth (A). Irregular cross sections of mineral aggregates are revealed with TEM (B). Crystal bridges are found between mineral aggregates (C). Examination of the center of the bundle reveals magnetite crystal structures (D), with d-spacings of the crystal lattices labeled.

4.3.3 Mechanical analysis of the mature tooth

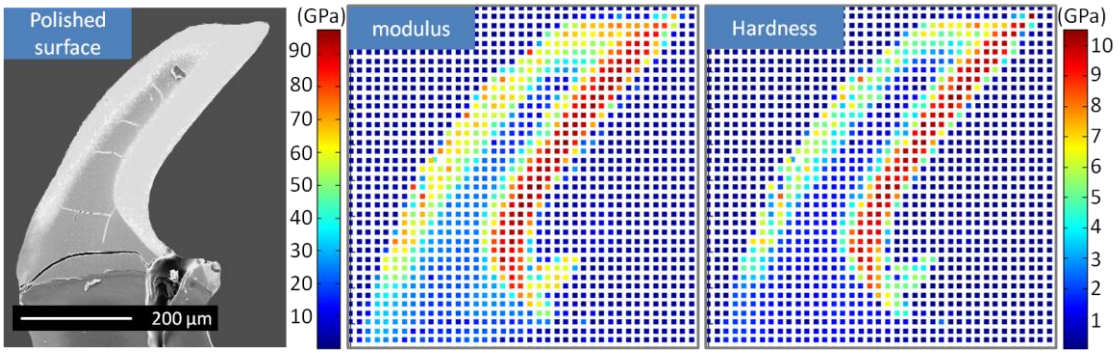

Figure 4.19 Nanoindentation with a 12.5 µm step size was performed on a longitudinal section (across the central line of the tooth) of a mature tooth. The bottom of the leading edge falls apart during sample preparation. Five latitudinal cracks propagate across the core region. A higher hardness and modulus is revealed at the leading edge than at the trailing edge. Both the highest modulus and hardness, 97.5 GPa and 10.5 GPa, is present at the middle area of the leading edge.

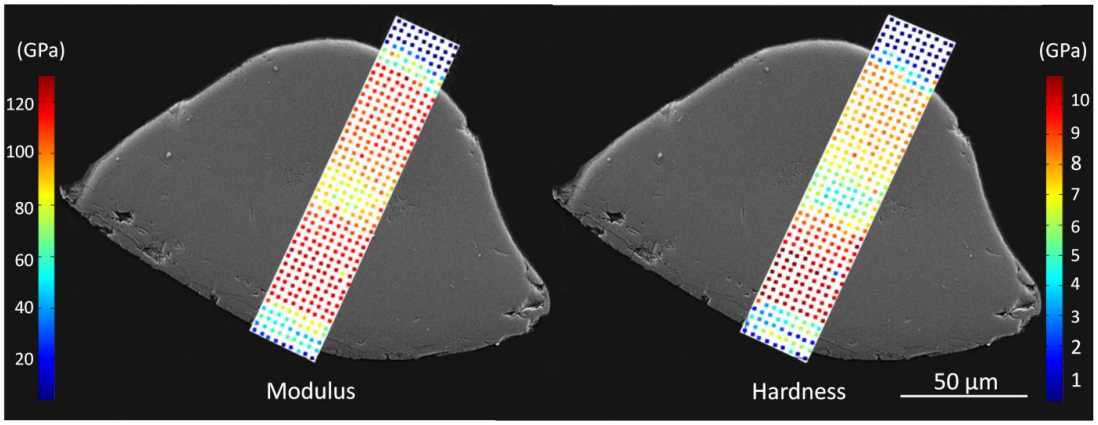

Figure 4.20 Nanoindentation with a 3 µm step size was performed on the cross section at the tip of a mature tooth. The cross section reaches the top of the core region, where it is soft. A higher hardness and modulus at the leading edge than the trailing edge is revealed. Both the highest modulus and hardness, 124.4 GPa and 11.0 GPa, is present at the middle area of the leading edge. A soft surface at both the leading edge and the trailing edge is found, 12 µm and 6 µm thick respectively.

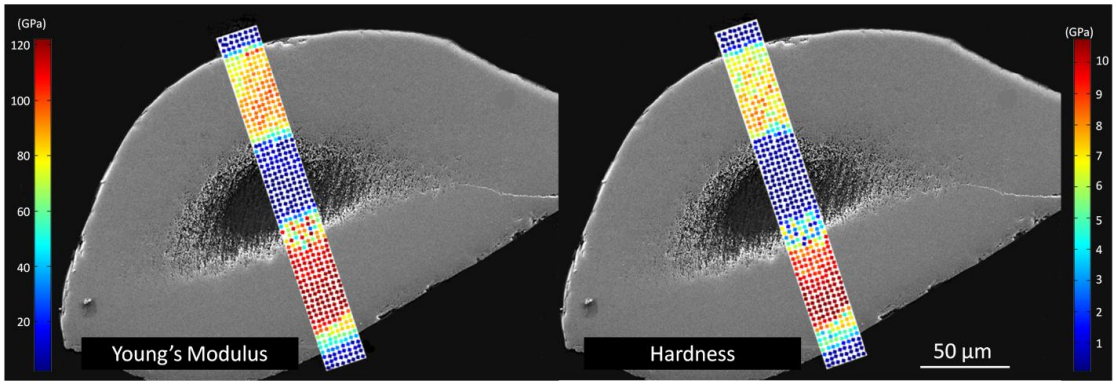

Figure 4.21 Nanoindentation with a 3 µm step size was performed on the cross section at half height of a mature tooth. The core region is soft. A higher hardness and modulus at the leading edge than the trailing edge is revealed. Both the highest modulus and hardness, 122.2 GPa and 10.8 GPa, is present at the middle area of the leading edge. A soft surface at both the leading edge and the trailing edge is found, 12 µm and 6 µm thick respectively. The transition zone between the leading edge and the core region is thicker than that between the trailing edge and the core region.

To understand the regional mechanical performance of the mature teeth, nanoindentation was performed on three polished surfaces: a longitudinal section across the central line of the tooth, latitudinal section at the tip of the tooth, and latitudinal section at half the height of the tooth. Nanoindentation on the longitudinal section (across the central line of the tooth) of a mature tooth revealed higher hardness' and moduli at the leading edge than at the trailing edge. Both the highest modulus and hardness, 97.5 GPa and 10.5 GPa, is present at the middle area of the leading edge. SEM examination of the indentation surface shows that the bottom of the leading edge falls apart during sample preparation. Five latitudinal cracks propagate across the core region (Figure 4.19).

Nanoindentation on the cross section at the tip of a mature tooth (Figure 4.20) exhibits higher hardness' and moduli at the leading edge than at the trailing edge. Both

the highest modulus and hardness, 124.4 GPa and 11.0 GPa, is present at the middle of the leading edge. A soft surface at both the leading edge and the trailing edge is found, about 12 μm and 6 μm thick respectively.

Nanoindentation on the cross section at half the height of a mature tooth (Figure 4.21) reveals a soft core region, as well as higher hardness' and moduli at the leading edge than the trailing edge. Both the highest modulus and hardness, 122.2 GPa and 10.8 GPa, is present at the middle of the leading edge. A soft surface at both the leading edge and the trailing edge is found, about 12 μm and 6 μm thick respectively. The transition zone between the leading edge and the core region is thicker than that between the trailing edge and the core region.

4.3.4 Finite element analysis of the mature tooth

To predict the structure-function relationship of the mature tooth, FEM analysis was utilized to predict the tooth performance. To obtain a model of a single tooth, surface information of a mature tooth (with part of the tooth base attached) was examined from both the leading edge side (Figure 4.22A) and the trailing edge side (Figure 4.22B) with confocal microscopy. A solid model of the tooth was obtained using the surface information via Catia (C, D). The model from Catia was then imported to Abaqus and separated into four parts: the tooth base made of chitin (Figure 4.23A), the iron phosphate core region (Figure 4.23B), the leading edge of the magnetite shell (Figure 4.23C), and the trailing edge of the magnetite shell (Figure 4.23D). Poisson's ratio of all the four parts is defined as 0.3. The elastic modulus of the four parts is defined as: 90 GPa for the

leading edge, 60 GPa for the trailing edge, 35 GPa for the core region, and 7 GPa for the tooth base. The association of the four parts is shown in figure 4.24. A longitudinal cut at the central line of the model reveals the relationship of the four parts (Figure 4.24).

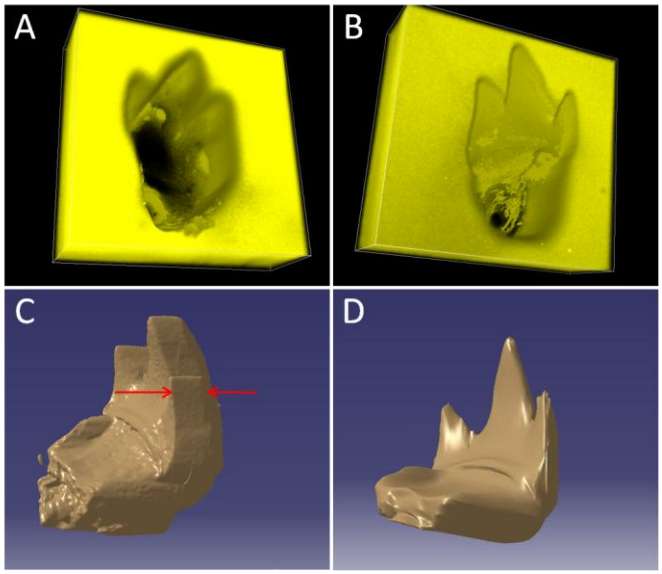

Figure 4.22 Surface information of a mature tooth (with part of the tooth base attached) was obtained from both the leading edge side (A) and the trailing edge side (B) with confocal microscopy. A solid model of the tooth was obtained using the surface information via Catia (C, D).

The tooth model was fully meshed with 3D stress and 4-node linear tetrahedrons (Figure 4.25A and B). The base of the tooth was set as fixed. A 0.1 N point force was applied at the tip of the tooth (Figure 4.25C) to simulate the working condition of radular teeth rasping for food. Non-linear effects are excluded.

With a fixed surface at the end of the tooth base and 0.1 N point force at the tip of the tooth, the distribution of the tensile (Figure 4.26A) and compressive (Figure 4.26B) strain is shown in the contour map. Strain is concentrated at the tip of the tooth, with

tensile strain at the leading edge and compressive strain at the trailing edge. The strain also concentrates at the organic tooth base. The deformation of the tooth is such that the main unit (iron phosphate core + magnetite veneer) moves as a rigid body that rotates around the organic tooth base (Figure 4.27).

Tensile stresses are mainly distributed along the leading edge, and their directions are parallel to the surface of the leading edge (Figure 4.28). On the other hand, compressive stresses are concentrated through the trailing edge, and their directions are parallel to the surface of the trailing edge (Figure 4.29).

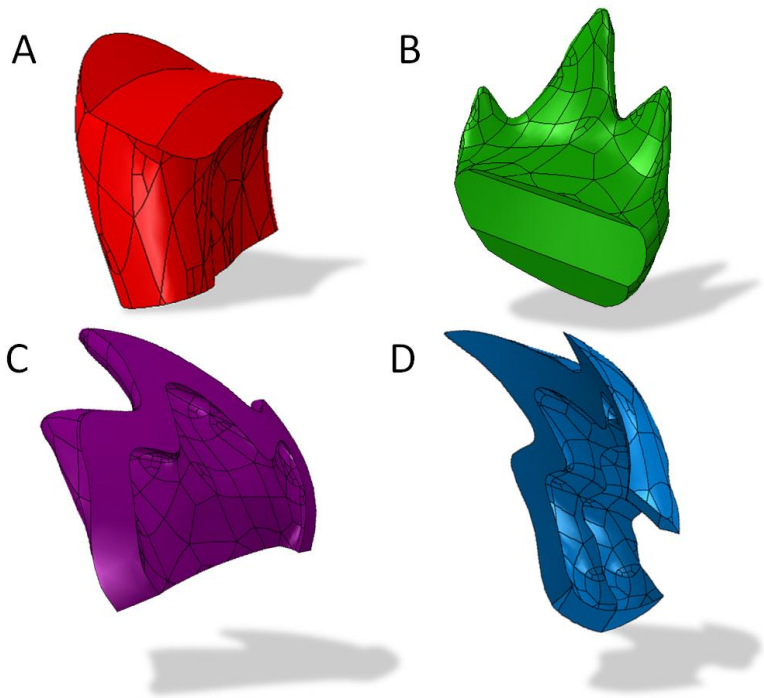

Figure 4.23 The model from Catia was imported to Abaqus and separated into four parts: the organic tooth base (A), the iron phosphate core region (B), the leading edge of the magnetite shell (C), and the trailing edge of the magnetite shell (D).

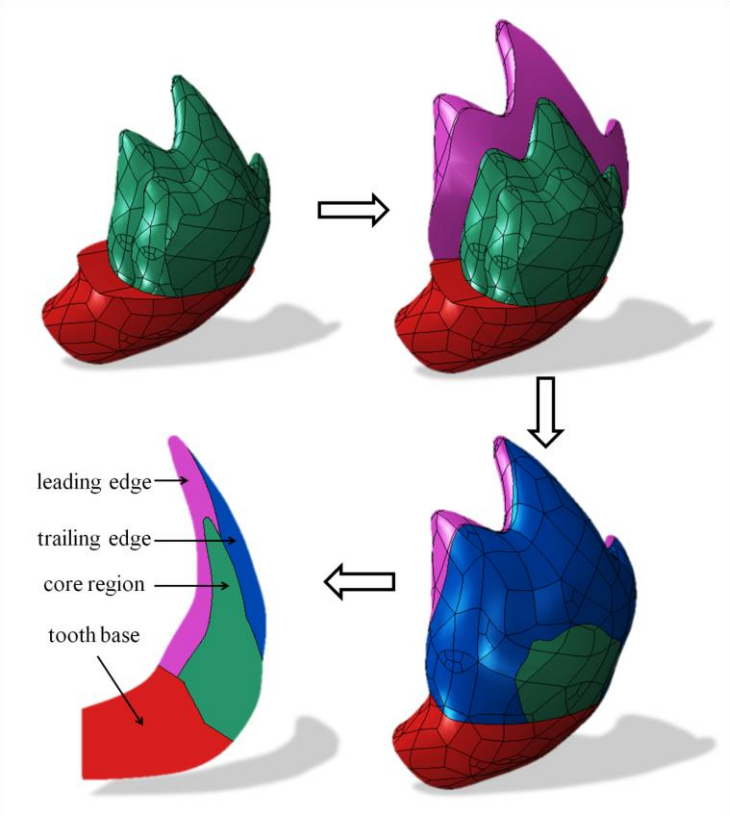

Figure 4.24 The association of the four parts is shown above. A longitudinal cut at the central line of the model reveals the relationship of the four parts.

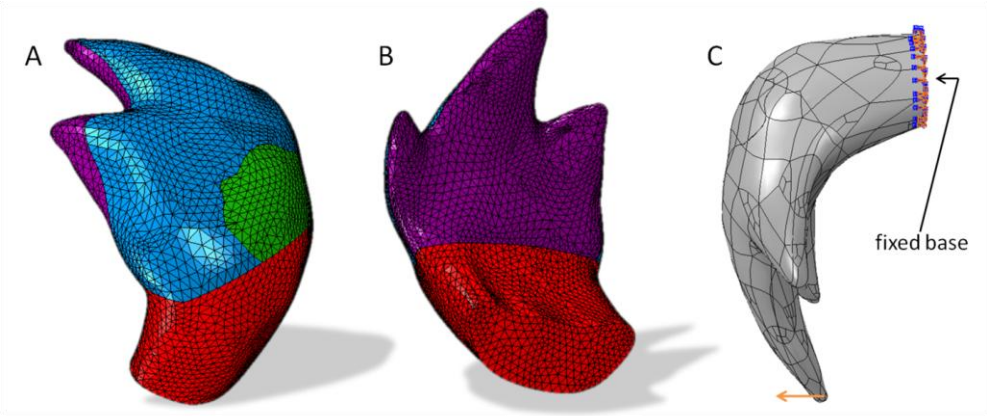

Figure 4.25 The tooth model was fully meshed with 3D stress and 4-node linear tetrahedrons. Views from the trailing (A) and leading edges (B) of the meshed model are shown above. The base of the tooth was set as fixed. A 0.1 N point force was applied at the tip of the tooth (C). Non-linear effects were not included.

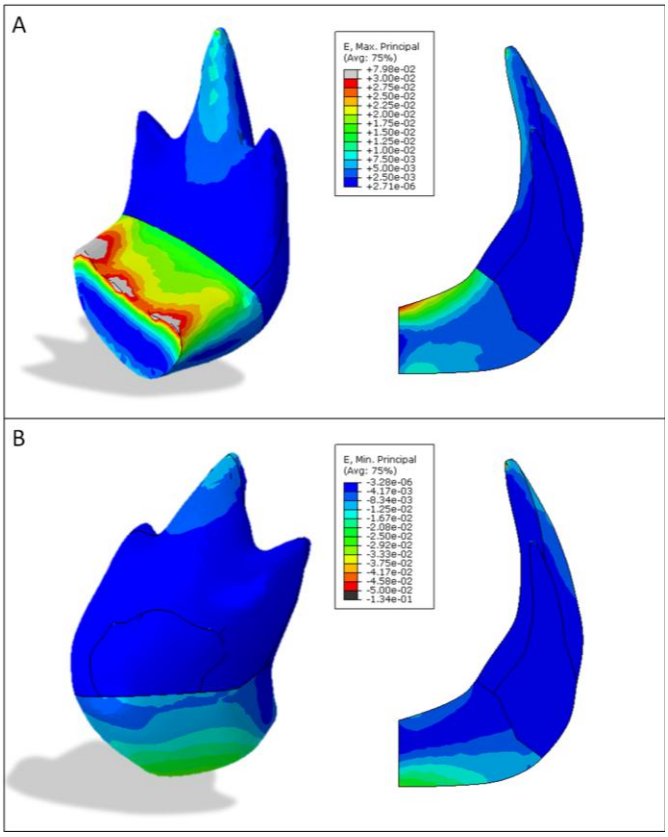

Figure 4.26 Contour maps of the distribution of the tensile (A) and compressive (B) strain. Strains are concentrated at the tip of the tooth as well as the organic tooth base.

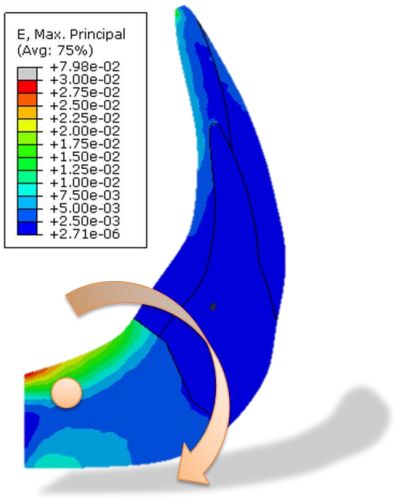

Figure 4.27 Based on the strain distribution of the tooth model, with a fixed surface at the end of the tooth base and 0.1 N point force at the tip of the tooth, the deformation of

the tooth is such that the main unit (iron phosphate core + magnetite veneer) moves as a rigid body that rotates around the organic tooth base.

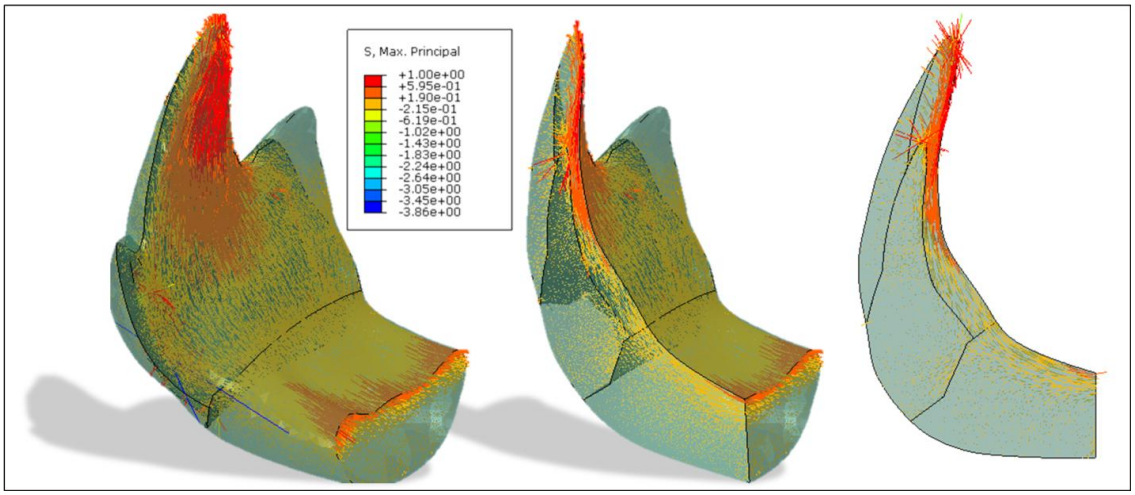

Figure 4.28 Tensile stresses are mainly distributed along the leading edge, and their directions are parallel to the surface of the leading edge.

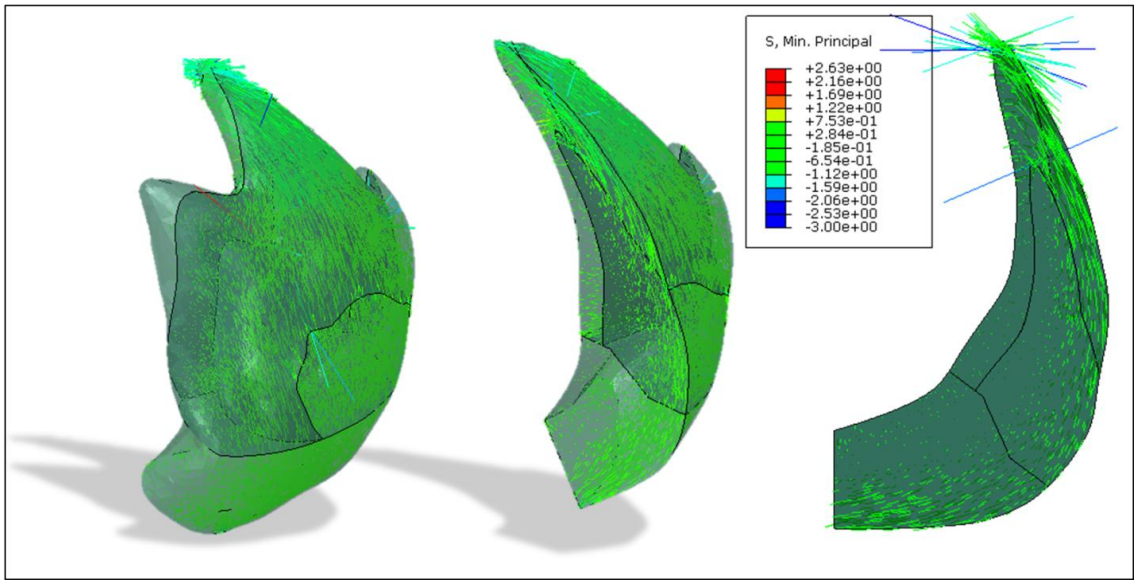

Figure 4.29 Compressive stresses are concentrated through the trailing edge, and their directions are parallel to the surface of the trailing edge.

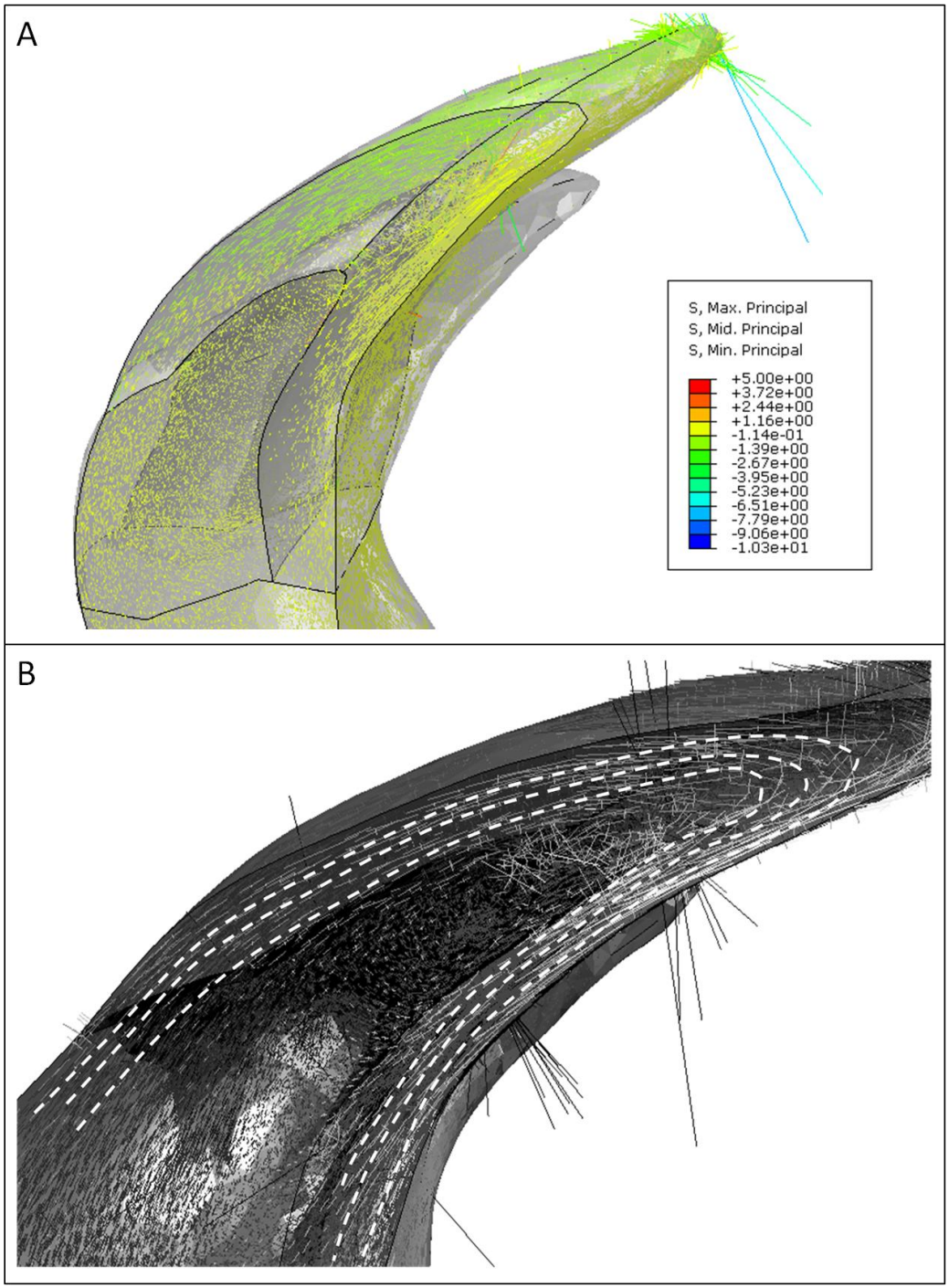

Figure 4.30 Distribution map of the principle stress on a mimetic fractured tooth (the fracture is the same as in Figure 4.2A) reveals that the stress is parallel to the surface of the tooth (A). At the transition zone between the trailing and leading edge, the direction of the stress rotates gradually as the dashed lines show (B).

A distribution map of the principle stress on a mimetic fractured tooth (the fracture is mimicking the longitudinal fracture in Figure 4.2A) reveals that the stress is parallel to the surface of the tooth (Figure 4.30A). At the transition zone between the trailing and leading edge, the direction of the stresses rotate gradually as the dashed lines show (Figure 4.30B).

4.4 Discussion

Microstructures all over the mature tooth were investigated with SEM. Nanostructures of the surfaces at both the leading and trailing edge were analyzed with TEM. Mechanical properties of the tooth were analyzed with nanoindentation on longitudinal and latitudinal sections. Tooth performance was analyzed with FEM on a mature tooth model.

Results from nanoindentation at both the longitudinal and latitudinal polished surfaces show that the highest hardness and modulus are both found at the middle area of the leading edge, where closely-packed particles structures are revealed with SEM analysis on the longitudinal and latitudinal fracture surfaces. With a wide size distribution, particles in this area are densely packed. On the other hand, at areas consisting of rods, there are gaps between magnetite rods as shown in the TEM images (Figure 4.16 and 4.18). The gaps are filled with organic material, likely chitin. With higher volume ratios of organic to mineral, the hardness' and moduli of the rods area is lower than the densely packed particle region in the middle of the leading edge [4].

Based on the SEM analysis of fracture surfaces in Figures 4.2 - 4.6, rods at the trailing edge have larger diameters than those at the leading edge. FEM analysis shows that the stress concentrated at the trailing edge is a compressive stress, while that at the leading edge is a tensile stress. Research on unidirectional fiber reinforced polymers has proved that composites with larger fiber/rod diameters have higher compressive strength. Four compressive failure modes have been identified for unidirectional composites: microbuckling, kinking, fiber failure and longitudinal cracking [39]. Increased resistance to microbuckling with increased fiber diameter has been revealed in several studies. The mechanism was proposed as that in unidirectional composites, increases in fiber/rod diameters results in the increase of the second moment area, which causes the decrease in the values of stress and deflection. The resistance of buckling increases as a result. Niu and Talreja suggested that the increased second moment area from larger fiber diameters also contributes in controlling the kinking formation during compressive failure [4, 39-42]. Bazhenov et al. proposed that the larger distance between larger fibers also improves the compressive strength [40]. The distance between adjacent fibers has control in the extent of the inelastic deformation of the matrix surrounding the fiber, and thus affects the matrix fracture energy [40]. In this way, with rods having larger diameters at the trailing edge, the tooth functions better as the compressive stress concentrates at the trailing edge during feeding process.

Crystal bridges were also discovered between rods and were found to increase the fracture toughness of the rods area. The energy for fracture to propagate through grains is

depleted during debonding of the crystal bridges. This mechanism is similar to that observed in the nacreous structures.

With the rods parallel to the stress directions, the radular teeth perform better during the feeding process. The simulation of the working condition of the radular tooth with Abaqus indicates that both the tensile stress concentrated on the leading edge and the compressive stress concentrated on the trailing edge is parallel to the surfaces of both edges. The orientations of the stresses are the same as the orientations of the rods at the trailing edge and the surface of the leading edge. In other words, the loading directions of the rods are along their long axis, which achieves the highest reinforcement efficiency in fiber reinforcement composites [43]. This is confirmed with the nanoindentation we did on both the cross sections and the longitudinal sections of the tooth. Higher hardness' and moduli are obtained at the latitudinal cross sections, where the loading directions are along the long axis of the rods.

According to the FEM analysis, the core region takes up much less stress than the shell. This protects the soft core region from catastrophic failure. The directions of the stress sustained by the core region are the same as the organic fibers in this area. This optimizes the resistance of fracture in the core region.

At the leading edge, the rods are perpendicular to the long axis of the tooth covered by the particles area at the surface, and then rotate 90° to be parallel to the long axis of the tooth (Figure 4.5-7). These rotating rods structures are not found at the surface of the trailing edge. We speculate here that the particle and rotating rods

structures at the trailing edge have been rasped away by the rocks with algae on them during the feeding process of chitons.

4.5 Conclusions

The local micro- and nanostructures as well as the mechanical properties of the mature radular teeth were analyzed. The function of the tooth was verified using Finite Element Analysis with Abaqus. With analysis of the relationship between these specific structures and their mechanical performances, this study provides design strategies for abrasion resistant composites.

4.6 Acknowledgements

We thank We thank Dr. Aron Tayler for help with confocal microscopy, Dr. Pablo Zavattieri, Jose Fernando Rave Arango, and Ajinkya Shirude for help with tooth modeling and their expertise in FEM analysis.

4.7 References

[1] H. Colfen, L. M. Qi, *Chem.-Eur. J.* **2001**, *7*, 106.

[2] S. G. Zhang, *Nat. Biotechnol.* **2003**, *21*, 1171.

[3] D. Hull, T.W.Clyne, *An Introduction to Composite Materials (Cambridge Solid State Science Series) 2 edition*, Cambridge University Press, **1996**.

[4] W. D. Callister, *Materials Science and Engineering: An Introduction (7 edition)*, Wiley, **2006**.

[5] P. G. Sanders, J. A. Eastman, J. R. Weertman, *Acta Mater.* **1997**, *45*, 4019.

[6] H. Conrad, *Metall. Mater. Trans. A-Phys. Metall. Mater. Sci.* **2004**, *35A*, 2681.

[7] H. Conrad, J. Narayan, *Acta Mater.* **2002**, *50*, 5067.

[8] M. R. Carriker, J. G. Schaadt, V. Peters, *Marine Biology* **1974**, *25*, 63.

[9] C. M. Huang, C. W. Li, M. C. Deng, T. S. Chin, *Ieee Transactions on Magnetics* **1992**, *28*, 2409.

[10] K. J. Liddiard, J. G. Hockridge, D. J. Macey, J. Webb, W. van Bronswijk, *Molluscan Research* **2004**, *24*, 21.

[11] H. K. Lu, C. M. Huang, C. W. Li, *Experimental Cell Research* **1995**, *219*, 137.

[12] D. A. Smith, *Journal of Experimental Biology* **1988**, *136*, 89.

[13] E. D. Sone, S. Weiner, L. Addadi, *Journal of Structural Biology* **2007**, *158*, 428.

[14] P. van der Wal, H. J. Giesen, J. J. Videler, *Materials Science & Engineering C-Biomimetic and Supramolecular Systems* **2000**, *7*, 129.

[15] M. S. Davies, D. J. Proudlock, A. Mistry, *Ecotoxicology* **2005**, *14*, 465.

[16] N. W. Runham, *Quarterly Journal of Microscopical Science* **1961**, *102*, 371.

[17] N. W. Runham, P. R. Thornton, D. A. Shaw, R. C. Wayte, *Zeitschrift Fur Zellforschung Und Mikroskopische Anatomie* **1969**, *99*, 608.

[18] L. A. Evans, D. J. Macey, J. Webb, *Calcified Tissue International* **1992**, *51*, 78.

[19] K. S. Kim, D. J. Macey, J. Webb, S. Mann, *Proceedings of the Royal Society of London Series B-Biological Sciences* **1989**, *237*, 335.

[20] A. P. Lee, J. Webb, D. J. Macey, W. van Bronswijk, A. R. Savarese, G. C. de Witt, *Journal of Biological Inorganic Chemistry* **1998**, *3*, 614.

[21] A. P. Lee, L. R. Brooker, D. J. Macey, J. Webb, W. van Bronswijk, *Journal of Biological Inorganic Chemistry* **2003**, *8*, 256.

[22] D. J. Macey, L. R. Brooker, J. Webb, T. G. StPierre, *Acta Zoologica* **1996**, *77*, 287.

[23] M. Saunders, C. Kong, J. A. Shaw, P. L. Clode, *Microscopy and Microanalysis* **2011**, *17*, 220.

[24] M. Saunders, C. Kong, J. A. Shaw, D. J. Macey, P. L. Clode, *Journal of Structural Biology* **2009**, *167*, 277.

[25] L. R. Brooker, A. P. Lee, D. J. Macey, W. van Bronswijk, J. Webb, *Marine Biology* **2003**, *142*, 447.

[26] A. P. Lee, L. R. Brooker, D. J. Macey, W. van Bronswijk, J. Webb, *Calcified Tissue International* **2000**, *67*, 408.

[27] J. C. Weaver, Q. Wang, A. Miserez, A. Tantuccio, R. Stromberg, K. N. Bozhilov, P. Maxwell, R. Nay, S. T. Heier, E. DiMasi, D. Kisailus, *Materials Today* **2010**, *13*, 42.

[28] C. W. Li, T. S. Chin, J. S. Li, S. H. Huang, *Ieee Transactions on Magnetics* **1989**, *25*, 3818.

[29] H. A. Lowenstam, S. Weiner, *Science* **1985**, *227*, 51.

[30] D. J. Macey, L. R. Brooker, *Journal of Morphology* **1996**, *230*, 33.

[31] K. M. Towe, *Science* **1963**, *142*, 63.

[32] J. L. Kirschvink, H. A. Lowenstam, *Earth and Planetary Science Letters* **1979**, *44*, 193.

[33] K. M. Towe, Lowensta.H.A., *Journal of Ultrastructure Research* **1967**, *17*, 1.

[34] H. A. Lowenstam, *Science* **1967**, *156*, 1373.

[35] N. W. Runham, *Quarterly Journal of Microscopical Science* **1963**, *104*, 271.

[36] J. A. Shaw, D. J. Macey, L. R. Brooker, P. L. Clode, *Biological Bulletin* **2010**, *218*, 132.

[37] J. A. Shaw, D. J. Macey, L. R. Brooker, *Journal of the Marine Biological Association of the United Kingdom* **2008**, *88*, 597.

[38] W. C. Oliver, G. M. Pharr, *Mrs Bulletin* **2010**, *35*, 897.

[39] C. R. Schultheisz, A. M. Waas, *Progress in Aerospace Sciences* **1996**, *32*, 1.

[40] S. L. Bazhenov, A. M. Kuperman, E. S. Zelenskii, A. A. Berlin, *Composites Science and Technology* **1992**, *45*, 201.

[41] A. M. Waas, C. R. Schultheisz, *Progress in Aerospace Sciences* **1996**, *32*, 43.

[42] Y. L. Xu, K. L. Reifsnider, *Journal of Composite Materials* **1993**, *27*, 572.

[43] H. Krenchel, *Fiber Reinforcement*, Akademisk Forlag, Copenhagen **1964**.

5 Chapter 5. Summary

5.1 General summary

This thesis presents the structure-function relationships in the radular teeth of *Cryptochiton stelleri*, as well as the kinetic phase transformation and structural developments during their biomineralization process. Various materials characterization methods have been adopted to achieve the objectives, including SEM, EDS, TEM, powder XRD, synchrotron XRD, confocal microscopy, Raman spectroscopy, nanoindentation and μXRF.

5.2 Structure and function relationship of the mature teeth

A hard magnetite containing shell / soft iron phosphate containing core structure is revealed in the mature teeth. A hardness and modulus gradient from the leading edge to the trailing edge is discovered with nanoindentation and contributes to the self-sharpening mechanism of the tooth.

Magnetite nanorods surrounded with an organic layer (α-chitin) parallel to the surface of the trailing edge are found all over the trailing edge. The rods at the top of the trailing edge have more clear boundaries while those at the bottom are less separated. Rotated lamellae of rods covered with particles are found at the surface of the leading edge. The middle of the leading edge is made of close-packed magnetite particles and shows the highest hardness and modulus.

FEM analysis simulating the tooth performance during feeding process proves that the leading edge sustains tensile loading and the trailing edge undertakes compressive loading. Rods with larger diameters at the trailing edge than at the surface of the leading edge are revealed and proved to have better performance during compressive loading.

Nanoindentation on both the latitudinal and longitudinal sections of the middle cusps of mature teeth shows that the cross sections of the mature teeth have higher hardness' and moduli. Since the direction of the stress is parallel to the surfaces at both edges according to FEM analyses (meaning that the stress is along the long axis of the rods), the tooth performance is optimized.

From fracture surface analysis, at the top of the tooth (without a core region in the middle), the rods from both edges rotate gradually to make lamellar intersections at the central line of the tooth. Based on FEM simulation results, the stress also rotates in the same way, which directs the loading along the long axis of the rods.

TEM analysis of the mature teeth reveals that the nanorods are made of magnetite nanocrystals without preferred orientation. Crystal bridges between rods are revealed and believed to increase the fracture toughness as the energy for the crack propagation is dissipated during fracture of these bridges.

5.3 Mineralization process of the radular teeth

Kinetic studies of the mineralization process of the hard outer magnetite containing region of the radular teeth of *C. stelleri* provides insights of the relationship

between the phase transformation and structural development during the four distinct stages of mineralization: *(i)* the formation of a crystalline α-chitin organic matrix that forms the structural framework of the non-mineralized teeth, *(ii)* the synthesis of ferrihydrite particles along these organic fibers, *(iii)* aggregation of the mineral particles with concurrent phase transformation from ferrihydrite to magnetite, and *(iv)* progressive magnetite crystal growth to form continuous parallel rods within the mature teeth.

The α-chitin matrix provides heterogeneous nucleation sites for ferrihydrite. The periodic spacing surrounding the organic matrix affects the density and size of mineral particles that further grow into highly oriented rod-like elements that exhibit regionally defined geometries, which affect the regional mechanical properties of the mature teeth. At the leading edge of the tooth, smaller spacing between the fibers is revealed together with denser nuclei and smaller particles, results in the rods with smaller diameter in mature teeth.

A phase transformation from ferrihydrite to magnetite initiates at the tip of the leading edge, with a dramatic increase of the mineral particle size. Ferrihydrite is unstable when passing a critical particle size, which drives the phase transformation to magnetite.

These studies into the biomineralization processes in the radular teeth of *C. stelleri* illustrate several design principles that could be potentially applied to not only the biomimetic synthesis of iron oxides, but also for the spatially confined template-directed growth of a wide range of inorganic materials and structural ceramics with graded moduli.

5.4 Future work

Based on the results and discussions we made in this thesis, future work of the radula project will be focused on two parts: i) experimental mimicry of the mineralization process of the radula to verify the observations we made during the biomineralization process of the radular teeth and provide biomimetic synthesis design principles; ii) FEM study of the microstructures within the mature radular teeth to obtain design strategies for abrasion resistant materials.

Further biomimetic synthesis inspired by the organic matrix controlled mineralization process will be performed by synthesizing ferrihydrite in Anodic Aluminum Oxide templates with various pore sizes. We suspect that AAO templates with various sizes may have control of the nucleation size and density, which can verify the higher density and smaller size of particles at the organic matrix with smaller spacing during the mineralization of the radular teeth.

FEM analysis of the microstructures within mature teeth will be carried out with Abaqus on the parametric study of microstructural rods. The first step will be to change the variables of solid rods: diameter, aspect ratio, alignment, and shape, while observing their mechanical performance. Each rod will be defined as a composite consisting of mineral particles surrounded with organic materials and will be compared to solid mineral rods.